LIÈGE université Library

https://lib.uliege.be

https://matheo.uliege.be

Structural Strength Improvement of Distortion Grids via Topology Optimization Cenaero

Auteur : Dinu, Carmen-Alexandra
Promoteur(s) : Salles, Loïc
Faculté : Faculté des Sciences appliquées
Diplôme : Master en ingénieur civil en aérospatiale, à finalité spécialisée en "aerospace engineering"
Année académique : 2025-2026
URI/URL : http://hdl.handle.net/2268.2/26591

Avertissement à l'attention des usagers :

Tous les documents placés en accès ouvert sur le site le site MatheO sont protégés par le droit d'auteur. Conformément aux principes énoncés par la "Budapest Open Access Initiative"(BOAI, 2002), l'utilisateur du site peut lire, télécharger, copier, transmettre, imprimer, chercher ou faire un lien vers le texte intégral de ces documents, les disséquer pour les indexer, s'en servir de données pour un logiciel, ou s'en servir à toute autre fin légale (ou prévue par la réglementation relative au droit d'auteur). Toute utilisation du document à des fins commerciales est strictement interdite.

Par ailleurs, l'utilisateur s'engage à respecter les droits moraux de l'auteur, principalement le droit à l'intégrité de l'oeuvre et le droit de paternité et ce dans toute utilisation que l'utilisateur entreprend. Ainsi, à titre d'exemple, lorsqu'il reproduira un document par extrait ou dans son intégralité, l'utilisateur citera de manière complète les sources telles que mentionnées ci-dessus. Toute utilisation non explicitement autorisée ci-avant (telle que par exemple, la modification du document ou son résumé) nécessite l'autorisation préalable et expresse des auteurs ou de leurs ayants droit.



UNIVERSITY OF LIÈGE - FACULTY OF APPLIED SCIENCES

Structural Strength Improvement of Distortion Grids via Topology Optimization

---

Master's thesis completed in order to obtain the degree of
Master of Science in Aerospace Engineering
by

Carmen - Alexandra Dinu

Supervisor
Loic Salles

Jury members
Florence Nyssen
Koen Hillewaert

Academic Year
2025-2026

Abstract

The implementation of new technologies in aircraft engines such as Boundary Layer Ingestion (BLI), Ultra-High Bypass Ratio (UHBR) engines, unducted architectures has introduced the need for advanced distortion generators that are capable to reproduce complex non-uniform swirl patterns. In addition to the aerodynamic performances, the mechanical behavior of the structure must be taken into account to ensure that the structure can withstand the loads during operation while maintaining its structural integrity. In this context, this thesis addresses the topology optimization application to a distortion grid system with the aim of improving the structural performance while allowing a reduced amount of material to be added.

A simplified test case is chosen in order to retain the main characteristics of the industry application and the workflow is tested on both $2D$ and $3D$ cases. A numerical workflow based on the maximization of the first three eigenfrequencies and a volume constraint is developed and applied on a representative blade. This baseline formulation is extended and stress constraints are added progressively based on a Computational Fluid Dynamics simulation and the geometries obtained for different optimization configurations are compared. The results show that the proposed optimization workflow generates several connecting supports for the blade structure, while respecting the imposed volume constraint. In both $2D$ and $3D$ cases, similarities are observed between the obtained results, suggesting that the eigenfrequencies and volume formulation provides an efficient design, while the stress constraint is mainly affecting the local material distribution rather than governing the overall topology. The proposed workflow is applied on the industrial case to demonstrate the applicability of the proposed method to a more complex geometry.

Overall, this study demonstrates that this topology optimization formulation provides a basis for exploring structurally efficient configurations, while more detailed aerodynamic, aeroelastic and structural analysis are needed in order to validate the final design.

Keywords: topology optimization, distortion generators, swirl patterns, mechanical performances, eigenfrequencies maximization.

Acknowledgement

I would like to express my sincere gratitude to my supervisor, Loic Salles from University of Liège for the guided support and valuable feedback.

I would like to also thank the Cenaero members, Florence Nyssen, Erin Kuci and Antoni Rebassa for providing me the opportunity and resources to carry out this work as well as for sharing their knowledge and expertise. The discussions shared through this project contributed to the development of this thesis and made the overall experience enriching and enjoyable.

Finally, I would like to thank my family, boyfriend and friends for their support and encouragement during these years of study. Their support made this achievement possible and I am deeply grateful for it.

Declaration of Artificial Intelligence Usage

This document includes the use of artificial tools, particularly ChatGPT, used to assist with language corrections and reformulations. All technical contents, results and interpretations represent entirely the author's own work.

Contents

1 Introduction **12**
- 1.1 Context . . . 12
- 1.2 Objectives . . . 13
- 1.3 Structure of the report . . . 13

2 Bibliography **14**
- 2.1 Design of distortion grids . . . 14
- 2.2 Conventional distortion generators and design methodologies . . . 15
- 2.3 Topology optimization for distortion grid design . . . 16
- 2.4 Flutter assessment . . . 20

3 Simplified test case definition **24**
- 3.1 Motivation . . . 24
- 3.2 Geometry description . . . 24
- 3.3 Geometry mechanical status . . . 25
- 3.4 CFD simulation . . . 27
  - 3.4.1 Computational domain . . . 27
  - 3.4.2 Meshing process . . . 28
  - 3.4.3 Model setup . . . 29
  - 3.4.4 Results and discussions . . . 30

4 Topology optimization applied to two-dimensional model **33**
- 4.1 Model definition . . . 33
  - 4.1.1 Loading conditions . . . 34
- 4.2 Eigenfrequency maximization with a volume constraint . . . 37
  - 4.2.1 Problem definition . . . 37
  - 4.2.2 Results and discussion . . . 39
- 4.3 Eigenfrequency maximization under a distributed load with volume and stress constraints . . . 41
  - 4.3.1 Problem definition . . . 41
  - 4.3.2 Results and discussion . . . 43
  - 4.3.3 Reduced allowable stress . . . 47
- 4.4 Eigenfrequency maximization under multiple loads with volume and stress constraints . . . 50
  - 4.4.1 Problem formulation . . . 51
  - 4.4.2 Results and discussion . . . 51
- 4.5 Comparison of the **2D** optimization cases . . . 54

5 Topology optimization applied to three-dimensional model **57**
5.1 Model definition . . . 57
5.1.1 Loading conditions . . . 58
5.2 Eigenfrequency maximization with a volume constraints . . . 59
5.2.1 Problem definition . . . 59
5.2.2 Results and discussion . . . 61
5.3 Eigenfrequency maximization under a distributed load with volume and stress constraints . . . 64
5.3.1 Problem formulation . . . 64
5.3.2 Results and discussion . . . 65
5.3.3 Reduced allowable stress . . . 69
5.4 Eigenfrequency maximization under multiple loads with volume and stress constraints . . . 75
5.4.1 Problem formulation . . . 75
5.4.2 Results and discussion . . . 76
5.5 Comparison of the three-dimensional optimization cases . . . 80

6 Application on an industrial case **83**
6.1 General description of the industrial case . . . 83
6.2 Industrial case analysis . . . 84
6.3 Baseline design domain . . . 87
6.3.1 Problem formulation . . . 87
6.3.2 Results and discussion . . . 88
6.3.3 Influence of eigenfrequency maximization formulation . . . 91
6.4 Guided design domain . . . 93
6.4.1 Problem formulation . . . 93
6.4.2 Results and discussion . . . 94
6.5 Summary . . . 97

7 Conclusions and perspectives **98**

List of Figures

1.1 Advanced propulsion architectures: (a) UHBR and (b) BLI, (c) unducted fan. Adapted from König [2] for (a), (b) and GE Aerospace [3] for (c). 12

2.1 Conventional techniques used to generate non-axial flow: (a) turned vanes system, (b) Delta wing assembly, (c) CAD model for swirl chamber. Adapted from Hoopes (2023) [5]. 15
2.2 StreamVane distortion screens developed by Hoopes (2013): (a) manufactured bulk swirl screen; (b) CAD for generic twin-vortex case; (c) CAD for serpentine inlet application; (d) CAD for hybrid wing body (HWB) StreamVane screen. Adapted from Hoopes (2013) [5]. 16
2.3 StreamVane method results comparison in reduced and full scale experiments. Normalized axial velocity, secondary velocity vectors and swirl angle contours present similar results in both cases, demonstrating the applicability and scalability of the method. Adapted from Guimarães (2018) [10]. 17
2.4 Schematic representation of an arbitrary FSI domain used in density-based topology optimization. Adapted from Lundgaard et al. (2018) [12] 18
2.5 *The wall problem* schematic. Adapted from Lundgaard et al. (2018) [12]. 19
2.6 Changing v to modify the Reynolds number vs changing μ to modify the Reynolds number. Adapted from Abdelhamid et al. (2023) [13]. 20
2.7 General workflow for nonlinear flutter analysis. Adapted from Jonsson et al. (2019) [14]. 22
2.8 *Pk*- method applied to turbomachinery. Adapted from Schuff [17] 23

3.1 NACA 9410 airfoil. Adapted from Airfoil Tools [18]. 25
3.2 Geometry of the extruded blade based on the NACA 9410 airfoil in XY-plane and extruded 2.4 chord lengths along the Z-axis 25
3.3 First six mode shapes of the blade 27
3.4 Fluid domain - top view 28
3.5 Fluid domain - side view 28
3.6 Cross-sectional views of the mesh used in CFD simulation: a) slice in the xy plane emphasizing the boundary layers of the blade and walls walls, b) slice in xz plane emphasizing the blade boundary layer, c) slice in yz plane emphasizing the walls boundary layer 30
3.7 Mach number distribution in the computational domain for the prescribed $M_{inlet} = 0.576$ 30
3.8 Mach number distribution in the computational domain for the prescribed $M_{inlet} = 0.23$ 31
3.9 Convergence history of the CFD simulation with a prescribed $M_{inlet} = 0.23$ . . . 31
3.10 Extracted pressure distribution at blade interface obtained from the CFD simulation with prescribed $M_{inlet} = 0.23$ 32

4.1 Two-dimensional topology optimization configuration - NACA 9410 airfoil with its corresponding surrounded domain . . . 33
4.2 Finite element mesh of the $2D$ topology optimization configuration . . . 34
4.3 Comparison of the CFD and mapped pressure distributions on the extracted $2D$ section . . . 36
4.4 Design domain and boundary conditions for the $2D$ topology optimization problem - case 1 . . . 37
4.5 $2D$ density based topology optimization result (objective: maximize the first three eigenfrequencies, constraint: retain 10 % of the initial volume) . . . 39
4.6 $2D$ density based optimization - maximizing eigenfrequencies objective evolution with respect to the iterations - case 1 . . . 40
4.7 $2D$ density based optimization - volume constraint evolution with respect to the iterations - case 1 . . . 40
4.8 $2D$ density based optimization - first three natural frequencies evolution with respect to the iterations - case 1 . . . 41
4.9 Design domain and boundary conditions for the $2D$ topology optimization problem - case 2 . . . 42
4.10 $2D$ density based topology optimization result (objective: maximize eigenfrequencies, constraint 1: retain 10% of the initial volume, constraint 2: stresses should be below the allowable value $\sigma_{allowable} = 32.5\,MPa$) . . . 43
4.11 $2D$ density based optimization - maximizing eigenfrequencies objective evolution with respect to the iterations - case 2.1 . . . 44
4.12 $2D$ density based optimization - volume constraint evolution with respect to the iterations - case 2.1 . . . 45
4.13 $2D$ density based optimization - stress constraint evolution with respect to the iterations - case 2.1 . . . 45
4.14 $2D$ density based optimization - first three natural frequencies evolution with respect to the iterations - case 2.1 . . . 45
4.15 $2D$ density based optimization - comparison between stress fields at iteration 0 and 100 - case 2.1 . . . 45
4.16 $2D$ density based optimization - obtained result with different parameters for scaling . . . 46
4.17 $2D$ density based optimization (objective: maximize eigenfrequencies, constraint 1: retain 10 % of the initial volume, constraint 2: stresses should be below the allowable value $\sigma_{allowable} = 0.3\,MPa$) . . . 48
4.18 $2D$ density based optimization - maximizing eigenfrequencies objective evolution with respect to the iterations - case 2.2 . . . 48
4.19 $2D$ density based optimization - volume constraint evolution with respect to the iterations - case 2.2 . . . 48
4.20 $2D$ density based optimization - stress constraint evolution with respect to the iterations - case 2.2 . . . 49
4.21 $2D$ density based optimization - first three natural frequencies evolution with respect to the iterations - case 2.2 . . . 50
4.22 $2D$ density based optimization - comparison between stress fields at iteration 0 and 100 - case 2.2 . . . 50
4.23 $2D$ density based optimization with multiple loads (objective: maximize eigenfrequencies, constraint 1: retain 10 % of the initial volume, constraint 2: stresses should be below the allowable value $\sigma_{allowable} = 32.5\,MPa$) . . . 52
4.24 $2D$ density based optimization - maximizing eigenfrequencies objective evolution with respect to the iterations - case 3 . . . 52

4.25 $2D$ density based optimization - volume constraint evolution with respect to the iterations - case 3 . . . 53
4.26 $2D$ density based optimization - stress constraint evolution with respect to the iterations - case 3 . . . 53
4.27 $2D$ density based optimization - first three natural frequencies evolution with respect to the iterations - case 3 . . . 53
4.28 $2D$ density based optimization - comparison between stress fields at iteration 0 and 100 - case 3 . . . 54
4.29 $2D$ density based optimizations - comparison between *case (a)* (eigenfrequency maximization and volume constraint), *case (b)* (addition of the stress constraint - $\sigma_{allowable} = 32.5\,MPa$), *case (c)* (reduced allowable stress - $\sigma_{allowable} = 0.3\,MPa$) and *case (d)* (multiple-load - $\sigma_{allowable} = 32.5\,MPa$) . . . 55

5.1 Three-dimensional topology optimization configuration - a) NACA 9410 airfoil extruded $2.4\,c$ with its corresponding surrounding domain, b) clamped regions containing four surfaces and the bottom surface of the blade . . . 57
5.2 Blade faces created for the CFD pressure projection . . . 58
5.3 Comparison between a) CFD pressure at the interface and b) resulted pressure distribution using the projection . . . 60
5.4 Design domain and boundary conditions for the $3D$ topology optimization problem - case 1 . . . 60
5.5 $3D$ density based topology optimization result (objective: maximize the first three eigenfrequencies, constraint: retain 10 % of the initial volume) - a) front view, b) lateral view 1, c) lateral view 2, d) top view with [0.5, 1] retained densities. 62
5.6 $3D$ density based optimization - maximizing eigenfrequencies objective evolution with respect to the iterations - case 1 . . . 63
5.7 $3D$ density based optimization - volume constraint evolution with respect to the iterations - case 1 . . . 63
5.8 $3D$ density based optimization - first three natural frequencies evolution with respect to the iterations - case 1 . . . 63
5.9 First three mode shapes of the obtained geometry with [0.5, 1] retained - case 1 64
5.10 $3D$ density based topology optimization result (objective: maximize the first three eigenfrequencies, constraint: retain 10 % of the initial volume, stresses should be below an allowable value $\sigma_{allowable} = 32.5\,MPa$) - a) front view, b) lateral view 1, c) lateral view 2, d) top view with [0.5, 1] retained densities. . . . 66
5.11 $3D$ density based optimization - maximizing eigenfrequencies objective evolution with respect to the iterations - case 2.1 . . . 66
5.12 $3D$ density based optimization - volume constraint evolution with respect to the iterations - case 2.1 . . . 67
5.13 $3D$ density based optimization - stress constraint evolution with respect to the iterations - case 2.1 . . . 67
5.14 $3D$ density based optimization - first three natural frequencies evolution with respect to the iterations - case 2.1 . . . 67
5.15 $3D$ density based optimization - comparison between stress fields at iteration 0 and 100 - case 2.1 . . . 68
5.16 $3D$ density based optimization - comparison between displacement at (a) iteration 0 and (b) iteration 100 - case 2.1 . . . 69
5.17 First three mode shapes of the obtained geometry with [0.5, 1] retained - case 2.1 70

5.18 $3D$ density based topology optimization result (objective: maximize the first three eigenfrequencies, constraint: retain 10 % of the initial volume, stresses should be below an allowable value $\sigma_{allowable} = 0.3\,MPa$) - a) front view, b) lateral view 1, c) lateral view 2, d) top view with [0.5, 1] retained densities. . . . 71
5.19 $3D$ density based optimization - maximizing eigenfrequencies objective evolution with respect to the iterations - case 2.2 72
5.20 $3D$ density based optimization - volume constraint evolution with respect to the iterations - case 2.2 72
5.21 $3D$ density based optimization - stress constraint evolution with respect to the iterations - case 2.2 72
5.22 $3D$ density based optimization - first three natural frequencies evolution with respect to the iterations - case 2.2 73
5.23 $3D$ density based optimization - comparison between stress fields at iteration 0 and 130 - case 2.2 74
5.24 $3D$ density based optimization - comparison between displacement at (a) iteration 0 and (b) iteration 100 - case 2.2 74
5.25 First three mode shapes of the obtained geometry with [0.5, 1] retained - case 2.2 75
5.26 $3D$ density based topology optimization result with multiple load applied (objective: maximize the first three eigenfrequencies, constraint: retain 10 % of the initial volume, stresses should be below an allowable value $\sigma_{allowable} = 32.5\,MPa$) - a) front view, b) lateral view 1, c) lateral view 2, d) top view with [0.5, 1] retained densities. 77
5.27 $3D$ density based optimization - maximizing eigenfrequencies objective evolution with respect to the iterations - case 4 77
5.28 $3D$ density based optimization - volume constraint evolution with respect to the iterations - case 3 78
5.29 $3D$ density based optimization - stress constraint evolution with respect to the iterations - case 3 78
5.30 $3D$ density based optimization - first three natural frequencies evolution with respect to the iterations - case 3 78
5.31 $3D$ density based optimization - comparison between stress fields at (a) iteration 0 and (b) iteration 130 - case 3 79
5.32 $3D$ density based optimization - comparison between displacement at (a) iteration 0 and (b) 100 - case 3 80
5.33 First three mode shapes of the obtained geometry with [0.5, 1] retained - case 3 80
5.34 $3D$ density based optimizations - comparison between *a)* (eigenfrequency maximization and volume constraint), *b)* (addition of the stress constraint - $\sigma_{allowable} = 32.5\,MPa$), *c)* (reduced allowable stress - $\sigma_{allowable} = 0.3\,MPa$) and *d)* (multiple-load - $\sigma_{allowable} = 32.5\,MPa$) 81

6.1 Velocity field used for preliminary design (a) and turning vanes system (b). Adapted from Grondin [21] 83
6.2 Comparison between the target swirl angle α and the obtained result using CFD simulation. Adapted from Grondin [21]. 84
6.3 Swirl device geometry: a) front view, b) lateral view, c) top view 84
6.4 Swirl device geometry: clamped surfaces 85
6.5 Mode shapes 1, 2, 3 for the industry application 86
6.6 Mode shapes 4, 5, 6 for the industry application 86
6.7 Geometry used in the topology optimization process - baseline case 87

6.8 $3D$ density based optimization result (objective: maximize the first three eigenfrequencies, constraint: retain 10 % of the initial volume) - a) front view, b) lateral view with [0.5, 1] retained densities, baseline case 89
6.9 $3D$ density based optimization - maximizing eigenfrequencies objective evolution with respect to the iterations - baseline case 89
6.10 $3D$ density based optimization - volume constraint evolution with respect to the iterations - baseline case 89
6.11 $3D$ density based optimization - first three natural frequencies evolution with respect to the iterations - baseline case 90
6.12 First three mode shapes of the obtained geometry with [0.5, 1] retained densities - baseline case 90
6.13 Topology optimization result - maximization of the first eigenfrequency, retained densities [0.8, 1] 91
6.14 First three mode shapes of the obtained geometry with [0.8, 1] retained densities - first eigenfrequency maximization 92
6.15 Topology optimization result - maximization of the second and third eigenfrequencies, retained densities [0.8, 1] 93
6.16 First three mode shapes of the obtained geometry with [0.8, 1] retained densities - second and third eigenfrequencies maximization 93
6.17 Geometry used in topology optimization process - guided design case 94
6.18 $3D$ density based optimization result (objective: maximize the first three eigenfrequencies, constraint: retain 10 % of the initial volume) - a) front view, b) lateral view with [0.5, 1] retained densities - guided design domain case 95
6.19 $3D$ density based optimization - maximizing eigenfrequencies objective evolution with respect to the iterations - guided design case 96
6.20 $3D$ density based optimization - volume constraint evolution with respect to the iterations - guided design case 96
6.21 $3D$ density based optimization - first three natural frequencies evolution with respect to the iterations - guided design case 96
6.22 First three mode shapes of the obtained geometry with [0.5, 1] retained densities - guided design case 97

List of Tables

3.1 Material properties 26
3.2 First six natural frequencies 27

4.1 Obtained force components for the three axes 35
4.2 Distributed force for the three axes 35
4.3 Natural frequencies - case 1 41
4.4 Scaling parameters -1 43
4.5 Natural frequencies - case 2.1 45
4.6 Scaling parameters -2 46
4.7 Natural frequencies - case 2.2 50
4.8 Scaling parameters - 3 51
4.9 Natural frequencies - case 3 53

5.1 Natural frequencies - case 1 63
5.2 Natural frequencies - case 2.1 67
5.3 Natural frequencies - case 2.2 73
5.4 Natural frequencies - case 3 78

6.1 First six natural frequencies - industry application 86
6.2 Scaling parameters - 4 88
6.3 Natural frequencies - baseline case 90
6.4 Scaling parameters - 5 94
6.5 Natural frequencies - guided design case 96

Chapter 1

Introduction

1.1 Context

The aviation industry is introducing new technologies in order to reduce the carbon footprint such as Ultra High Bypass Ratio (UHBR), Boundary Layer Ingestion (BLI) or unducted fan architectures, illustrated in fig. 1.1. These configurations are able to increase the aircrafts efficiencies but new challenges may arise, such as the increase level of the flow distortion at the engine inlet. Engine testing under a non-uniform flow is crucial since it has a high impact on engine performance and operability and the need of ground testing facilities have arisen [1].

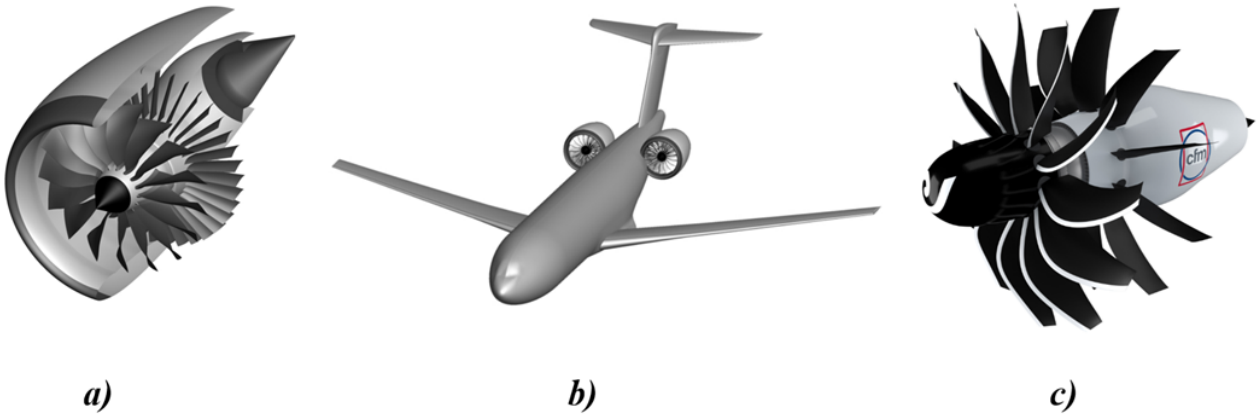


Figure 1.1: Advanced propulsion architectures: (a) UHBR and (b) BLI, (c) unducted fan. Adapted from König [2] for (a), (b) and GE Aerospace [3] for (c).

In earlier work, systems such as turning vanes and delta wings that were capable of reproducing simple distortion flow fields were used, but with the current technologies, more complex flow patterns are needed in order to evaluate the overall performance and stability of the engine [4, 5].

The primary objective of such system is to generate the desired distortion pattern, but during operation, the blades are subjected to high pressure loadings that may affect the dynamic behavior and even induce deformations. Therefore, an additional step is needed in order to ensure that the mechanical integrity is preserved and topology optimization can be used since it is able to explore unconventional geometrical configurations and approaches, while allowing the coupling of multi-physics problems [6]. In the context of the present work, using a Cenaero in-house software - Morfeo (Manufacturing Oriented Finite Element tOol), a topology optimization

approach is tested on a simplified case while treating only mechanical constraints. This ensures that the problem complexity remain relatively low, while still preserving the main characteristics of the complex system. The methodology is applied afterwards on an industrial case and its capabilities are analyzed.

1.2 Objectives

The main objective of this work is to develop and assess a workflow using topology optimization of a distortion grid system based on mechanical constraints in order to improve the structural performances. To achieve this objective, the following specific goals are defined:

- define a simplified geometry that is capable to reproduce the main characteristics of the distortion grid system;
- perform a CFD simulation using the simplified case in order to obtain the aerodynamic pressure at the interface that can be used to define the mechanical loads;
- define the topology optimization framework based on eigenfrequencies maximization and volume constraints in order to increase the stiffness of the structure;
- investigate the influence of the aerodynamic loads over the structure and demonstrate that the stresses can be reduced using the proposed framework;
- assess the proposed methodology and analyze the effects of different optimization parameters;
- apply the developed methodology on an industrial case and evaluate the capabilities of the proposed approach.

1.3 Structure of the report

The contents of this thesis is organized in 6 chapters. Chapter 2 reviews the current state of the available technologies and methods, along with a presentation of the topology optimization capabilities. Chapter 3 presents the selected simplified geometry and the corresponding modal and CFD analysis that are used to set the topology optimization framework. Chapter 4 is based on a two-dimensional topology optimization where four cases are treated. The first one is based on eigenfrequencies optimization while taking into account a volume constraint, the second one introduces a stress constraint, the third one lowers the maximum allowable limit in order to analyze its influence and the last one presents a more realistic loading scenario. Chapter 5 described four three-dimensional topology optimizations, where the same cases that were treated in the Chapter 3 are directly transferred in the $3D$ formulations. Chapter 6 presents the developed topology optimization framework applied on an industrial application and the corresponding results are analyzed. Finally, Chapter 7 summarizes the main findings and conclusions of the work and discusses the limitations and future improvements.

Chapter 2

Bibliography

2.1 Design of distortion grids

For an aircraft engine, an uniform flow field is preferable while entering the fan or first compressor stages. However, in practice, variations in total temperature, velocity and pressure are observed. This effect is called distortion and the main concern related to it is the stability of the compressor system because of the potential of stall and surge. These effects can cause losses in thrust and reduced efficiencies [4].

In Kurzke and Halliwel book [4], two types of distortion are presented: total pressure distortion and total temperature distortion. To begin with, the total pressure distortion can be caused by the flow separation at curved inlet ducts or flow detachment at the intake lip due to hight angles of attack, while total temperature distortion is associated with thermal non-uniformities and it is highly relevant for military applications [4]. Moreover, another important distortion is the swirl distortion that represents the angular variations of the incoming velocity vector. In practice, these effects are dependent on the flight conditions and can also occur simultaneously.

Theoretically, in a compressor row, all the blades have the same geometry and they are specifically designed to generate an amount of pressure rise [5]. When the compressor receives a non-uniform flow due to distortion, the blades are operating in an off-design condition, affecting the performance of the compressor and also lowering the surge margin. Another effect that is caused by the distortion is the non-uniform blade loading, which can eventually cause fatigue and damage [5].

One method to model the distortion effects is the parallel compressor theory and it is used to analyze the stability and performance of the system. This method consists of two compressors working in parallel, using two streams with uniform and different total pressures [4].

During the development phase of a new engine design, the distortion effects are also evaluated using dedicated ground-systems. The aim of these systems is to reproduce non-uniform flow fields in order to evaluate the performance of the fan and compressor under realistic operating conditions. The current interest in new technologies such as boundary layer ingestion increases the need for advanced distortion generators that are capable of reproducing complex and realistic swirl patterns. Currently, devices capable in reproducing distortion patterns such as grids, screens or tailored vane assemblies are installed upstream the compressor [5]. Additionally, several research organizations such as Virginia Tech [7], NASA Langley [8] or University of Defense [9] designed or evaluated distortion grids for aircraft engine testing.

2.2 Conventional distortion generators and design methodologies

In this context, some conventional techniques were developed to create a non-axial flow: turned vanes, delta-wing vortex generators and swirl chambers [5]. Genssler et al. presented two of these devices, a turned vanes system and a delta wing, while Sheoran and Bouldin conduced studies on the swirl chamber [5].

The turned vane system consists of multiple oriented blades that are placed upstream the compressor, imposing in this way a circumferential flow component. Because of their configuration, these devices can produce a relatively uniform flow, rather than a more complex swirl pattern [5]. Delta-wing generators at an angle of attack can create a pair of rotating vortices and they are preferable because they are relatively easy to manufacture. Another advantage for these systems is that the vortices are adjustable, offering more control on the flow patterns. In contrast, a more complex system is the swirl chamber [5]. This option relies on creating a plenum with adjustable doors and using these features, the flow can enter at specific angles, creating some rotating flow patterns [5]. These devices are presented in fig. 2.1.

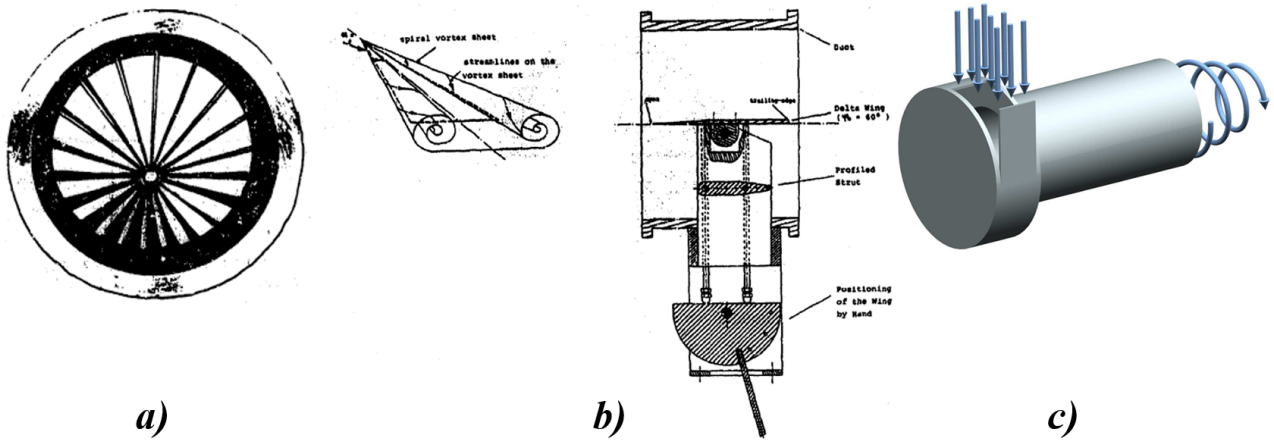


Figure 2.1: Conventional techniques used to generate non-axial flow: (a) turned vanes system, (b) Delta wing assembly, (c) CAD model for swirl chamber. Adapted from Hoopes (2023) [5].

The limitation arises from the fact that the generated patterns are relatively simplistic. The need for devices that are capable of reproducing more complex swirl pattern arises because of the future concepts that are introduced in the engine design. In this direction, Hoopes described a method that is capable of producing arbitrary profiles called the StreamVane method [5]. This method presents a considerable advantage since, for a given velocity, the method is capable of creating a device that can replicate the non-uniform flow pattern while testing. Thus, the method starts by using a velocity field vector at the aerodynamic interface plane (AIP). Using this profile, the lines are created perpendicular to the local velocity direction and consequently, the vanes are placed along these paths. After this step, the blades sections are defined by taking into account the local turning angle and from a mechanical point of view, additional supports may be added in order to increase the rigidity of the structure. Following this developing process, the device can be manufactured using additive manufacturing [5].

To demonstrate the versatility of the method, the Hoopes' paper aims to validate multiple devices that were created. The developed and tested configurations are presented in fig. 2.2.

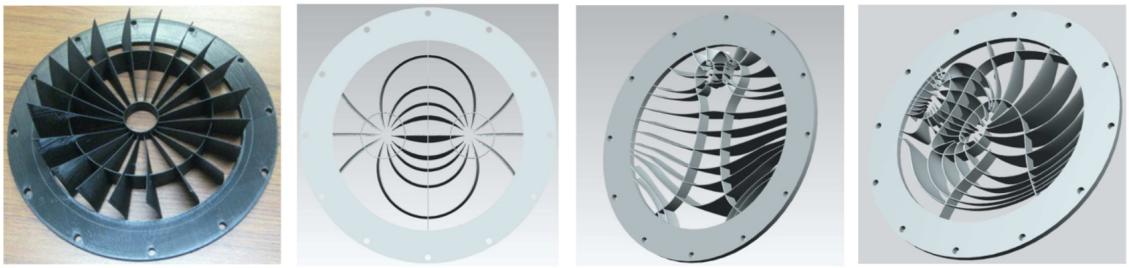


Figure 2.2: StreamVane distortion screens developed by Hoopes (2013): (a) manufactured bulk swirl screen; (b) CAD for generic twin-vortex case; (c) CAD for serpentine inlet application; (d) CAD for hybrid wing body (HWB) StreamVane screen. Adapted from Hoopes (2013) [5].

The devices testing was conducted in a low-speed tunnel and the results displayed a good agreement with the given velocity field [5]. Therefore, the StreamVane method was capable of reproducing several patterns, but further investigation was needed in order to confirm that this method is also effective on a real scale turbofan inlet, where the rotating parts and turbulence also influence the flow. For this, in the studies conducted by Guimarães et al. [7], this method was tested in a 6 inch wind tunnel and also in a full scale Pratt & Whitney JT15-D research engine [7]. For this purpose, the Stereoscopic Particle Image Velocity (PIV) was used. With it, the measurement of axial, tangential, radial, swirl and turbulence quantities could be recorded. The comparison between target and measured field revealed a good agreement and thus, the method is capable of reproducing realistic patterns during the ground-testing. Additionally, the PhD thesis of Guimarães demonstrated that the swirl is mainly influenced by two-dimensional vortex dynamics, mainly because these vortices can convect or reshape the secondary flow [7].

In addition to its advantages, the StreamVane method also introduces local boundary layer interactions, wake losses, blockages. Because of this aerodynamic effects, the geometry of the blade needs to be optimized in order to balance the capability to reproduce complex distortion patterns, mechanical rigidity and pressure losses [7].

Another important finding is emphasized in the thesis, since the small and full scale tests were available. It was observed that the swirl distortion is independent of Mach number, while the Reynolds effects are also limited, reinforcing the usage of reduced scale models in preliminary design phases [7]. A comparison between the small and large scale is shown in fig. 2.3.

2.3 Topology optimization for distortion grid design

The previous section described a method that is flexible and can create systems of blades that are capable of producing non-uniform flows fields during ground testing. Besides this main objective, other aspects such as mechanical integrity or manufacturability should be taken into account. To address these effects, the topology optimization can be used, as it offers a platform of integration of all aspects for defining a preliminary design. In turbomachinery, the blades operate in an aerodynamic environment and therefore the flow is influencing the performance, stability and also loadings. To achieve the coupling between aerodynamical and mechanical aspects, Computational Fluid Dynamics (CFD) can be used in order to evaluate and maintain aerodynamic performances, but, in parallel, the aeroelastic phenomena should also be considered. Thus, for this type of problems, the topology optimization enables the

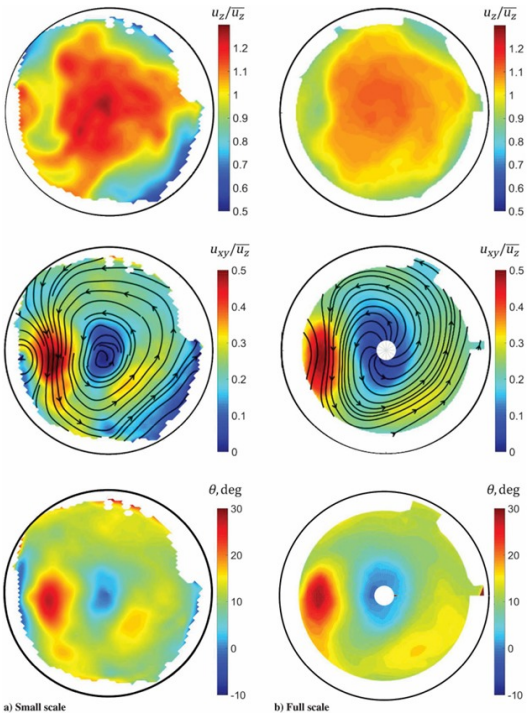


Figure 2.3: StreamVane method results comparison in reduced and full scale experiments. Normalized axial velocity, secondary velocity vectors and swirl angle contours present similar results in both cases, demonstrating the applicability and scalability of the method. Adapted from Guimarães (2018) [10].

coupling between mechanical and aerodynamic aspects, ensuring that the performances are achieved, while the mechanical integrity is preserved.

A review paper done by He Li et al. [6] offers a perspective on topology optimization applied to systems that are governed by flow equations. For the explicit methods, a widely used option is represented by the density based topology optimization. For it, the densities values are continuously updated until the configuration meets the objective, while satisfying the imposed constraints. On the other hand, for the implicit methods, the level-set is used in order to obtain smoother and clearer boundaries. The paper also emphasizes the challenges met when the optimization process is done under turbulent flow conditions, where numerical stability influences the quality of the final design. In contrast, recent trends introduce manufacturability constraints or also machine learning assisted processes [6].

J. Meng et al. [11] used it in order to optimize a hollow wide-chord fan blade used in a turbofan engine. The optimizable domain is represented by the blade's internal domain, while the outer structure remained unchanged since this is what gives the desired aerodynamic performances. In this specific case, the problem was mainly structural, since the outer structured was not modified, eliminating the need of several CFD simulations. In the presented study, several loading cases were considered such as static strength, vibration, bird strike, while critical stresses were found at the blade root. During the optimization, the frequency margin increased from 0.35% to 10.7% [11] .This study presented a case where the main focus was on stresses reduction, while the frequency constraint was relevant from an aeroelastic perspective, since the blade natural frequencies and mode shapes strongly influence the flutter.

A relevant study for multi-physics problems is the Lundgaart paper [12]. The study investigated a density based topology optimization approach for fluid-structure interactions (FSI), solving the Navier-Stokes equations for the fluid domain and the Navier-Cauchy equations for structural domain using finite element method (FEM). The aerodynamic component of the blade is analyzed concerning the fact that the blade's deformation also affects the structural response [12]. A generic FSI problem used in a density based approach is presented in fig. 2.4.

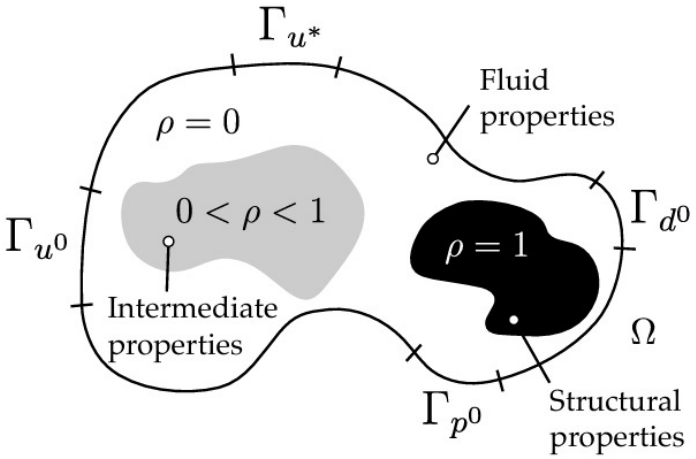


Figure 2.4: Schematic representation of an arbitrary FSI domain used in density-based topology optimization. Adapted from Lundgaard et al. (2018) [12]

Figure 2.4 presents a main domain denoted Ω which accommodates two sub-domains, solid and fluid. The region where the design variable $\rho = 1$ represents the solid domain, while the zone that displays $\rho = 0$ represents the fluid domain. A transition domain is seen for intermediate properties, where $0 < \rho < 1$. This region is often penalized such that, during a density based optimization, there is a clean separation between fluid and solid zones. The boundaries are noted with Γ, both for structural and fluid domain, where prescribed conditions can be applied. The paper empathizes that, for a density based problem, a Brinkman penalization term $\alpha(\rho)\mathbf{v}$ is introduced to the momentum equation, while the structural stiffness $E(\rho)$ is interpolated as a function of design variables. When $\rho = 1$, the Brinkman penalization term imposed a velocity equal to zero to the fluid, while for $\rho = 0$, a pure fluid flow is imposed [13].

As stated in the study, for a viscous, incompressible and stead flow, the Navier-Stokes governing equation can be written [13]:

$$\left.\begin{aligned} \nabla \cdot \mathbf{v} &= 0, \\ \rho_f(\mathbf{v} \cdot \nabla)\mathbf{v} &= \nabla \cdot \boldsymbol{\sigma}^f + \mathbf{f}^f - \alpha(\rho)\mathbf{v}, \\ \boldsymbol{\sigma}^f &= -p\mathbf{I} + \mu\left[\nabla\mathbf{v} + (\nabla\mathbf{v})^T\right], \\ \alpha(\rho) &= \alpha_{\max} + (1-\rho)(\alpha_{\min} - \alpha_{\max})\tfrac{1+p_\alpha}{1-\rho+p_\alpha} \end{aligned}\right\} \quad \Omega_f, \tag{2.1}$$

with $\mathbf{v}$ as the fluid velocity, μ as fluid dynamic viscosity, p as hydrostatic pressure, σ^f as Cauchy fluid stress tensor, $\mathbf{f}^f$ as the external fluid force, while the inverse permeability $\alpha(p)$, as it is called in paper of M. Abdelhamid [13], represents the Brinkman penalization parameter with its corresponding α_{min} and α_{max} [13].

In contrast, the Navier-Cauchy governing equations can be written under linear elasticity assumptions with infinitesimal deformations in a steady state frame as [13]:

$$\left.\begin{aligned} \nabla \cdot \sigma^s + \mathbf{f}^s = 0, \\ \sigma^s = \mathbf{C}^s \epsilon, \\ \epsilon = \tfrac{1}{2}[\nabla \mathbf{u} + (\nabla \mathbf{u})^T], \\ E(\rho) = E_{min} + (E_{max} - E_{min})\rho^{pE} \end{aligned}\right\} \quad \Omega_s, \tag{2.2}$$

with σ^s as the Cauchy solid stress tensor, ϵ as the strain tensor, $\mathbf{f}^s$ as the external solid force, $\mathbf{C}^s$ as the solid elasticity tensor, while the elastic modulus E is interpolated using the SIMP (Solid Isentropic Material Penalization) approach [13].

Based on Lundgaard's paper [12], the boundary conditions can be defined as:

$$\begin{aligned} \text{No slip fluid:} \quad & u_i = {u_i}^0 = 0 \quad \text{on} \quad \Gamma_{u_0}, \\ \text{Fluid inflow:} \quad & u_i = {u_i}^* \quad \text{on} \quad \Gamma_{u^*}, \\ \text{Fluid outflow:} \quad & p = p^0 = 0 \quad \text{on} \quad \Gamma_{p^0}, \\ \text{Structural displacement:} \quad & d_i = {d_i}^0 = 0 \quad \text{on} \quad \Gamma_{d_0}. \end{aligned} \tag{2.3}$$

The previous description emphasizes that the elements that have design variables $\rho = 1$ are governed by the structural equations, while the elements with $\rho = 0$ are governed by the fluid equations. For any elements that have intermediate values $0 < \rho < 1$, a state between fluid and solid structure is present [12].

A well known problem in the literature called *the wall problem* was described by both Lundgaard et al. [12] and also by Abdelhamaid et al. [13]. The structure is exposed to aerodynamic loading and the problem's objective is to minimize its structural compliance, while a 10% volume constraint is imposed. The problem schematics is presented in fig. 2.5.

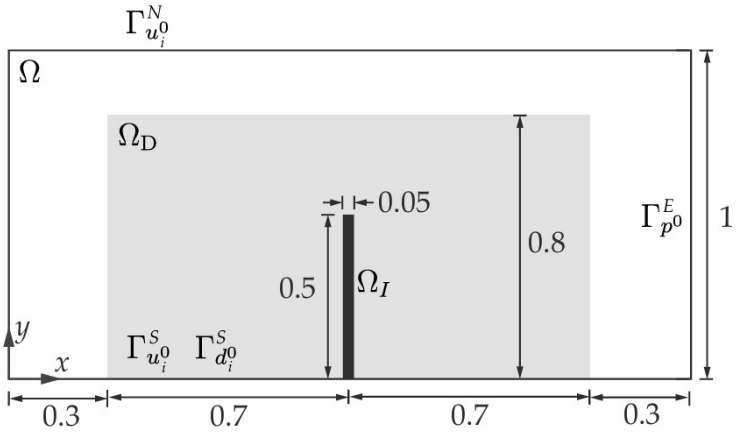


Figure 2.5: *The wall problem* schematic. Adapted from Lundgaard et al. (2018) [12].

The domain Ω presented in the picture illustrates the wall, where the design variables ρ are set to 1, while the domain Ω_D is a fixed domain. Additionally, several boundary conditions are prescribed: Γ_u^N as a Neumann condition for the fluid, Γ_d^S as a structural Dirichlet condition, Γ_f^S as a structural condition imposing a structural load and $\Gamma_{p^0}^E$ as a pressure prescribed boundary.

In the Lundgaard et al. [12] paper, the influence of four Reynolds numbers was investigated ($Re = \{1, 5, 10, 40\}$), where the Reynolds number is defined as $Re = (v_C \cdot \rho \cdot L_C)/\mu$, with v_c as characteristic velocity, ρ as fluid density, L_C as characteristic length and μ as dynamix viscosity of the fluid [12]. In Abdelhamaid et al. [13] paper, the influence of several parameters is examined (Brinkman penalization parameter p_α, Young's modulus penalization parameter p_E and pressure-coupling parameter p_γ), demonstrating their strong influence over the optimization problem.

In Adbelhamid et al. [13] paper, different results are obtained when the Reynolds number is modified through dynamic viscosity instead of velocity [13]. The justification for this behavior can be represented by the fact that the structure loads are highly influenced by all constituent parameters, not only dependent on the Reynolds final number [13]. In fig.2.7, the effects of using v to change the Reynolds number Re instead of μ are presented.

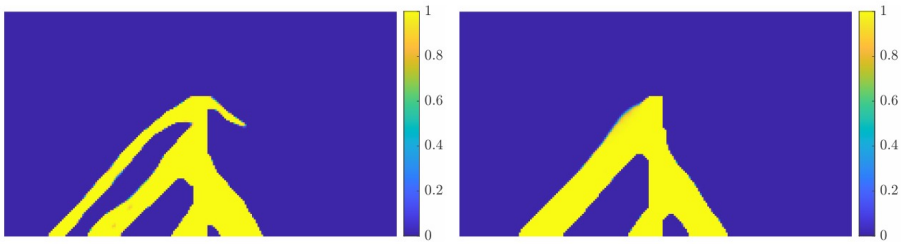


Figure 2.6: Changing v to modify the Reynolds number vs changing μ to modify the Reynolds number. Adapted from Abdelhamid et al. (2023) [13].

Therefore, Lundgaard et al. [12] and Abdelhamid et al. [13] papers are based on the same wall problem. Lundgarrd et al. [12] describes the benchmark and studies the fluid-structure-interaction problem under different conditions, while Abdelhamid [13] extends the study and changes how the fluid loads are transferred to the structure, coupling pressure with viscous stresses.

2.4 Flutter assessment

In the context of designing distortion grid systems using topology optimization, the flutter constraints are not taken into account. Hence, this section aims to introduce some numerical methods used in flutter assessment.

In an article published in 2019 by E. Jonsson et al. [14], the flutter and its corresponding analysis are presented. Essentially, the flutter is described as a dynamic instability that arises from the coupling between structural elasticity, inertial and aerodynamic forces and it can eventually cause damage or even failure. For the flutter analysis, two categories of methods are available: eigenvalue analysis method and direct method.

The direct method is based on Hopf-bifurcation approach and it directly computes the flutter point [14]. Starting from a generic nonlinear system [14]:

$$\dot{x} = f(x; U), \tag{2.4}$$

where the state vector $x = [q^T, \dot{q}^T]$ includes the generalized coordinates and U represents the flight speed, the bifurcation point is found using the equilibrium state x_F and the critical flight speed U_F such that $f(x_F, U_F) = 0$. The critical eigenvector is described as [14]:

$$(A - iI\omega_F)\, u = 0, \tag{2.5}$$

where $A(x_F, U_F)$ represents the Hopf point, $u = u_r + iu_i$ is the complex eigenvector, I is the identity matrix and ω_F is the angular frequency. Therefore, the corresponding flutter point is the solution of the non-linear system [14]:

$$F(X) = 0, \qquad X = \begin{bmatrix} x_F^T & u_r^T & u_i^T & U_F & \omega_F \end{bmatrix}^T. \tag{2.6}$$

For the eigenvalue method, the equations of motion for a generalized system subjected to aerodynamic loading F_{aero} can be written as [14]:

$$M\ddot{u}(t) + Ku(t) - F_{\text{aero}}(t) = 0, \tag{2.7}$$

where M and K represent the structural and stiffness matrices respectively, while u is the displacement vector for a system with N degrees of freedom. Because usually the number of degrees of freedom is large, a reduced model with a reduced number of degrees of freedom $N_r < N$ can be used in order to reduce the computational cost.

The displacement field can be written using the modal reduction as [14]:

$$u \approx \Phi_r q, \tag{2.8}$$

where Φ_r corresponds to the r preserved mode shapes and q defines the vector of generalized modal coordinates. Using this relation, the equation of motion for a reduced model can be written as [14]:

$$M_r\ddot{q}(t) + K_r q(t) - F_{\text{aero},r}(t) = 0, \tag{2.9}$$

where M_r and K_r represent the reduced mass and stiffness matrices and the vector of generalized aerodynamic forces is described as $F_{\text{aero},r} = \Phi_r^T F_{\text{aero}}$ [14].

In order to analyze the stability problem, the system's equation is written in Laplace form:

$$\left[\left(\frac{U}{b}\right)^2 p^2 M_r + K_r - q_\infty Q_r(p)\right] \hat{q}(p) = 0, \tag{2.10}$$

where Q_r corresponds to the generalized aerodynamic force matrix, q_∞ represents the dynamic pressure, $\hat{q}$ is the Laplace transform of $q(t)$, p is the Laplace variable, U is the flow speed and b defines the semi-chord. The output of this analysis is the non-dimensional Laplace variable $p = g + ik$, with g being the damping coefficient and k the reduced frequency.

Fig. 2.7 represents a general scheme of the eigenvalue method for a nonlinear flutter analysis presented in the paper [14].

In the general workflow for the stability analysis, the real part is analyzed:

$$\begin{aligned} g < 0 \;&\Rightarrow\; \text{stable}, \\ g = 0 \;&\Rightarrow\; \text{flutter boundary}, \\ g > 0 \;&\Rightarrow\; \text{unstable}. \end{aligned} \tag{2.11}$$

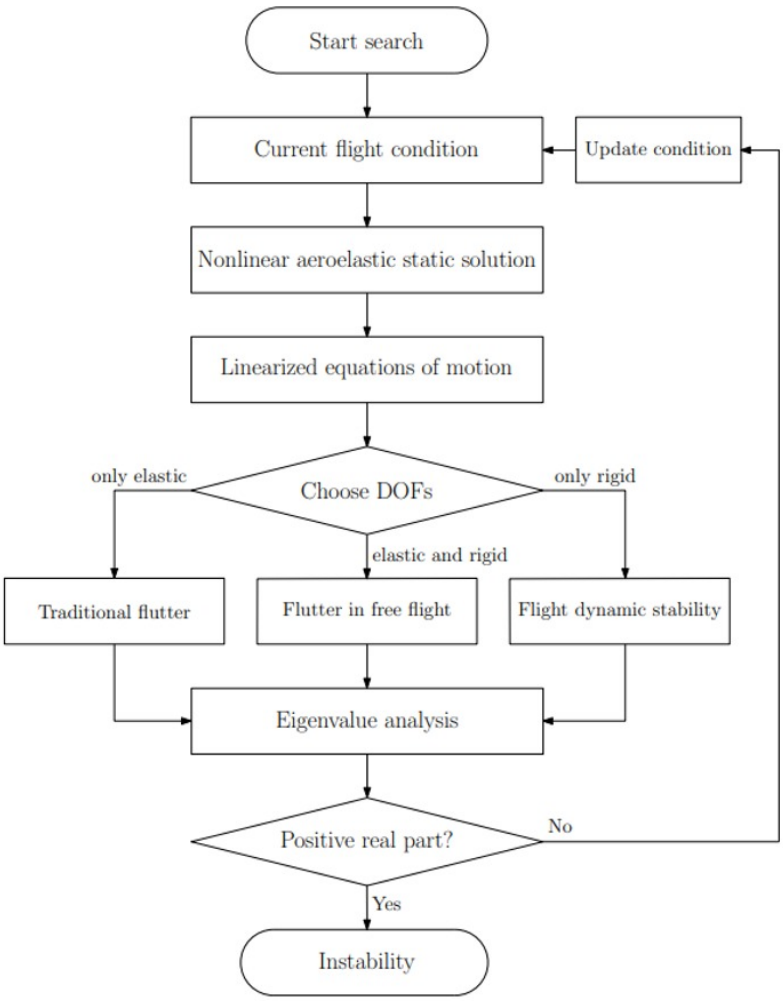


Figure 2.7: General workflow for nonlinear flutter analysis. Adapted from Jonsson et al. (2019) [14].

Due to the high computational cost of the general method presented in fig. 2.7, the need of new methods with a reduced cost has emerged. Thus, in practice, the flutter analysis is studied using several methods based on the eigenvalue analysis: *p*-, *k*-, *pk*- and *g*- [14].

For instance, the *pk*- method calculates over a range of prescribed reduced frequencies in order to address the aeroelastic stability. Therefore, by increasing the reduced frequency, the flutter stability could also be increased. The reduced frequency represents a non-dimensional form for a frequency, written as:

$$k = \frac{\omega \cdot b}{U_\infty}, \tag{2.12}$$

where b represents the semi-chord, U_∞ is the freestream velocity and ω is the circular frequency [15]. This *pk*- method is solved iteratively, but convergence issues may appear and because of this, a non-iterative option is available [16]. This non-iterative method relies on the fact that the generalized aerodynamic forces matrix is computed for the selected reduced frequencies and following this, the eigenvalue problem is resolved. At the end of the process, the interpolation is used in order to determine the eigenvalue that solves the flutter equation [16].

In Schuff's paper [17], the *pk*- method was adapted and applied to turbomachinery. Because the natural frequencies depend on the rotational speed, for each selected operating point, the flutter equation needs to be solved individually [17].

An adapted algorithm presented in Schuff's paper [17] uses a linearized aerodynamic model and frequency-domain forced-motion simulations in order to obtain the generalized aerodynamic forces. Another assumption that was made refers to assuming small perturbations around the flutter onset, while the turbomachinery adaptation takes into account the cyclic symmetry and the fact that the mode shapes and frequencies vary with rotor speed [17]. In fig. 2.8, an adaptation of the general workflow is presented. The main difference arise from the fact that, in a turbomachinery framework, the operating point is already fixed and the iterating process is used to converge the aeroelastic frequency and mode, while taking into account the aerodynamic coupling between the structural modes. However, fig 2.7 presents a generalized workflow, where the main goal is to determine whether a flight condition is stable.

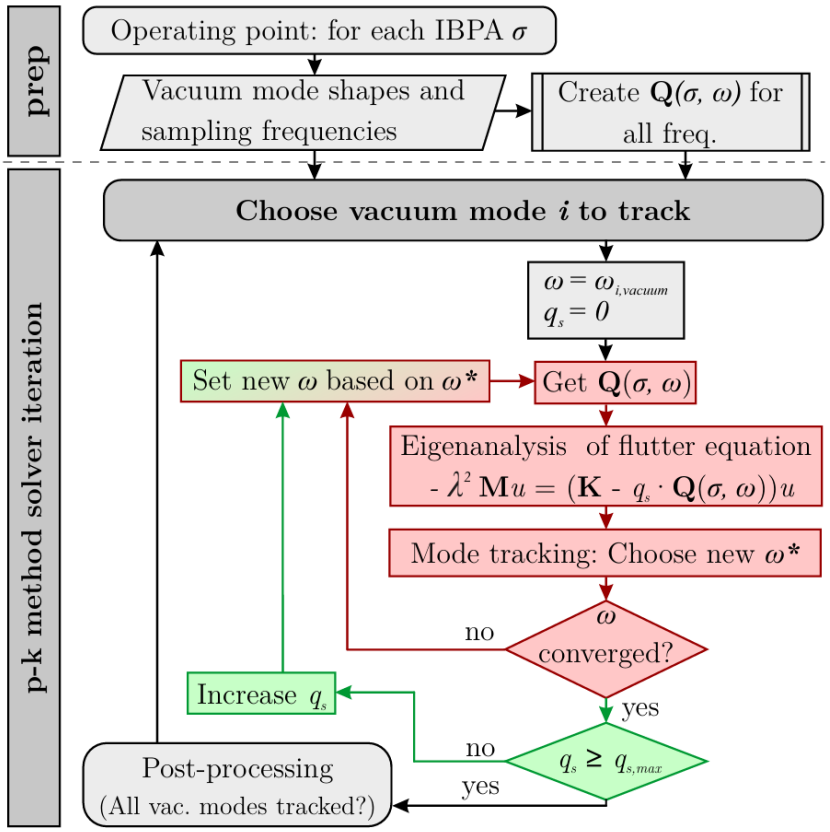


Figure 2.8: *Pk*- method applied to turbomachinery. Adapted from Schuff [17]

Chapter 3

Simplified test case definition

3.1 Motivation

In this chapter, the main objective is to develop a methodology that can increase the mechanical resistance of a distortion grid system, while still partially preserving the flow path using topology optimization. Although topology optimization is an efficient method that allows the integration of multiple constraints, the computational cost can rise in more elaborate cases and due to the complexity of the industrial distortion grid system, a simplified test case is introduced.

Therefore, the first step of this work consists of defining the simplified geometry which is selected such that it preserves the main characteristics of the distortion grid system, considering a compromise between physical relevance and computational efficiency. The modal characteristics of the structure are presented along with a detailed CFD simulation and the output is translated as mechanical constraints. The aim of this simplified test case is to validate the methodology and following this, the process is applied to an industry application case.

This section describes the geometry definition, along with its corresponding analysis - modal analysis and CFD simulation, used to determine the mechanical loads that are applied during the optimization process.

3.2 Geometry description

A distortion grid system is formed by multiple blades and typically, these blades are slender, twisted and asymmetrical. Therefore, the aim of this simplified geometry is to reproduce these characteristics, while still maintaining a relatively low computational cost.

Thus, an extruded blade based on a NACA 9410 airfoil was chosen. The airfoil is presented in fig. 3.1 and it is characterized by a 9% maximum chamber, located at 40% of the chord from the leading edge and a maximum thickness equal to 10% of the chord. This cambered airfoil is suitable for this application, having a relatively high camber and a moderate thickness.

Using the data obtained from Airfoil Tools [18], the airfoil was generated in Salome Meca and it was extruded to a span of 2.4 chord lengths, ensuring a slender blade geometry. With this configuration, the aim is to perform a CFD simulation and as an output, the pressure distribution at the interface is extracted. Using it, the loads are generated and afterwards, they are introduced in the topology optimization in order to obtain stresses that are higher

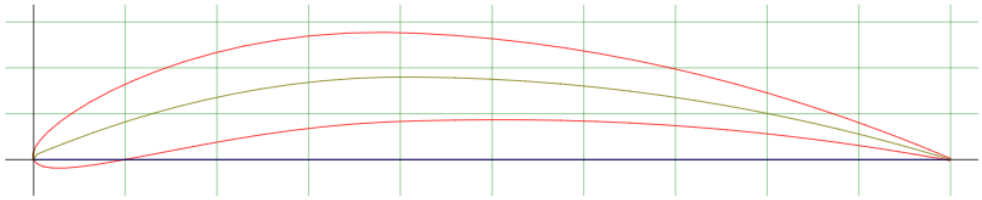


Figure 3.1: NACA 9410 airfoil. Adapted from Airfoil Tools [18].

than the material allowable values. Therefore, this slender blade configuration presented in fig. 3.2 aligns with the main characteristics of a more complex distortion grid system.

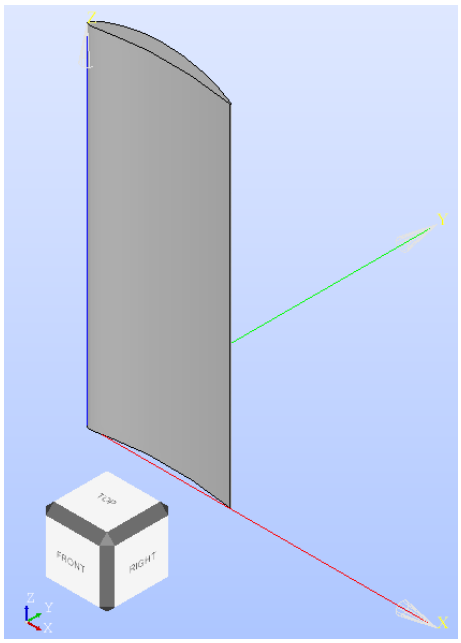


Figure 3.2: Geometry of the extruded blade based on the NACA 9410 airfoil in XY-plane and extruded 2.4 chord lengths along the Z-axis

3.3 Geometry mechanical status

The chosen geometry is presented in this section, along with the mechanical characteristics of the blade. A modal analysis is conducted in order to determine the dynamic behavior of the reference blade. The output is represented by the natural frequencies which describe the frequencies at which the structure naturally tends to vibrate, along with the corresponding mode shapes, emphasizing the deformation patterns for each vibration mode.

Generally, a modal analysis solves the generalized eigenvalue problem [19]:

$$(\mathbf{K} - \omega^2 \mathbf{M})x = 0, \tag{3.1}$$

where $\mathbf{K}$ and $\mathbf{M}$ represent the stiffness and mass matrix respectively, ω is the circular frequency and x is the corresponding mode shape of the structure. For non-trivial solutions $x \neq 0$, the corresponding determinant vanishes [19]:

$$det(\mathbf{K} - \omega^2 \mathbf{M}) = 0 \tag{3.2}$$

and in this way, the eigenvalue $\lambda = \omega^2$ is obtained. Furthermore, the natural frequency is found using [19]:

$$f = \frac{\sqrt{\lambda}}{2\pi} = \frac{\omega}{2\pi}. \tag{3.3}$$

The material used for this simplified case is the *rigid 10k* resin plastic with a UV post-processing, having the properties presented in tab. 3.1.

Table 3.1: Material properties

Material properties	
Density	$\rho = 1700\ [kg/m^3]$
Poisson's ratio	$\nu = 0.425\ [-]$
Young's modulus	$E = 10\ [GPa]$

The blade mesh was created using the open source software, Salome Meca, using the NETGEN 1D-2D-3D algorithm. The domain was discretized using an unstructured first-order tetrahedral mesh, consisting of 24,870 nodes and 103,178 tetrahedral volume elements. For the boundary conditions, the bottom surface of the blade was clamped, while the rest of the structure was left unconstrained.

The first six natural frequencies along with their corresponding mode shapes were computed using Morfeo (Manufacturing Oriented Finite Element Tool), a software developed at Cenaero to simulate welding, machining, crack propagation predictions and optimizations. The mode shapes were visualized using the ParaViS module integrated inside Salome platform, using the same scaling factor. The mode shapes are presented in fig. 3.3 and the corresponding values are presented in tab. 3.2. As expected, the values are increasing with the mode number, indicating more complex deformation patterns.

The first mode shape is characterized by a first bending of the structure. As the blade is clamped at the bottom, the displacement magnitude increases from the root towards the tip, where the maximum displacement is observed. The second mode represents the first torsional mode, where the blade is twisted around its longitudinal axis, while the third one corresponds to the second bending mode. This mode displays a change in curvature along the span and consequently, it presents a more complex deformation pattern than the first bending mode of the structure.

The following three modes present similar deformation pattern that were observed for mode 1, 2 and 3, but at higher frequencies. The higher-order bending modes (4, 6) are more complex, with increased curvatures and local deformations, while the second torsion mode (mode 5) displays a more pronounced deformation pattern.

Hence, all six modes were presented, but in the topology optimization process, only the first three will be taken into account, since these mode shapes present the dominant deformation patterns of the structure (mainly bending and torsion).

Table 3.2: First six natural frequencies

Mode	Frequency [Hz]
f_1	10.31
f_2	45.02
f_3	61.44
f_4	66.51
f_5	138.75
f_6	161.23

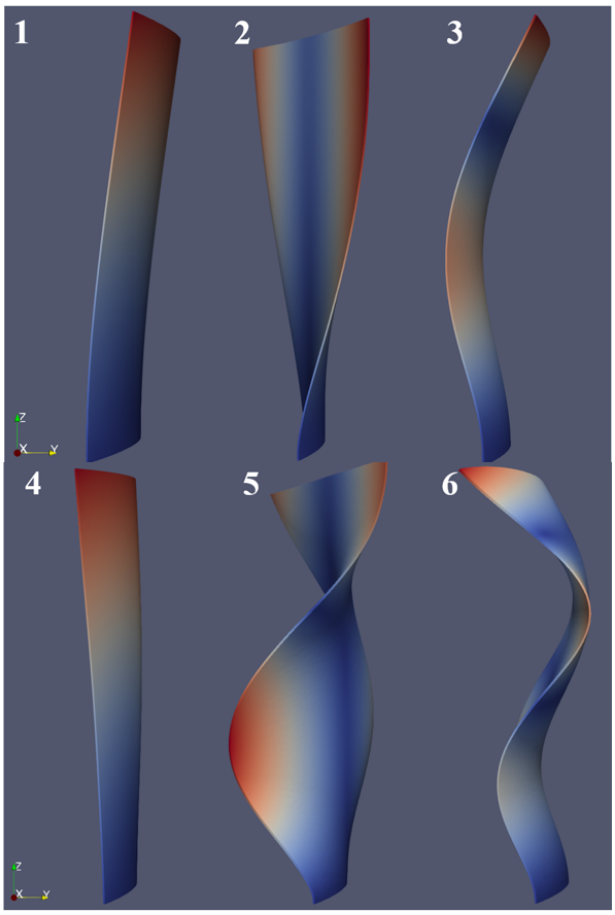


Figure 3.3: First six mode shapes of the blade

3.4 CFD simulation

After analyzing the dynamic behavior of the structure, the following step consists of obtaining a realistic representation of the loads during operation and for this purpose, a Computational Fluid Dynamics (CFD) simulation was performed. The objective of this simulation is to determine the pressure distribution on the blade surface under prescribed operating conditions. Subsequently, the obtain pressure is translated into mechanical loads and it is introduced in the optimization.

3.4.1 Computational domain

The CFD simulation was performed on the three-dimensional test case, obtained from the NACA 9410 airfoil that was extruded in $z-$ direction. This extrusion serves as a simplification in the aerodynamic analysis, preserving a constant cross-section area and facilitating the meshing process.

The blade was placed in a large domain, simulating the surrounding air around the blade placed in an aerodynamic tunnel. The fluid domain was constructed relative to blade chord length c. An upstream distance of $0.5 \cdot c$ and a downstream distance of $2 \cdot c$ were defined, while a clearance of $0.5 \cdot c$ was maintained between the blade and the top wall. Therefore, the corresponding domain is presented in the figs. 3.4, 3.5.

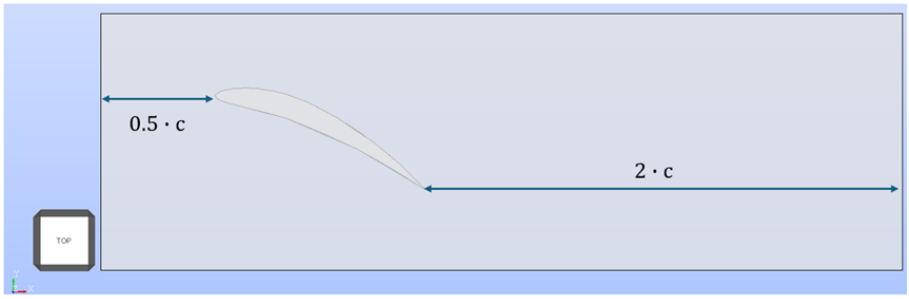


Figure 3.4: Fluid domain - top view

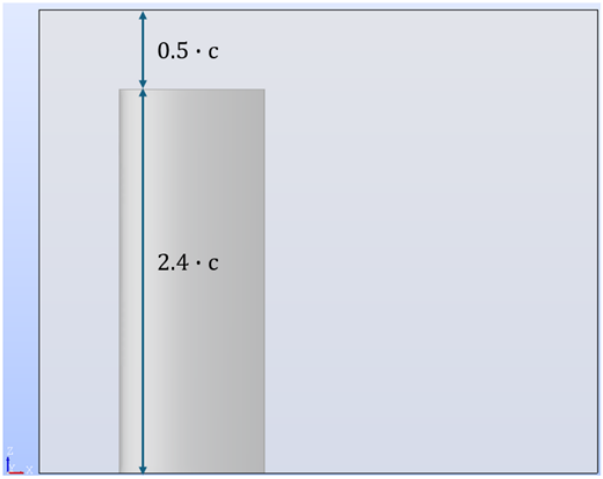


Figure 3.5: Fluid domain - side view

The blade was rotated with $\theta = 24°$, such that the incoming flow is aligned with the local camber line. This angle was obtained using the NACA four-digit camber equation:

$$\frac{dy_c}{dx} = \frac{2M}{P^2}(P - x), \qquad 0 \leq x \leq P \tag{3.4}$$

with M being the maximum camber with its corresponding location P [18]. Using $x = 0$ for the leading edge, the slope becomes [18]:

$$\frac{dy_c}{dx} = 0.45, \tag{3.5}$$

while the corresponding inclination angle θ is found using [18]:

$$\theta = tan^{-1}(\frac{dy_c}{dx}) \approx 24.2°. \tag{3.6}$$

3.4.2 Meshing process

Following the computational domain definition, the next step is represented by the mesh generation. To improve the flow field resolution in regions where large pressure gradients are expected, boundary layers are added. A boundary layer is considered around the blade and since the four walls of the domain are modeled as no-slip walls, a boundary layer for this region was also added.

In order to determine the boundary layer parameters, the Reynolds number was computed in both cases:

$$Re = \frac{\rho U L}{\mu}, \tag{3.7}$$

with $\rho = 1.225\,m/s$ being the density of the standard air, U the freestream velocity, L the characteristic length and $\mu = 1.8 \cdot 10^{-5} Pa \cdot s$ the dynamic viscosity. The freestream velocity is chosen $u = 200\,m/s$ to match the case with the industry application.

Following this, the height of the first prism layer was determined, in order to ensure an appropriate mesh resolution, using the target dimensionless wall distance y^+:

$$y_1 = \frac{y^+ \mu}{\rho u_\tau}, \tag{3.8}$$

where the friction velocity is computed as:

$$u_\tau = \sqrt{\frac{\frac{1}{2} C_f \rho U^2}{\rho}}. \tag{3.9}$$

In this case, the target dimensionless wall distance was chosen $y^+ = 4$ such that the first computational cell is placed within the viscous sub-layer, ensuring a convenient resolution, while avoiding an increase in computational cost.

The boundary layers contains n prism layers with a growth rate $g = 1.2$ and the total thickness is computed using:

$$\delta = y_1 \cdot \frac{g^n - 1}{g - 1}, \tag{3.10}$$

ensuring convenient transition between the highly refined region around blade or walls and the coarser tetrahedral mesh inside the domain.

Consequently, following this process, around the blade, $n = 19$ layers were used, while the total thickness of the boundary layer is equal to 0.96 mm and the first cell thickness is approximately 6.2×10^{-3} mm. For the walls boundary layer, $n = 23$ layers were used, with a total thickness of 2.2 mm and a first cell thickness of 6.2×10^{-3} mm. The obtained mesh is presented in fig. 3.6 and has 12.6 millions of elements and 5.2 millions of nodes.

3.4.3 Model setup

The CFD simulation was conducted using the SU2 software. The chosen solver is the Reynolds-Averaged Navier-Stokes (RANS) in which the flow is assumed to be time dependent, with a solution that converges to a steady state. The turbulence model is described using Sapalart-Allmarad (SA) and the operating conditions of the flow are defined using the free-stream conditions:

- Mach number $M = 0.576$,
- free-stream pressure $p_s = 101325 Pa$,
- free-stream temperature $T = 300K$.

The flow is modeled as standard air with $\gamma = 1.4$ and gas constant R equal to 287.058 $J/(kg \cdot K)$, while the dynamic viscosity is computed using the Sutherland's law.

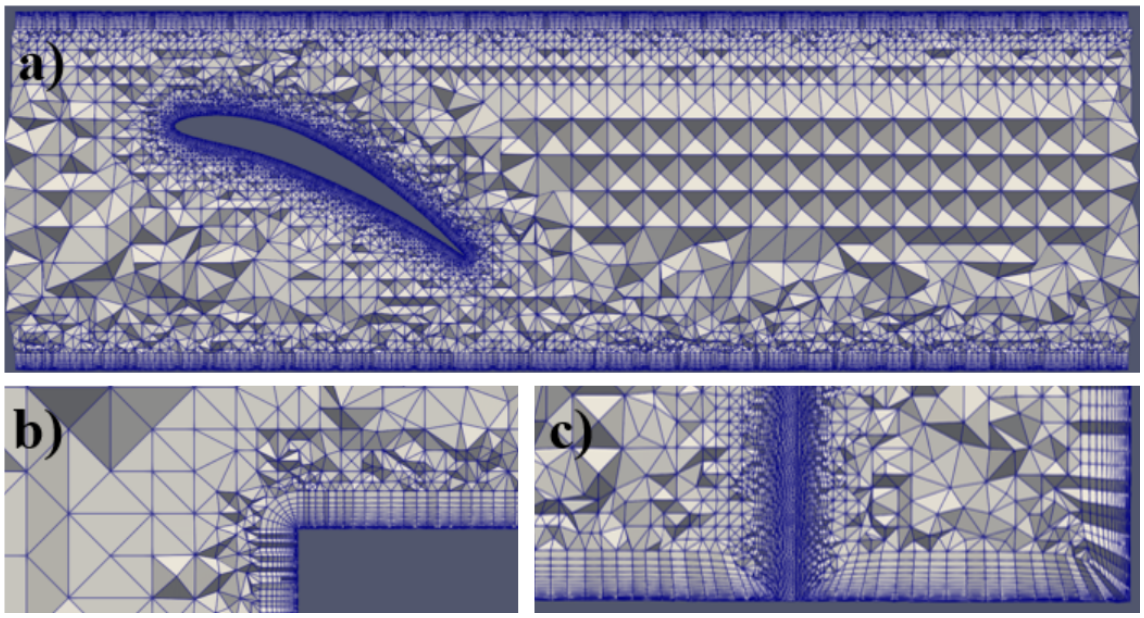


Figure 3.6: Cross-sectional views of the mesh used in CFD simulation: a) slice in the xy plane emphasizing the boundary layers of the blade and walls walls, b) slice in xz plane emphasizing the blade boundary layer, c) slice in yz plane emphasizing the walls boundary layer

In terms of boundary conditions, for the inlet, a mass flow boundary condition is defined, using the air density $\rho = 1.1766\ kg/m^3$ and an inlet velocity of 200 m/s, while for the outlet, the pressure is fixed at 101325 Pa. The blade surface is modeled using the adiabatic wall condition, while the outer walls are treated as no-slip walls.

A residual convergence criterion was imposed to 10^{-12} and quantities such as pressure, velocity, Mach number were extracted and visualized using ParaViS.

3.4.4 Results and discussions

A first solution from this CFD simulation presented a non-physical result for the prescribed operating conditions. The prescribed Mach number at the inlet is equal to 0.576, while during the computation, a Mach number approaching $M = 2$ was identified, as it can be observed in fig. 3.7.

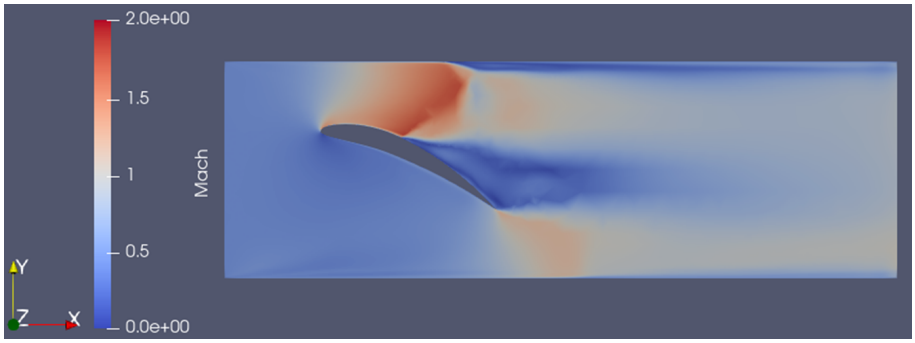


Figure 3.7: Mach number distribution in the computational domain for the prescribed $M_{inlet} = 0.576$

The cause of this non-physical result can be represented by a blockage due to the computational domain dimensions. The blade occupies part of the cross-sectional area in the fluid domain, while the upper and lower corresponding part are 0.5 chord lengths, resulting in a narrow flow passage. Therefore, the flow is forced to pass through a restricted zone around the blade, resulting in an artificial increase in terms of Mach number. Furthermore, having these non-realistic values for the velocity, the pressure distribution was highly influenced and consequently, the obtained values cannot be used in the optimization computation.

A rapid solution for this problem, without needing to modify the domain dimensions is to reduce the inlet Mach number. The value of the imposed Mach number was progressively reduced until the flow remained subsonic ($M < 1$) in the computational domain. As a result, a prescribed inlet Mach number equal to $M = 0.23$ was imposed and the obtained results are presented in fig. 3.8.

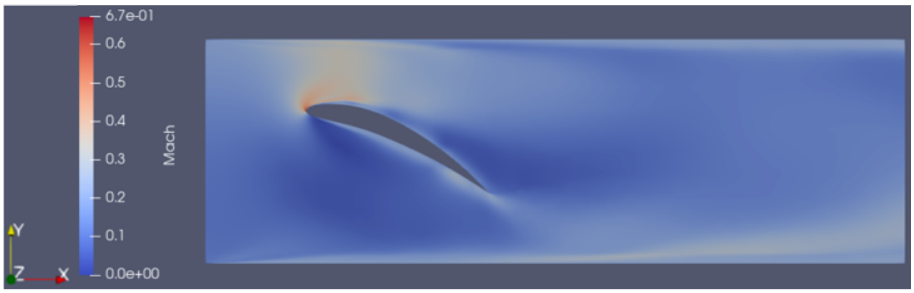


Figure 3.8: Mach number distribution in the computational domain for the prescribed $M_{inlet} = 0.23$

The corresponding convergence history is presented in fig. 3.9, displaying the residuals evolution after the 2000 iterations. In the initial iterations, the residuals decrease and small oscillations can be seen. Although this behavior is observed, the oscillations remain bounded and therefore, the solution was considered valid for the pressure extraction. The continuity residual $rms[\rho]$ decreases to approximately 10^{-7}. Additionally, the energy residual $rms[E]$ stabilizes at around 10^{-2}, while the other residuals remain around 10^{-5}.

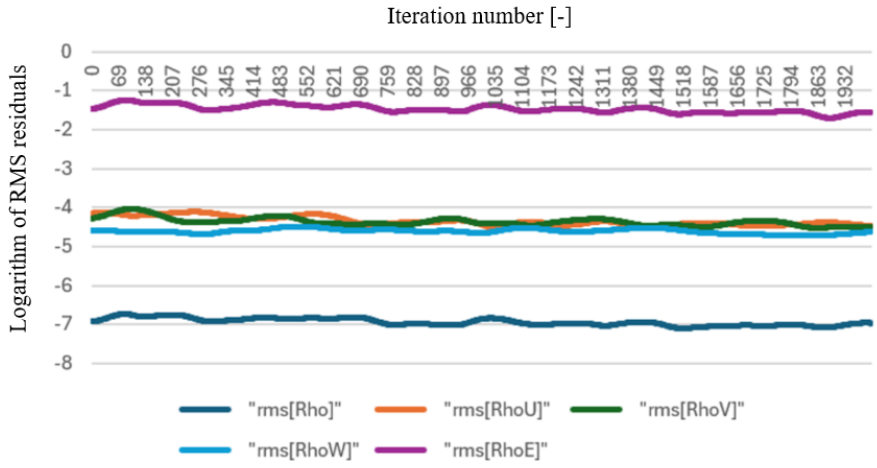


Figure 3.9: Convergence history of the CFD simulation with a prescribed $M_{inlet} = 0.23$

The pressure distribution was extracted at blade interface as it is shown in fig. 3.10. A non-uniform distribution is obtained and for the lower part of the blade, higher pressure levels are observed at around $1.3 \times 10^5\, Pa$. Therefore, this part is subjected to a larger aerodynamic load, while the upper part presents lower and intermediate pressure levels, varying between $6.2 \times 10^{-4}\, Pa$ and $1.1 \times 10^5\, Pa$.

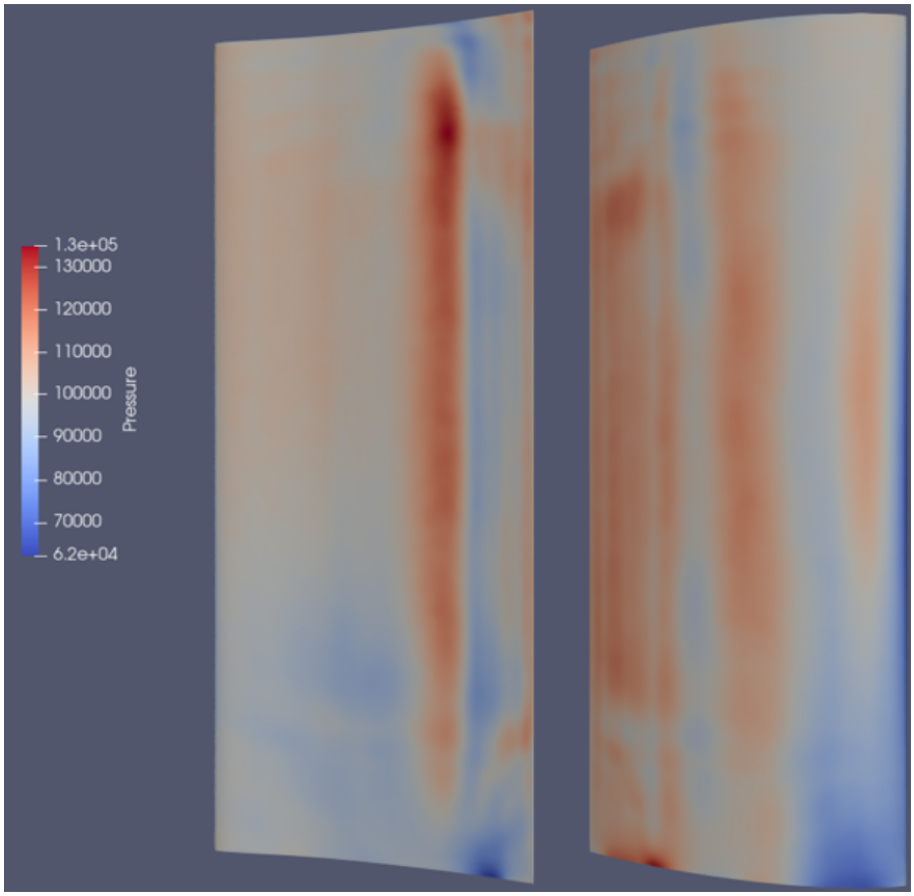


Figure 3.10: Extracted pressure distribution at blade interface obtained from the CFD simulation with prescribed $M_{inlet} = 0.23$

The objective of the CFD analysis was to determine the pressure distribution at the interface. Using it, the mechanical constraints can be derived from it and introduced in the topology optimization. This process is detailed in the following chapter.

Chapter 4

Topology optimization applied to two-dimensional model

In this chapter, different $2D$ topology optimization cases based on the simplified test case defined in chapter 3 are presented. Considering a $2D$ case first facilitates the validation of the optimization framework and allows to evaluate the optimization strategy while maintaining a low computational cost. Following this chapter, the procedure is directly transferred in $3D$ cases, ensuring the applicability of the proposed approach under more realistic conditions.

4.1 Model definition

The two-dimensional model corresponds to a $2D$ mid-span cut of the full three-dimensional model defined in the chapter 3, as it can be observed in fig. 4.1. Due to the fact that distortion grids are tested in wind tunnels, a restricted domain is created around the blade, representing the optimizable domain, which is smaller than the CFD domain in order to reduce the computational cost. Because the geometry definition starts from the wind tunnel configuration, the two parallel walls were clamped, whereas the inlet and outlet boundaries remained unconstrained. These clamped regions are highlighted in red in fig. 4.1.

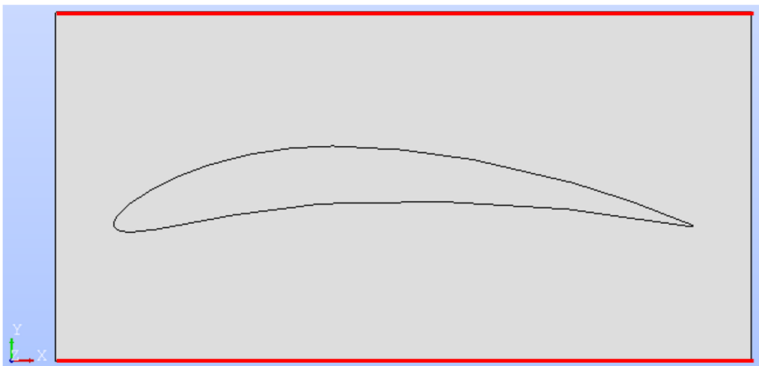


Figure 4.1: Two-dimensional topology optimization configuration - NACA 9410 airfoil with its corresponding surrounded domain

The primary objective of the presented optimization is to increase blade's rigidity by creating several supports around the blade and based on this, the topology optimization problem is formulated.

The *rigid 10k* resin plastic with a UV post-processing is used in the following optimizations and the mesh used is presented in fig. 4.2. The geometry was discretized into a finite element mesh that consists of $8,284$ nodes and $16,206$ linear triangular elements.

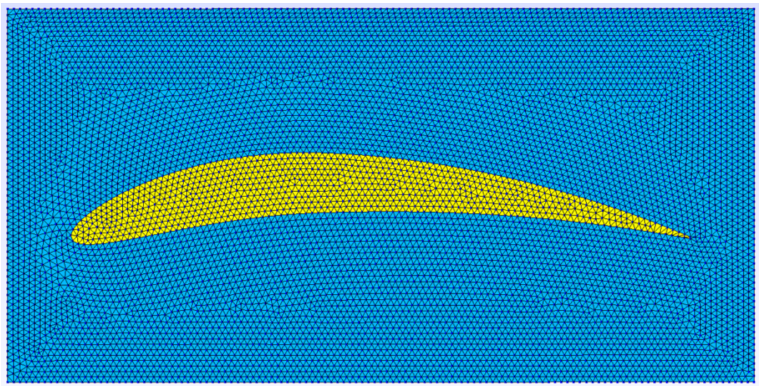


Figure 4.2: Finite element mesh of the $2D$ topology optimization configuration

4.1.1 Loading conditions

Based on the pressure distribution obtained from the CFD simulation, two loading cases are defined. The first one represents a simplification used in the initial computations, while the second option corresponds to a more accurate representation of the pressure field. Each loading case is used in a separate topology optimization and the results are compared afterwards.

4.1.1.1 Case A - Simplified loading

In this first case, a distributed force is extracted and the obtained values are used. Using the CFD solution described in section 3.4.4, the aerodynamic pressure field is extracted using ParaViS, meaning that for each node on the CFD mesh, the values for pressure and their corresponding normals are extracted. As a result, for each node, a pressure value with its corresponding normal vector were obtained:

$$\mathbf{x}_i \rightarrow \{p_i, \mathbf{n}_i\}, \qquad \mathbf{n}_i = \begin{bmatrix} n_{x,i} \\ n_{y,i} \\ n_{z,i} \end{bmatrix}, \qquad \|\mathbf{n}_i\| = 1, \tag{4.1}$$

where $\mathbf{x}_i$ represents a surface node, p_i is the pressure and $\mathbf{n}_i$ represents the normal vector.

Using these data, the first step consists of extracting the corresponding force. Since the CFD result displayed the absolute values, the atmospheric pressure is extracted in order to obtain the gauge pressure acting on the blade structure. Therefore, the force is obtained using:

$$\mathbf{F} = -(\mathbf{p} - p_{atm}) \cdot \mathbf{n}, \tag{4.2}$$

where $p_{atm} = 101325\, Pa$.

The negative sign ensures that the loads is acting towards the surface and for the three axes, the loads are presented in tab. 4.1.

Table 4.1: Obtained force components for the three axes

Force	Value
$\mathbf{F_x}[\mathbf{N}]$	-4.516
$\mathbf{F_y}[\mathbf{N}]$	-2.184
$\mathbf{F_z}[\mathbf{N}]$	0.194

The computed values were divided by the total area of the blade ($A = 0.00314\ m^2$) and the corresponding distributed forces are given in tab. 4.2.

Table 4.2: Distributed force for the three axes

Distributed force	Value
$\mathbf{Q_x}[\mathbf{N}]$	-1438.37
$\mathbf{Q_y}[\mathbf{N}]$	-695.78
$\mathbf{Q_z}[\mathbf{N}]$	61.93

Hence, the uniformly distributed force is applied on the airfoil contour in the $2D$ configuration and the stresses are evaluated. This simplification serves as a baseline representation of the actual load, useful for investigating the influence of the optimization parameters under simplified loading conditions.

4.1.1.2 Case B - Aerodynamic loading

This case defines a detailed representation of the pressure distribution, linking the loads obtained on the CFD mesh to a more coarser mesh used in mechanical contexts. The objective of this procedure is to apply a load on each edge of the finite element mesh that construct the airfoil, resulting in a more detailed representation of the CFD result.

Using ParaViS, the pressure for each node is extracted, along with their coordinates and in the following steps, these quantities are projected on a coarser mesh that can be used during the optimization.

Therefore, for each edge extracted from the structural mesh, the midpoint x_m is computed, representing the sampling point used in the projection:

$$x_m = \frac{x_1 + x_2}{2}, \tag{4.3}$$

where x_1 and x_2 represent the edge coordinates.

The normal is computed from the tangent vector using:

$$\mathbf{t} = \begin{bmatrix} t_x \\ t_y \end{bmatrix} = \frac{x_2 - x_1}{||x_2 - x_1||}, \quad \mathbf{n} = \begin{bmatrix} t_y \\ -t_x \end{bmatrix} \quad or \quad \mathbf{n} = \begin{bmatrix} -t_y \\ t_x \end{bmatrix}, \tag{4.4}$$

depending on contour orientation and ensuring that all normals are pointing outward the blade contour.

The next step is to transfer the CFD pressure to the structural mesh. The extracted airfoil contour has 651 edges, while the mechanical mesh has 207. To be efficient while assigning the pressure, for each structural edge, the closest CFD point is computed using:

$$j = \arg\min_i \left\| \mathbf{x}_m - \mathbf{x}_i^{\text{CFD}} \right\|, \tag{4.5}$$

where x_i^{CFD} is the CFD point, while x_m is the midpoint.

Thus, using this procedure, the pressure is assigned:

$$p_{edge} = p_j, \tag{4.6}$$

where j is the closest CFD point to the midpoint of a structural edge.

Once the two constituents are determined, the loads can be written using:

$$q_x = p \cdot n_x, \quad q_y = p \cdot n_y. \tag{4.7}$$

This approach ensures an accurate representation of the loads, derived from the CFD simulation, ensuring a realistic context in which the presented methodology can be validated.

In order to validate this method, the pressure distributions are plotted with respect to the distance from the leading edge in fig. 4.3. The airfoil is divided into two contours corresponding to the lower and upper part. The continuous lines represent the pressure extracted using ParaViS, while the dashed lines correspond to the projection results. The pressure distribution extracted mid-span presents a maximum value of approximately $12,500\,Pa$ on the lower surface, while a minimum of approximately $90,000\,Pa$ is present on both contours.

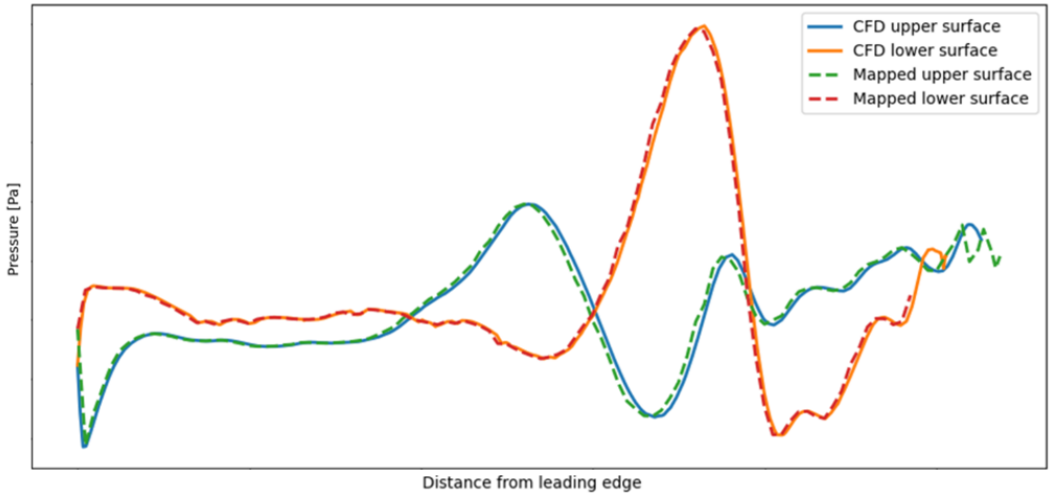


Figure 4.3: Comparison of the CFD and mapped pressure distributions on the extracted $2D$ section

The analysis displays a good agreement between the two distributions, preserving the main characteristics such as maximum and minimum values or recovery towards the trailing edge. Small differences are observed, indicating that small deviations of approximately $1-2\%$ are introduced during the mapping procedure, while oscillations are seen near the trailing edge. These effects are expected due to the fact that the structural mesh (207 edges) is coarser than the one used in CFD (561 edges) and despite the small differences between the two cases, the overall trends display a good correspondence.

After validating the procedure, the mechanical loads are obtained and can be introduced in the optimization. Therefore, 414 loads were obtained, indicating that, for each edge, a force is applied on $x-$ and one on $y-$axis.

In the following section, multiple $2D$ optimization cases are presented, showing a process that was conduced progressively in order to analyze the influence of each aspect, while ensuring that the whole process remains stable and the results are valid.

4.2 Eigenfrequency maximization with a volume constraint

In the current section, a first topology optimization is presented, where the first three eigenfrequencies are maximized, while a fraction of the total volume is retained.

4.2.1 Problem definition

The objective of the current case is to create a baseline optimization that can be progressively refined, facilitating parameters isolation, process verification and progressive improvements that can be directly applied in the $3D$ case in the next chapter. Since the computational cost is severely reduced in the $2D$ case, the transfer of methods and parameters is supported, ensuring a continuous and efficient process.

The finite element model adopted for the $2D$ optimization case is illustrated in fig. 4.4. As it was presented before, a rectangular domain is created and inside of it, a NACA 9419 airfoil is placed. The full domain is denoted as Ω, composed of two subdomains Ω_d and Ω_{nd} such that $\Omega = \Omega_d \cup \Omega_{nd}$. The design domain is therefore denoted as Ω_d, representing the area around the blade where the optimizer is expected to create structures that can attach the blades to the domain boundaries. The non-optimizable domain is considered the blade area, denoted Ω_{nd} that is preserved during the optimization. The boundary conditions are presented as Γ_{fix}, representing the clamped regions of the design domain. For the boundary conditions, the two parallel rectangle sides are clamped:

$$\mathbf{u} = \mathbf{0} \quad on \quad \Gamma_{fix}, \tag{4.8}$$

replicating in $2D$ a blade placed inside a wind tunnel, while the other two sides are unconstrained.

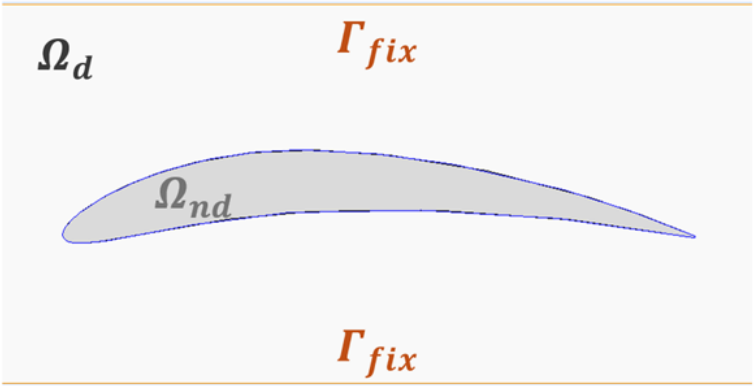


Figure 4.4: Design domain and boundary conditions for the $2D$ topology optimization problem - case 1

The objective of the optimization is increase the mechanical resistance by creating rigid supports that connect the blade to the surrounding domain sides in order to increase structural stiffness and reduce deformations. Therefore, this initial optimization case focuses on maximizing the eigenfrequencies, while maintaining a relatively low mass. In particular, these characteristics are related such that:

$$f_n \propto \sqrt{\frac{k}{m}}, \tag{4.9}$$

where k represents the stiffness and m the mass. Consequently, in an optimization with an imposed volume fraction, the mass is fixed or limited, while the optimizer needs to redistribute material in order to increase the structure's stiffness, facilitating more efficient load paths and higher natural frequencies. Additionally, using eigenfrequencies maximization in the present formulation offers a preliminary assessment for the flutter, shifting the natural frequencies away from the excitation.

The Method of Moving Asymptotes (MMA) is used in the optimizations, a gradient based algorithm that approximates the non-linear problem with a convex one using moving asymptotes [20]. Along with it, a density based approach is used in the following cases, offering a robust framework that is suited for gradient based optimization. Therefore, for each element, an initial density is set and during the optimization process, these densities are continuously updated in order to meet the objective, while still taking into account the constraints. This approach can also introduce intermediate densities or gray regions and therefore, a SIMP (Solid Isotropic Material with Penalization) material interpolation method is introduced. Using this, the design variables ρ are directly related to material properties of the finite elements [20]:

$$E(\rho) = E_{min} + \rho^p(E_0 - E_{min}), \tag{4.10}$$

where E_0 is the Young's modulus of the material, $E(\rho)$ is the interpolated Young's modulus, E_{min} is the minimum stiffness assigned to void elements and p represents the penalization factor that is used to reduce the intermediate densities. Hence, for the following optimizations, a penalization factor $p = 3$ is adopted, while the minimum Young's modulus is set to $E_{min} = 10^{-6}$.

Using the presented framework, the blade represents the non-optimizable domain and therefore, the assigned initial density field corresponds to $\rho = 1$ in order to represent a solid zone that remains unmodified during the optimization process. For the optimizable domain, the surrounding area around the blade is considered, facilitating the supports and ribs creation. For this zone, an initial density field $\rho = 0$ is imposed, illustrating the void around the airfoil and facilitating the material addition.

The optimization objective is to maximize the first three eigenfrequencies, while a volume constraint is imposed such that the optimize is allowed to keep only 10% of the optimizable domain material. The current optimization problem can be written as:

$$\begin{aligned} \max_{\boldsymbol{\rho}} \quad & \left(\sum_{i=0}^{n=2} \frac{1}{\lambda_i(\boldsymbol{\rho})} \right)^{-1} \\ \text{s.t.} \quad & \frac{V(\boldsymbol{\rho})}{V_0} \leq 0.10, \\ & 0 \leq \rho \leq 1, \end{aligned} \tag{4.11}$$

where ρ represents the design variables with values between 0 (void) and 1 (solid), $\lambda_i(\rho)$ represents the eigenvalues, $V(\rho)$ is the material volume in the optimized design space and V_0 represents the volume of the optimized domain before optimization.

The topology optimizations were performed using Morfeo. In order to have a control on the final design, a density filter was imposed. The local lengths of the elements in the presented mesh are around $0.15 - 0.25\,mm$ and a filter radius of $0.50\,mm$ was chosen, ensuring that the final design won't contain small features that are non-physical. Another factors that are strongly influencing the geometry evolution are the scaling parameters. Because different functions can have values with different orders of magnitude, the scaling is applied in order to improve the numerical conditioning, avoiding excessive influence of certain functions on the final design. In the current case, the default values were used, meaning that the objective and constraint weights were set to 1.

4.2.2 Results and discussion

For this first topology optimization, the result obtained after 100 iterations is presented in fig. 4.5. The geometry obtained using Morfeo was visualized afterwards using an open source software, Gmsh. Therefore, in this density representation, the solid regions where $\rho \approx 1$ correspond to retained material, while the low densities regions $\rho \approx 0$ indicate the zones where the material was removed.

As expected, in regions with low structural contribution, the material densities are 0 or almost 0 (blue regions). In high structural contribution zones, a network of ribs was created (red areas), connecting the airfoil to the surrounding domain boundaries and increasing the structural stiffness. The inclined supports indicate a dominant stress region between the blade and the fixed edges, while the transverse ribs offer additional stiffness by reducing the local bending that may be experienced and improving the local load distribution. Their geometry is highly influenced by the imposed filter radius, resulting in multiple supports with a minimum characteristic thickness, avoiding formation of thin non-physical structures. Additionally, the intermediate densities are reduced, indicating that the SIMP penalization was successfully implemented. The airfoil is presented in red, illustrating a domain where the densities are equal to 1 and as imposed, the zone was not modified during the process.

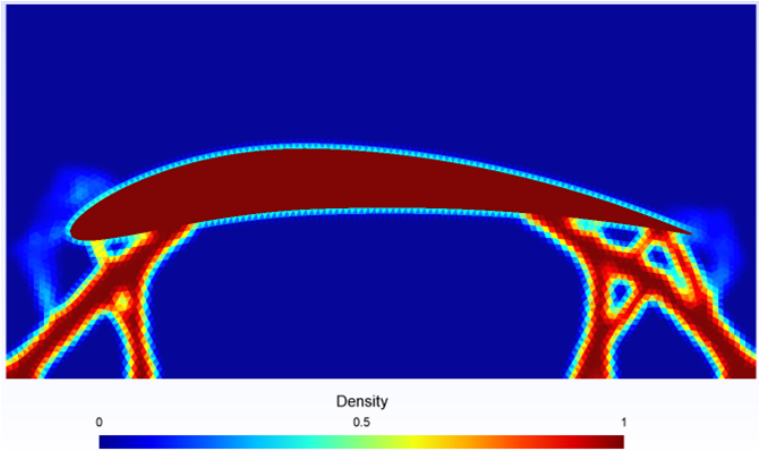


Figure 4.5: $2D$ density based topology optimization result (objective: maximize the first three eigenfrequencies, constraint: retain 10 % of the initial volume)

In order to evaluate the optimization process evolution, the objective function along with the imposed constraint evolutions were plotted with respect to the iterations in figs. 4.6 and 4.7. The scaled objective function presents a stable behavior. The decreasing trend indicates a progressive minimization of the objective and therefore, an improvement in terms of eigenfrequencies is obtained. In the first iterations (between $1 - 7$), the value of the function is almost constant, while a rapid improvement is observed in the following iterations. This indicates that the optimizer is able to identify an efficient material distribution that can satisfy the problem. A sudden increase is observed at iteration 20, indicating the fact that the optimizer is adjusting in order to maximize the eigenfrequencies, while satisfying the volume constraint. Afterwards, the objective function decreases progressively and small changes are observed in the last iterations.

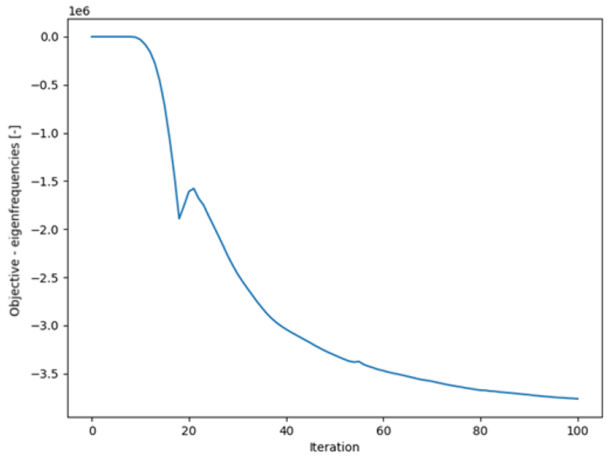


Figure 4.6: $2D$ density based optimization - maximizing eigenfrequencies objective evolution with respect to the iterations - case 1

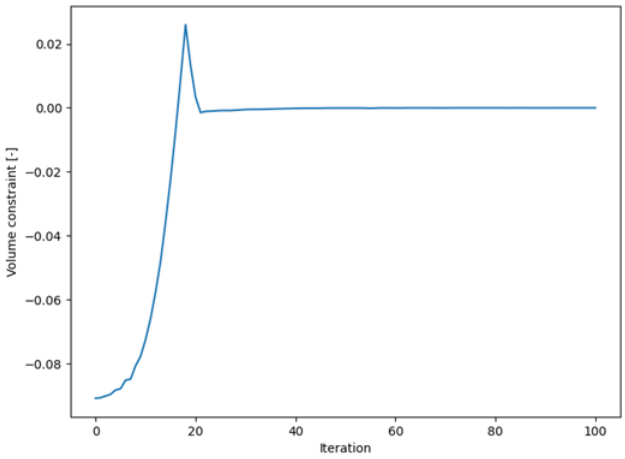


Figure 4.7: $2D$ density based optimization - volume constraint evolution with respect to the iterations - case 1

For the volume constraint, a similar behavior is observed. The constraint is constantly changing at the beginning of the optimization, while at iteration 20, the sudden increase is visible. The optimizer stabilizes quickly and the 10 % volume constraint is clearly satisfied afterwards.

Another important aspect in this analysis is the natural frequencies evolution. Their corresponding evolution is presented in fig. 4.8, along with the obtained values in tab. 4.3.

Using Morfeo, the obtained natural frequencies in rad/s are extracted every 10 iterations. The three natural frequencies present stable increase with respect to the iterations, starting from 20, 46 and 60 rad/s and increasing until they reach $2,800\,rad/s$, $3,000\,rad/s$ and respectively $5,800\,rad/s$. The results stabilize after 40 iterations for the first two frequencies, while the third one continues to increase progressively.

Overall, the trends emphasize that the objective is achieved, while the volume constraint is satisfied. The three eigenfrequencies are maximized until they reached a plateau, resulting in a geometry where the airfoil is connected to the boundary edges through a ribs system. In the following optimizations, the loads are introduced and their influence is analyzed with respect to this first result.

	$f_1[rad/s]$	$f_2[rad/s]$	$f_3[rad/s]$
Iter. 0	20.1	45.7	59.9
Iter. 100	2,849.3	2,973.7	5,813.7

Table 4.3: Natural frequencies - case 1

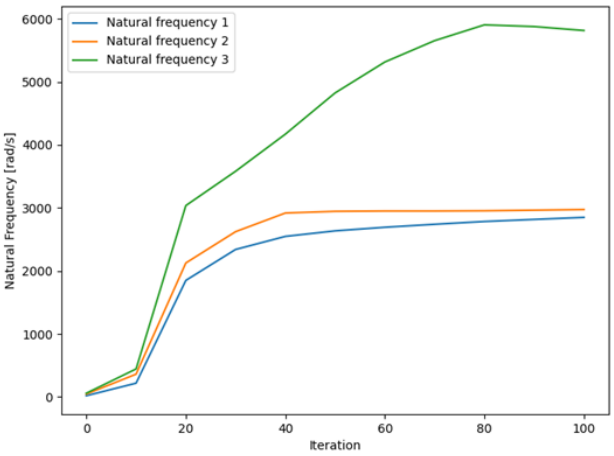


Figure 4.8: $2D$ density based optimization - first three natural frequencies evolution with respect to the iterations - case 1

4.3 Eigenfrequency maximization under a distributed load with volume and stress constraints

The previous optimization problem considered only the eigenfrequencies optimization under a volume constraint. This approach was a simplified case, serving as a baseline result, while the structural integrity of the structure was not controlled. Subsequently, an additional stress constraint is introduced in order to ensure that the final design satisfies the mechanical and dynamic performances.

4.3.1 Problem definition

The eigenfrequencies maximization remains set as an objective, while a 10 % volume constraint is imposed. Furthermore, a stress constraint is added in order to have a better control on the design evolution by imposing a maximum allowable limit. Therefore, the optimization is now based on a modal and a linear static analysis. The modal analysis is used to evaluate the objective function, while the linear elastic problem provides the stress field that is required to satisfy the stress constraints.

The finite element model is identical to the previous case as well as the fixation boundary condition. Additionally, the distributed load obtained from the CFD result and described in section 4.1.1.1 is prescribed on the airfoil contour.

The design domain is identical to the one described in section 4.2.1, with the airfoil prescribed as non-optimizable domain and surrounding area as optimizable domain. However, with the introduction of linear elastic analysis, a new boundary condition is needed, where the distributed load can be applied. The new boundary condition is presented in fig. 4.1 and it is written as Γ_p which represents the airfoil contour. Therefore, the updated boundary conditions are written:

$$\begin{aligned} \mathbf{t} &= \begin{bmatrix} q_x \\ q_y \end{bmatrix} = \begin{bmatrix} -1438.37 \\ -695.78 \end{bmatrix} [Pa] \quad \text{on} \quad \mathbf{\Gamma_p}, \\ \mathbf{u} &= 0 \quad \text{on} \quad \mathbf{\Gamma_{fix}}, \end{aligned} \tag{4.12}$$

where $\mathbf{u}$ represents the displacement and $\mathbf{q_x}$, $\mathbf{q_y}$ are the distributed forces.

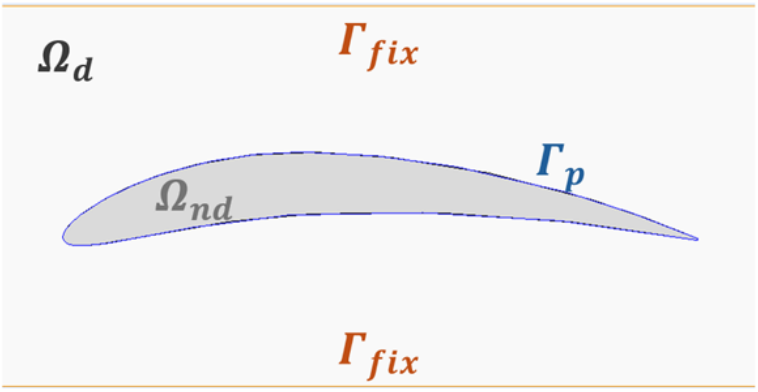


Figure 4.9: Design domain and boundary conditions for the $2D$ topology optimization problem - case 2

The distributed load presented in section 4.1.1.1 was extracted from the blade pressure distribution and therefore it is representative for the $3D$ optimization cases. To maintain consistency between the $2D$ and the $3D$ case, the same loads are applied, serving as a validation model by applying a representative aerodynamic loading to the airfoil contour. During the process, the stresses are evaluated and the geometry is continuously updated while ensuring that the stresses remain under a prescribed value. For the chosen material, *rigid 10k* resin plastic with a UV post-processing, the ultimate tensile strength is equal to $65\,MPa$. A safety factor equal to 2 is considered and as a result, a maximum allowable stress equal to $32.5\,MPa$ is considered in this optimization case.

Therefore, with the explained modifications, the updated optimization case can be written as:

$$\begin{aligned} \max_{\boldsymbol{\rho}} \quad & \left(\sum_{i=0}^{n=2} \frac{1}{\lambda_i(\boldsymbol{\rho})} \right)^{-1} \\ \text{s.t.} \quad & \frac{V(\boldsymbol{\rho})}{V_0} \leq 0.10, \\ & \frac{\sigma_{max}(\boldsymbol{\rho})}{\sigma_{allowable}} \leq 1, \\ & 0 \leq \rho \leq 1, \end{aligned} \tag{4.13}$$

where $\sigma_{max}(\rho)$ represents the maximum von Mises stress and $\sigma_{allowable} = 32.5\,MPa$ is the prescribed stress limit.

In a multi-constraint optimization, the scaling factors represent a more sensitive aspect than in the previous case with only one volume constraint. Because the stress constraint modifies the optimization behavior, several combinations of scaling factors were tested in order to find a balanced design. In the $2D$ cases, the computational cost is low and therefore, the sensitivity study was facilitated.

In the previous case, the default parameters (1 for both objective and constraint) were used, while in the current case, the objective function, volume and stress constraints exhibit different orders of magnitude. When the scaling is not properly chosen, one term can dominate the final design, obtaining a poor convergence and a non-physical final result. With a proper scaling, the final geometry is balanced, with a stable convergence behavior. Consequently, the optimizer

can follow different paths in order to converge and different solution may appear. Because topology optimization is a non-convex optimization problem, there is no unique solution and therefore, multiple final designs can give usable results.

The parameters given in tab. 4.4 were used for the scaling, obtaining similar sensitivities as in the initial case.

Table 4.4: Scaling parameters -1

Objective: Eigenfrequencies	**Constraint 1:** Volume	**Constraint 2:** Stress
1	$1e3$	$1e1$

In the next section, the final design is presented along with a second geometry that uses different scaling parameters in order to analyze their influence.

4.3.2 Results and discussion

The result obtained after 100 iteration is presented in fig. 4.10. The geometry is similar to the one from the previous optimization presented in fig. 4.5, while the main difference between the two cases appears at the created openings. These results reveal that the stress constraint is not governing the optimization process and therefore, the optimization is mainly driven by the eigenfrequencies maximization. Another possible reason can be the fact that the supports that were added for the eigenfrequencies optimization are also the main regions that influence the stresses. In this case, the two problems may be solved by the same support regions.

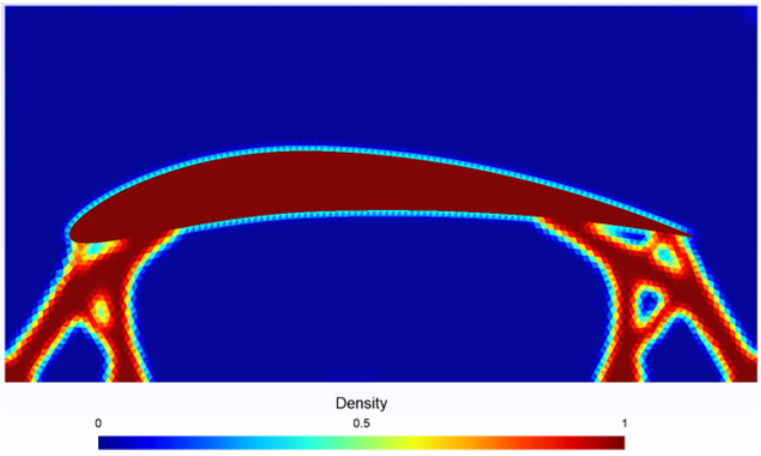


Figure 4.10: $2D$ density based topology optimization result (objective: maximize eigenfrequencies, constraint 1: retain 10% of the initial volume, constraint 2: stresses should be below the allowable value $\sigma_{allowable} = 32.5\,MPa$)

The evolutions of objective and constraints are evaluated as well with respect to iteration number and the corresponding plots are given in figs. 4.11 and 4.12.

The objective evolution with respect to the iterations presented in fig. 4.11 illustrate similar trends compared to the previous case. A rapid improvement is observed in the first iterations and afterwards, larger oscillations appear. These oscillations can be associated with the stress constraint introduction, adding another requirement to the optimization problem. The large oscillation is reduced starting from iteration 40, resulting in a more stable convergence. Essentially, at each iteration, the optimizer redistributed the material in the optimizable domain in order to increase the first three eigenfrequencies, while satisfying both volume and stress constraints.

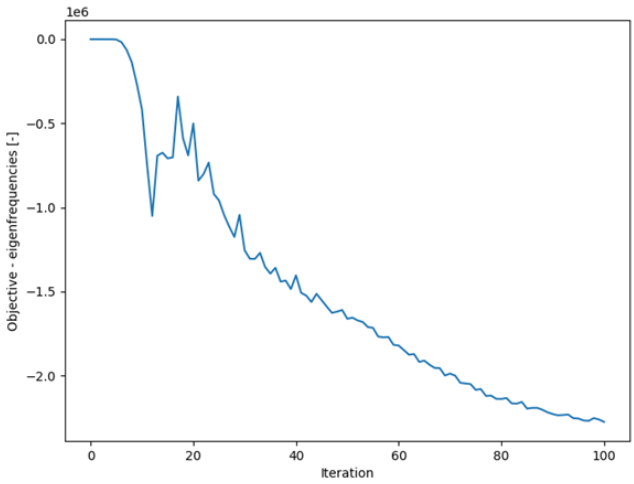


Figure 4.11: $2D$ density based optimization - maximizing eigenfrequencies objective evolution with respect to the iterations - case 2.1

For the volume constraint presented in fig. 4.12, similar behavior to the initial optimization is experienced. As expected, the volume constraint is satisfied and a stable convergence is observed. Small oscillations are experienced during the first half of the optimization, but they are reduced progressively until the optimization ends. Regarding the stress constraint presented in fig. 4.13, it is observed that it is active until iteration 7 and afterwards, it becomes 0. This suggests that the stress constraint is rapidly satisfied and the main design modifications are driven by the objective and volume constraint rather than the stresses. This justifies the similarities between the first optimization and the current case.

The natural frequencies evolution is presented in fig. 4.14, along with the final values for first three frequencies. This evolution exhibits similar trends as in the previous case, but with a less smooth progression due to the multi-constraints formulation. In the current case, the third natural frequency presents a lower value ($f_3^{case2} \approx 2,800\, rad/s$) at the final iteration compared to the first optimization ($f_3^{case1} \approx 5,800\, rad/s$). Although the geometries may look very similar, small differences in intermediate densities or local material distribution can highly affect the higher modes. The corresponding third mode shape can coincide with a different bending or torsional deformation pattern, resulting in different final values.

The stress fields of the isolated airfoil are also evaluated, comparing iteration 0 with iteration 100. The output files from Morfeo were post-processes using Gmsh and the resulted von Mises stresses were obtained. The distributed aerodynamic load was applied on the airfoil edges and therefore, the higher values are observed on the contour, while the airfoil interior presents stresses close to zero, suggesting that the applied force does not produce significant deformation within the domain. The maximum stress obtained is equal to $\sigma = 3.29\, MPa$, which is lower

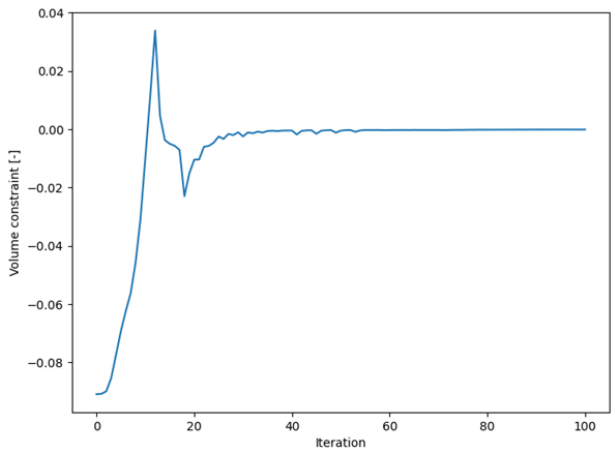


Figure 4.12: $2D$ density based optimization - volume constraint evolution with respect to the iterations - case 2.1

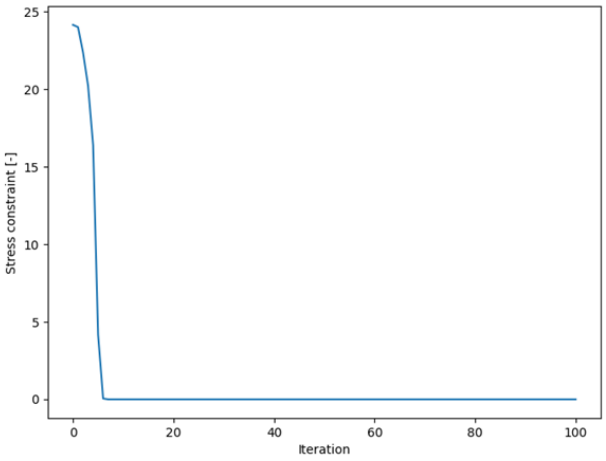


Figure 4.13: $2D$ density based optimization - stress constraint evolution with respect to the iterations - case 2.1

	$f_1[rad/s]$	$f_2[rad/s]$	$f_3[rad/s]$
Iter. 0	20.1	45.7	59.9
Iter. 100	2,403.4	2,661.7	2,825.1

Table 4.5: Natural frequencies - case 2.1

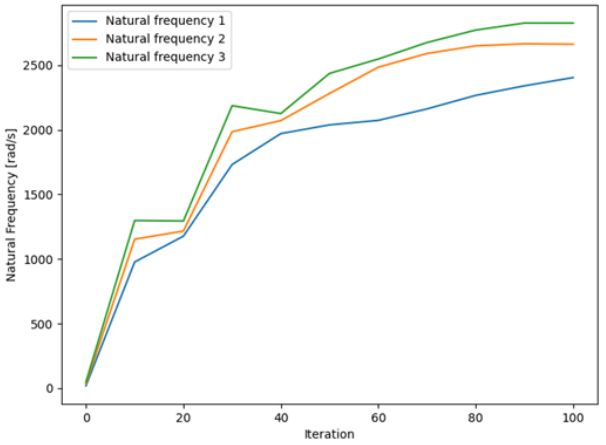


Figure 4.14: $2D$ density based optimization - first three natural frequencies evolution with respect to the iterations - case 2.1

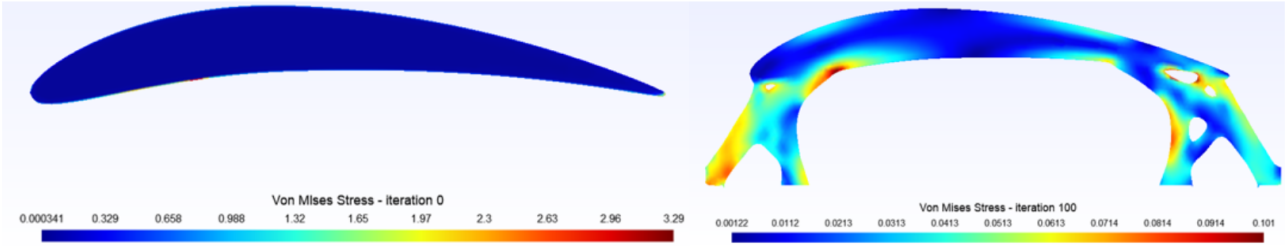


Figure 4.15: $2D$ density based optimization - comparison between stress fields at iteration 0 and 100 - case 2.1

than the imposed limit $\sigma_{allowable} = 32.5\,MPa$. However, the evolution presented in fig. 4.13 reveals that the stress constraint is active for 7 iteration, indicating that the maximum stresses are obtained inside the surrounding domain. Since the density initialization in the optimizable domain was equal to 10^{-6}, a reduced amount of material is available for load transferring and consequently, high local stresses appear. The constraint is satisfied once the optimizer assigns higher densities in the corresponding regions, increasing the structural stiffness.

At iteration 100, the maximum value obtained for the stress is equal to $\sigma = 0.1\,MPa$ which is far below the imposed limit. The airfoil and supports surfaces exhibit small variation, indicating that the applied load is relatively small compared to the stiffness of the resulted geometry.

Overall, similar designs and trends are obtained in these two optimization cases. However, the obtained result is dependent of the scaling parameters. To illustrate this, a different result for different scaling parameters is presented.

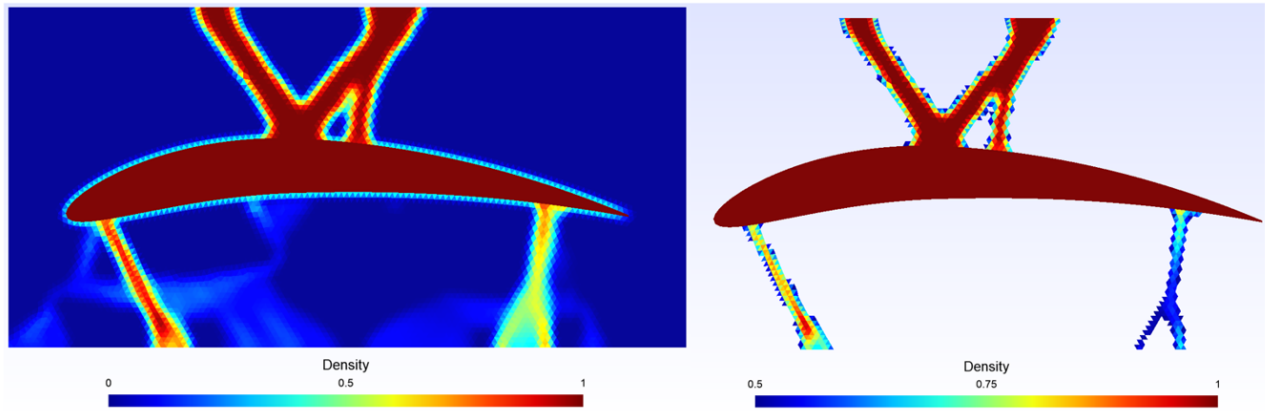
The parameters that are given in tab. 4.8 were chosen for this computation. Compared to the previous set of parameters, the scaling parameter of the stress constraint is now reduced from $1e1$ to 1 such that its numerical influence is reduced. For the volume constraint scaling, the weight is reduced as well from $1e3$ to $1e2$. As a result, the optimizer follows a different path and therefore, a different solution presented in fig. 4.16 is obtained.

Table 4.6: Scaling parameters -2

Objective: Eigenfrequencies	**Constraint 1:** Volume	**Constraint 2:** Stress
1	$1e2$	1

The geometry presents multiple supports, placed in different locations than in the previous case. This confirms that the scaling parameters highly influence the material distribution in the optimizable domain. The upper support that connects the airfoil to the top edge is thicker than the ones in the previous configuration, while the other two are thinner, without any additional openings. Using Gmsh, the densities in the chosen range [0.5, 1] are also shown in fig. 4.16 for a better visualization.

The resulted design is physically meaningful with clear supports in the problematic regions. However, more intermediate densities can be observed, suggesting a poor scaling of the parameters. This behavior reflects a less efficient optimization due to numerical imbalances between the objective and the constraints even though a feasible solution was obtained.



a) Density range [0, 1] ***b) Density range [0.5, 1]***

Figure 4.16: $2D$ density based optimization - obtained result with different parameters for scaling

Considering these results presented in fig. 4.10, adding the stress constraint does not bring additional changes in the final design. The stress constraint is active in the initial iterations and it rapidly decreases to 0, suggesting that the constraint is fully satisfied. Another aspect is that the scaling parameters need to be properly chosen in order to obtain a feasible design. The similarities in terms of magnitudes between the first and the second optimization offers a final geometry with similar ribs system, but when the scaling parameters of the objective and constraints are not properly chosen, different trends are observed.

Because one of the objectives of this work is to demonstrate that the stresses can be decreased using topology optimization, in the next $2D$ optimization case, the maximum stress allowable value is drastically reduced to an arbitrary value, in order to see the evolution of the optimization when the stress constraint is active for more iterations.

4.3.3 Reduced allowable stress

To demonstrate that the stresses can be reduced using this topology optimization setup, a sufficiently low arbitrary value was chosen: $\sigma_{allowable} = 0.3\,MPa$. The same setting are kept for the optimization along with the distributed load and the scaling parameters presented in tab. 4.4 and therefore the stress influence is going to be analyzed.

The current optimization problem can be written as:

$$\begin{aligned} \max_{\boldsymbol{\rho}} \quad & \left(\sum_{i=0}^{n=2} \frac{1}{\lambda_i(\boldsymbol{\rho})} \right)^{-1} \\ \text{s.t.} \quad & \frac{V(\boldsymbol{\rho})}{V_0} \leq 0.10, \\ & \frac{\sigma_{max}(\boldsymbol{\rho})}{\sigma_{allowable}} \leq 1, \\ & 0 \leq \rho \leq 1. \end{aligned} \tag{4.14}$$

Using Morfeo, the geometry presented in fig. 4.17 was obtained after 100 iterations. Once again, a similar pattern for the supports can be observed. Their placement is identical and the only difference that can be identified is represented by the openings. One of the main ribs that is located in the trailing edge zone is slightly bifurcated into two distinct members, while the opening becomes more defined. These modifications ensure that the load is distributed and therefore each rib needs to withstand lower stresses. Additionally, the trailing edge is a problematic area because it is more flexible and due to that, it may need an extra support.

The optimizer modifies certain regions in order to reduce the local stresses, but even for this reduced allowable value, the final design is similar to the baseline optimization. This behavior emphasizes that, for this specific case, the eigenvalues and volume formulation already provides a structurally efficient result that is capable to withstand the applied loads. When the eigenfrequencies are increased, an improvement in terms of global stiffness-to-mass ratio is obtained, creating a stiffer structure that can exhibit lower deformations.

The objective and constraints evolutions were analyzed and the results are presented in figs. 4.18, 4.19 and 4.20.

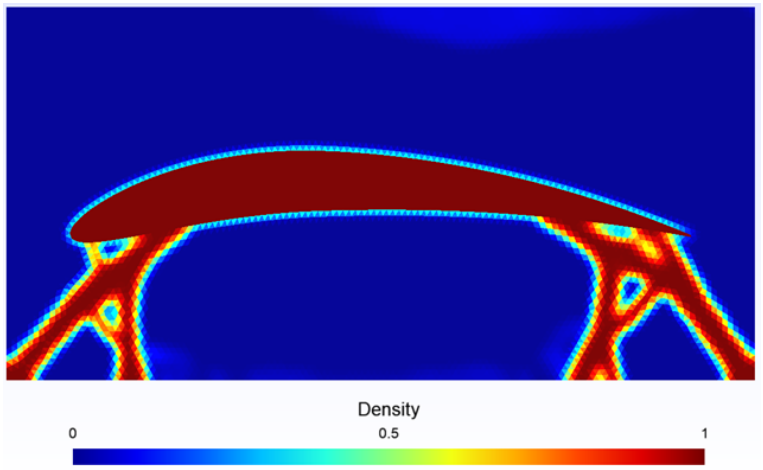


Figure 4.17: $2D$ density based optimization (objective: maximize eigenfrequencies, constraint 1: retain 10 % of the initial volume, constraint 2: stresses should be below the allowable value $\sigma_{allowable} = 0.3\,MPa$)

Firstly, the objective evolution with respect to the iterations presents a similar trend as in the previous optimization and several oscillations are observed. With a lower admissible stress value, the stress constraint is active for more iterations and it contributes more in the design evolution. The optimizer must therefore achieve the maximizing eigenfrequencies objective, while balancing the volume and stress constraint. The problem becomes more sensitive since any material distribution that can satisfy one constraint can temporarily affect the other. Additionally, maximum stress may shift during the iterations, producing more abrupt changes that reflect in the oscillations.

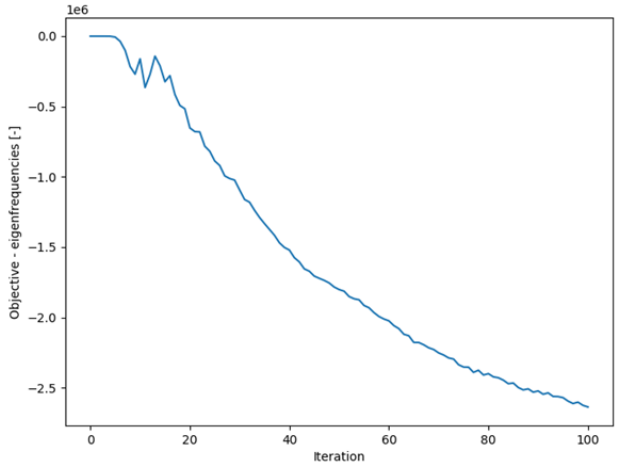


Figure 4.18: $2D$ density based optimization - maximizing eigenfrequencies objective evolution with respect to the iterations - case 2.2

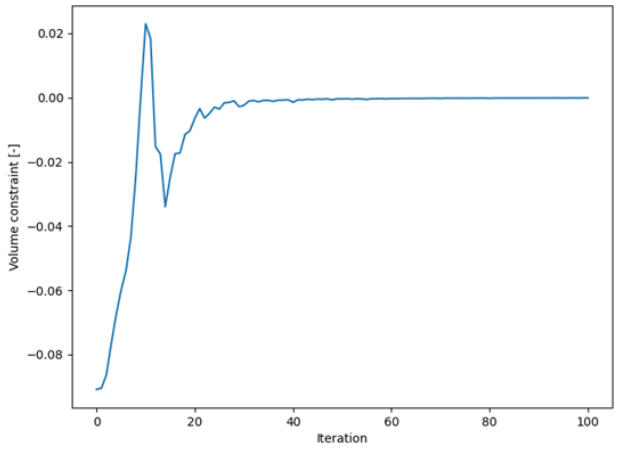


Figure 4.19: $2D$ density based optimization - volume constraint evolution with respect to the iterations - case 2.2

Secondly, the volume constraint presented in fig. 4.19 is satisfied and the results are stabilizing after iteration 60. The trend is similar and small oscillation can be observed in the first half of the optimization process.

Regarding the stress constraint presented in fig. 4.20, previously, it was satisfied after only 7 iterations, but in the current case, a different behavior is observed. In the first 5 iteration, the

constraint value decreases rapidly from 2500 until it reaches lower values. This suggests that the optimizer is distributing the material efficiently and the maximum stresses are reduced. Afterwards, a gradual reduction is identified until iteration 50 while approaching 0, indicating that the optimizer is performing small adjustments in material distribution in order to balance the two constraints. After the first half of the optimization, the stress constraint is fully satisfied.

In the current $2D$ case, the main objective is to demonstrate that stresses can be reduced with this topology optimization formulation. This is clearly shown in fig. 4.20, where the stress constraint is gradually decreasing and stabilizing until it reaches the end of the optimization. Additionally, the similarities between the current case and the baseline confirm that, in $2D$, the final geometry offers a structure with better mechanical performances while treating only the dynamic response of the structure.

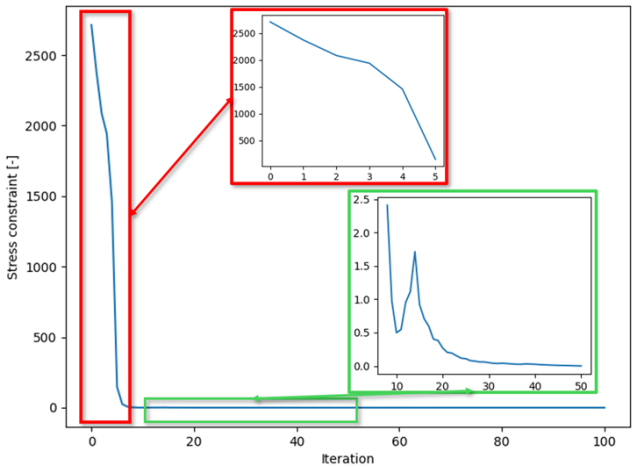


Figure 4.20: $2D$ density based optimization - stress constraint evolution with respect to the iterations - case 2.2

The corresponding natural frequencies variation with respect to iterations is presented in fig. 4.22 and tab. 4.7. A gradual and stable increase is observed and in the final iteration, values starting from $2,500\,rad/s$ are obtained. The third natural frequencies exhibit larger increase in the last 30 iterations, similar to what was observed in the baseline optimization, reaching approximately $3,500\,rad/s$ at the end.

Furthermore, the stress comparison between iteration 0 and 100 is presented in fig 4.22. As it was stated before, the maximum stress $\sigma = 3.29\,MPa$ is obtained on the airfoil edges. By reducing the stress limit to $\sigma_{allowable} = 0.3\,MPa$, the stress constraint becomes more restrictive and therefore, the maximum value obtained at iteration 0 exceeds the prescribed value. To satisfy the constraint, the optimizer is forced to refine the material distribution in the problematic region, resulting in a geometry with well-defined openings. At iteration 100, the maximum stresses obtained are far below the imposed limit, suggesting that the constraint was successfully satisfied.

Additionally, the case where the allowable limit was set to $32.5\,MPa$ already had a large safety margin, since the maximum obtained stress was equal to $\sigma = 0.1\,MPa$. This indicates that the optimized structure is conservative and not governed by the imposed stress constraint. When the lower admissible limit is imposed, the stress field displays a maximum value equal to $0.1\,MPa$, suggesting that the overall topology remains unchanged and only local refinement is

	$f_1[rad/s]$	$f_2[rad/s]$	$f_3[rad/s]$
Iter. 0	20.1	45.7	59.9
Iter. 100	2,449,8	2,736.9	3,552.6

Table 4.7: Natural frequencies - case 2.2

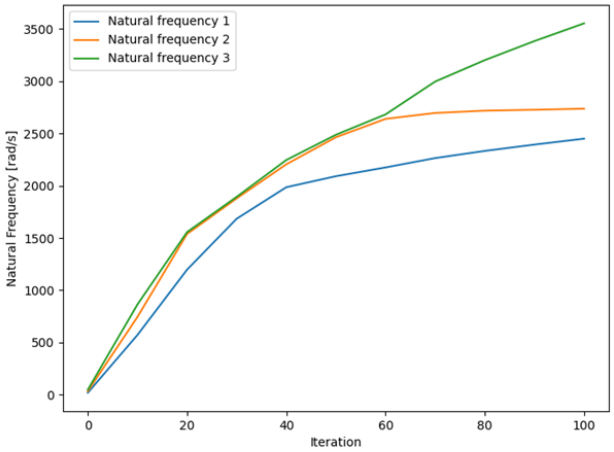


Figure 4.21: $2D$ density based optimization - first three natural frequencies evolution with respect to the iterations - case 2.2

needed. However, the objective of this case was to demonstrate that the stresses can decrease and therefore, a larger contribution is considered while defining the final design.

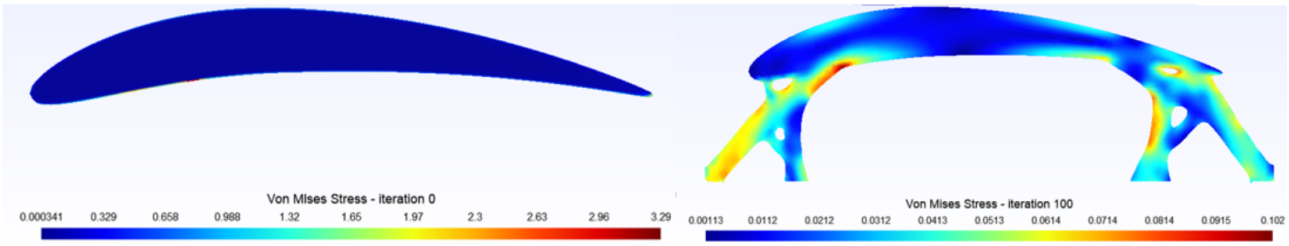


Figure 4.22: $2D$ density based optimization - comparison between stress fields at iteration 0 and 100 - case 2.2

By imposing a drastic maximum limit for the stresses, the optimizer is forced to improve the mechanical capabilities even more. When this is set, the stresses are decreasing progressively and when the constraint becomes fully satisfied, small adjustments are performed on the geometry. The similarities between the three cases indicate a robust model, demonstrating that the baseline result is also effective from a mechanical perspective.

4.4 Eigenfrequency maximization under multiple loads with volume and stress constraints

In the previous optimization, the equivalent distributed force presented in section 4.1.1.1 was applied on the airfoil contour, representing an approximation of the aerodynamic loading. The main objective was to demonstrate that the stresses can be reduced to very low values and the corresponding trends were analyzed. In contrast, the purpose of the current case is to analyze the effects of a realistic aerodynamic load presented in 4.1.1.2 on the resulted geometry. This approach is able to capture the non-uniform aerodynamic pressure distribution while maintaining the same optimization framework.

4.4.1 Problem formulation

In this last $2D$ optimization, the aerodynamic loads obtained from the CFD projection and described in section 4.1.1.2 are applied on the airfoil edges. Thus, a valid spatial representation of the pressure is applied, creating a final intermediate step before the full $3D$ optimization.

The blade contour Γ_p described in fig. 4.9 was discretized in 207 edges resulted from the meshing process. For each edge, two loads are applied (one for $x-$ and one for $y-$ axes), resulting in a total of 414 forces applied on the whole contour. Additionally, to preserve the realism of the problem, the original maximum value is used for the stress constraint.

The multi-constraints optimization framework is maintained and can be written as:

$$\begin{aligned} \max_{\boldsymbol{\rho}} \quad & \left(\sum_{i=0}^{n=2} \frac{1}{\lambda_i(\boldsymbol{\rho})} \right)^{-1} \\ \text{s.t.} \quad & \frac{V(\boldsymbol{\rho})}{V_0} \leq 0.10, \\ & \frac{\sigma_{max}(\boldsymbol{\rho})}{\sigma_{allowable}} \leq 1, \\ & 0 \leq \rho \leq 1, \end{aligned} \tag{4.15}$$

where the $\sigma_{allowable}$ is set to $32.5\,MPa$.

For all $2D$ optimizations, a scaling parametric study was performed in order to balance the effects of each function and the final geometries were analyzed. Since the magnitudes of the functions were changed when multiple loads are applied, the default parameters were chosen. The corresponding set of parameters ensures that the objective and the constraints have comparable magnitudes, offering balanced contributions during the optimization with stable convergence behavior. Apart from this modification, all the other settings were kept unchanged.

Table 4.8: Scaling parameters - 3

Objective: Eigenfrequencies	**Constraint 1:** Volume	**Constraint 2:** Stress
1	1	1

4.4.2 Results and discussion

The result presented in fig. 4.23 was obtained after 100 iterations. As expected, the result is very similar to the previous cases, even though multiple loads were applied in order to capture the aerodynamic effects. Small differences appear in the openings area, where more defined empty regions are observed in the trailing edge support. This can be explained by the fact that slightly larger loads were applied in those regions using the current setup and therefore, the rigidity was marginally modified but adding or removing intermediate densities.

Even though this load representation captures local effects, the final geometry remains very similar to the previous result, emphasizing that the distributed load defines a good approximation that can be used in preliminary design phases. Both loading scenarios were determined from the same CFD simulation and although one of them is more precise, the global force acting on the airfoil is similar.

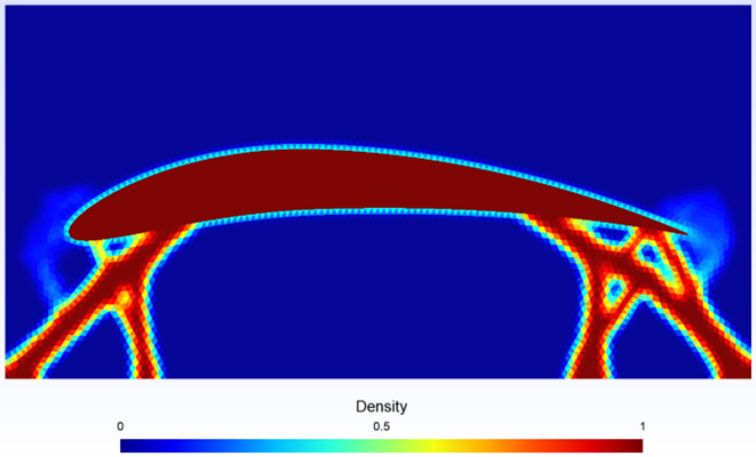


Figure 4.23: $2D$ density based optimization with multiple loads (objective: maximize eigenfrequencies, constraint 1: retain 10 % of the initial volume, constraint 2: stresses should be below the allowable value $\sigma_{allowable} = 32.5\,MPa$)

The objective and constraints evolutions were analyzed with respect to the iterations and the results are presented in figs. 4.24, 4.25 and 4.26. For the objective, a smooth evolution is observed, without many oscillations. Similar to this case, in fig. 4.11, when a distributed load was applied and a $32.5\,MPa$ limit was imposed, the response displayed a fluctuating behavior rather than a smooth and continuous decrease in the scaled function. This response can be a consequence of the multi-load representation, where the pressure distribution evolved gradually, producing a more realist load transfer to the airfoil. The design sensitivities could evolve smoothly and smaller design modifications are performed, without introducing many oscillations.

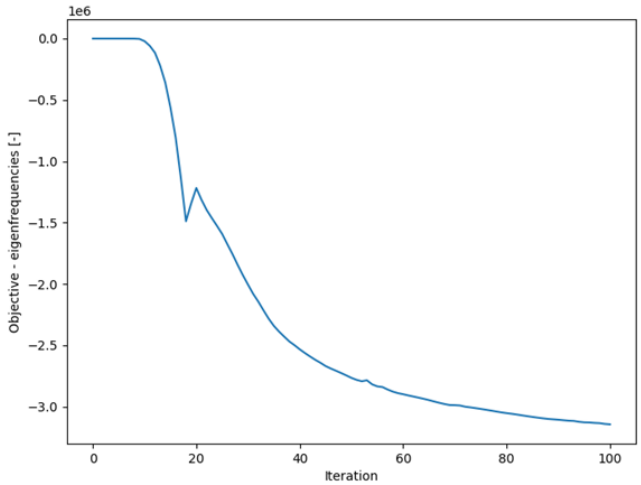


Figure 4.24: $2D$ density based optimization - maximizing eigenfrequencies objective evolution with respect to the iterations - case 3

The volume constraint evolution with iterations is presented in fig. 4.25. A similar smooth pattern is observed, where the constraint is satisfied after approximately 20 iterations. Regarding the stress constraint, it is active for 11 iterations, indicating an efficient material distribution in the design domain. In the equivalent case with distributed load, the stress constraint was active for only 5 iterations, suggesting that the initial stress was higher. Therefore, this constraint had a larger influence on the final design, while the optimizer was redistributing material over a larger number of iterations in order to satisfy this constraint. The overall trends suggest that gradual updates were performed, resulting in smoother curves and a more defined supports system.

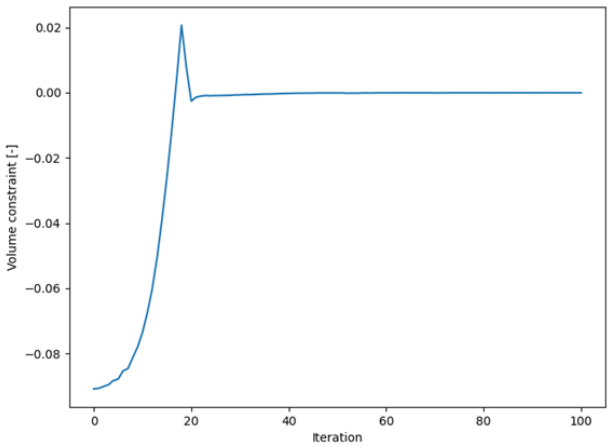


Figure 4.25: $2D$ density based optimization - volume constraint evolution with respect to the iterations - case 3

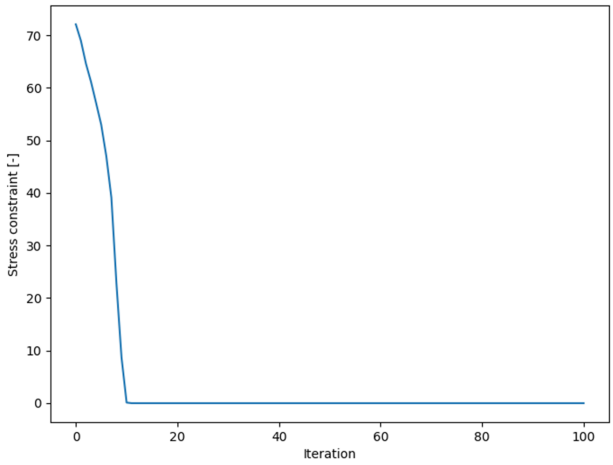


Figure 4.26: $2D$ density based optimization - stress constraint evolution with respect to the iterations - case 3

The natural frequencies evolution presented in fig. 5.8 and tab. 4.9 illustrate an almost identical behavior to the baseline case, where the third frequency was increased significantly compared to the first two. In this case, a value of approximately $5,300\,rad/s$ was obtained, while in the baseline case, $5,800\,rad/s$ was found.

	$f_1[rad/s]$	$f_2[rad/s]$	$f_3[rad/s]$
Iter. 0	20.1	45.7	59.9
Iter. 100	2,594.5	2,724.1	5,371.9

Table 4.9: Natural frequencies - case 3

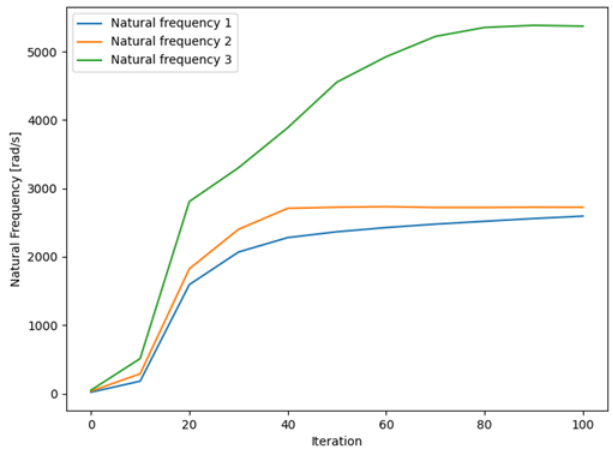


Figure 4.27: $2D$ density based optimization - first three natural frequencies evolution with respect to the iterations - case 3

Overall, these convergence similarities between the current case and the baseline indicate that the dominant structural load path is identified even from the beginning. This suggests that the eigenfrequencies maximization represent the primary driver in the optimization, while the volume constraints ensures that only a small fraction of material is added. The local refinement is determined by the stress constraints, which controls the openings and potential bifurcations.

The stress comparison between iteration 0 and 100 is presented in fig. 4.29. With multiple loads applied, higher stresses are obtained in the trailing edge area, where the values equal to $\sigma = 37.7\,MPa$ are obtained, exceeding the maximum allowable limit. This problematic region forces the optimizer to attach the airfoil using ribs to the clamped edges, in order to increase the mechanical performances. At iteration 100, low values are noticed in the field where the maximum stress obtained is equal to $\sigma = 1.3\,MPa$ near the leading edge support. Two main supports are created and several openings are formed, increasing the overall stiffness of the structure.

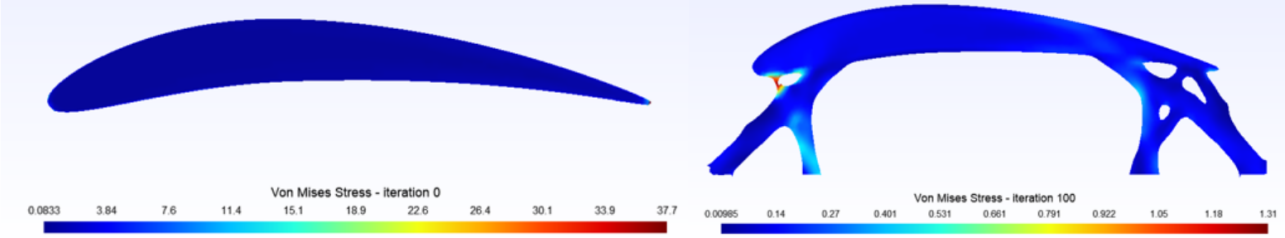


Figure 4.28: $2D$ density based optimization - comparison between stress fields at iteration 0 and 100 - case 3

The primary objective of this $2D$ study was to create an intermediate validation step that can facilitate rapid parametric studies, while analyzing the influence of different optimization strategies. Therefore, the gained information can directly be transferred to the three-dimensional blade topology optimization, following the same steps. A summary for these cases along with their relevant conclusions are presented in the following section.

4.5 Comparison of the 2D optimization cases

A comparison between the four cases is presented in fig. 4.29. For a better visualization of the final geometries, the densities between [0.5, 1] were retained using Gmsh.

The $2D$ study was driven by the need to obtain rapid results with significant relevance for the $3D$ topology optimization. Progressively, additional alternatives were explored, investigating the influence of several configurations, parameters and loads. The similarities in terms of geometries between the cases are relevant, presenting a robust setup that offers information that can be directly translated into the $3D$ topology optimization cases.

The first case presented in fig. 4.29 (a), an eigenfrequencies maximization along with a volume constraint formulation is used, since the maximization of the first three natural frequencies is assumed to increase the separation between the structural natural frequencies and the aerodynamic excitation frequencies that are associated with flutter instability. Additionally, because the simplified blade resumes several characteristics of a distortion grid system, a reduction of 90 % of the initial volume was imposed in order to obtain thin supports that can

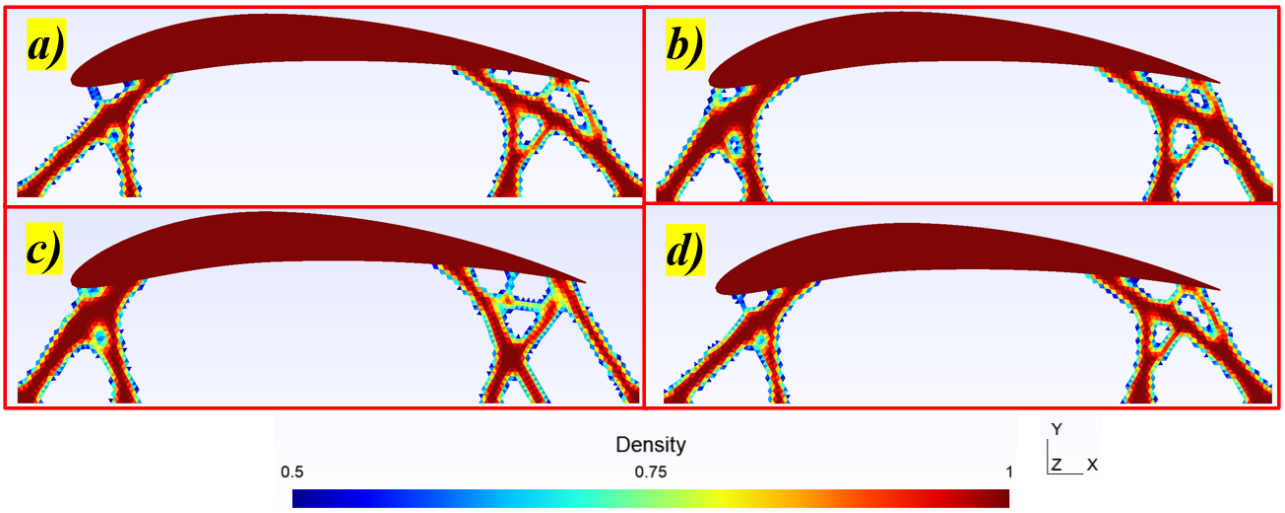


Figure 4.29: $2D$ density based optimizations - comparison between *case (a)* (eigenfrequency maximization and volume constraint), *case (b)* (addition of the stress constraint - $\sigma_{allowable} = 32.5\,MPa$), *case (c)* (reduced allowable stress - $\sigma_{allowable} = 0.3\,MPa$) and *case (d)* (multiple-load - $\sigma_{allowable} = 32.5\,MPa$)

allow the flow to pass without major disturbances. Within this case, the scaling parameters were initially adjusted in order to obtain a balanced final design, while the other setting were also fixed for the future optimizations. A stable convergence was observed and a network of ribs were created.

The second case illustrated in fig. 4.29 (b) introduced the stress constraint where $\sigma_{allowable}$ was set to $32.5\,MPa$. Using this configuration where two constraints were added, the scaling weights were modified in order to obtain a feasible result. An unbalanced set of parameters can generate non-physical structures with multiple zones with intermediate densities and during this optimization, the importance of this balance was remarked. The final result displays a more oscillatory convergence along with a similar geometry. The stress constraint was active for 7 iterations, indicating that the stress was not the main driver in this optimization.

The third case presented in 4.29 (c) treated an optimization where the maximum allowable stress was drastically reduced to $0.3\,MPa$. The objective was to demonstrate that the stresses can be reduced using the presented formulation and the final result presented thicker supports, well-defined openings and a bifurcation for the trailing edge support. The constraint was active for 50 iterations and therefore, the final design was severely influenced by it.

The last case presented in fig. 4.29 (d) used the $32.5\,MPa$ as the maximum allowable and multiple loads were applied on the airfoil edges. Both the final geometry and the convergence behavior were very similar to the baseline, illustrating that the initial configuration had good mechanical performances. For this specific $2D$ case, the simplified framework defined by the eigenfrequencies maximization while retaining a small fraction of the volume offers a feasible result from a static and dynamic point of view.

Overall, similar results were obtained, emphasizing that the baseline formulation is robust with respect to the applied changes in loading or imposed stresses. The main differences appeared locally and they were observed in rib thickness, internal openings or convergence behavior. The simplified two-dimensional study was used in identifying the influence of several

functions or settings such as the scaling parameters that will be used in the $3D$ computations, while in the three-dimensional cases, multiple differences are expected, since these cases include a larger design space with a higher number of design variables, more complex load transfer mechanisms and torsional effects.

Chapter 5

Topology optimization applied to three-dimensional model

After establishing $2D$ topology optimizations, three-dimensional cases are defined in this chapter. An identical approach is used here, treating four optimization cases and analyzing the corresponding results.

5.1 Model definition

The three-dimensional model corresponds to the geometry presented in section 3.2. As it can be observed in fig. 5.1, the extruded blade based on NACA 9410 airfoil is placed inside a large domain, leaving enough space in order to create supports between the blade and the domain boundaries. During the computations, four faces of the domain are fully clamped, representing the walls of the wind tunnel, along with the bottom surface of the blade. The rest of the blade along with the two domain surfaces that are corresponding to the inlet and outlet are left unconstrained.

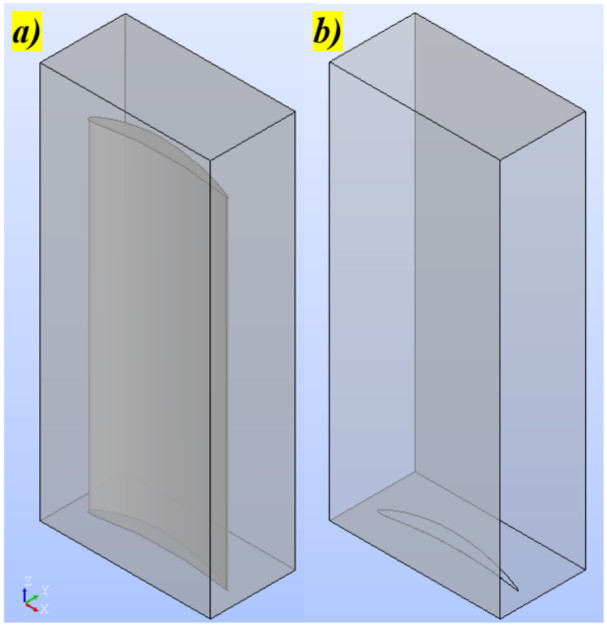


Figure 5.1: Three-dimensional topology optimization configuration - a) NACA 9410 airfoil extruded $2.4\,c$ with its corresponding surrounding domain, b) clamped regions containing four surfaces and the bottom surface of the blade

Similar to the two-dimensional cases, the primary objective is to increase the mechanical performances of the blade by creating additional supports between its surface and the clamped regions.

The same material is used for the geometry and the corresponding properties were given in tab. 3.1. The mesh is obtained using Salome Meca, applying the NETGEN 1D-2D-3D algorithm. An unstructured tetrahedral mesh is generated and $170,775$ nodes and $1,005,750$ linear elements are obtained. This included $931,612$ linear tetrahedral elements, $72,850$ triangular surface elements and $1,288$ edge elements.

5.1.1 Loading conditions

In the following sections, four optimization cases are presented, similar to the $2D$ cases. The first one takes into account the eigenfrequencies maximization with respect to a volume constraint, the second and third configuration use the same configuration as in the baseline and adds the distributed force discussed in section 4.1.1.1, while the fourth one relies on a more realistic representation of the pressure distribution presented in fig. 3.10. The distributed force application offers a simplified loading condition obtained from the CFD computation, without introducing the complexity of a non-uniform pressure field, facilitating the analysis of the global trends. In contrast, the realistic loading condition is used to assess whether the methodology remain effective under a physically representative loading condition, while capturing the local effects.

The blade outer surfaces were divided into multiple faces and for each face, a value for the pressure was assigned. This procedure created an accurate representation of the obtained aerodynamic forces, capturing details from the CFD computation.

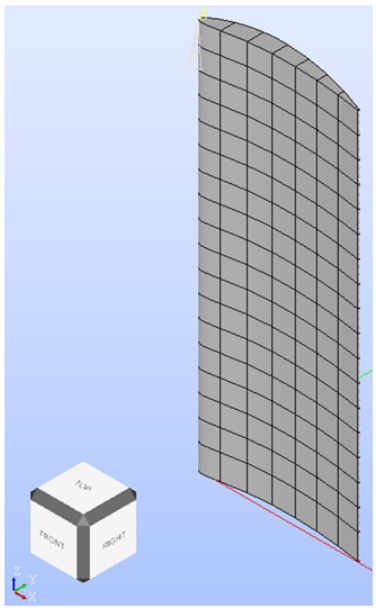


Figure 5.2: Blade faces created for the CFD pressure projection

Using Salome Meca, 270 groups were created as it is presented in fig. 5.2. The division ensures that the local effects are captured, while creating a more detailed representation than in the distributed force case. Therefore, for each group, a pressure is assigned and the mechanical constraint is added in the optimization framework.

To begin with, the center of the each element face is computed and the nearest CFD point is found. Its pressure is assigned to the new point such that:

$$p_i = p_{nearestCFD} \tag{5.1}$$

and afterwards, the area A_i and the corresponding normal $\mathbf{n_i}$ are computed. Therefore, each element from the blade mesh has a pressure, an area and a normal assigned. The force vector for each element is computed as:

$$\mathbf{F_i} = -p_i \cdot \mathbf{n_i} \cdot A_i, \tag{5.2}$$

Subsequently, for each group, the total area is given by:

$$A_{group} = \sum A_i, \tag{5.3}$$

and the mean pressure with respect to the area is computed as:

$$\bar{p}_{group} = \frac{\sum_i p_i \cdot A_i}{\sum_i A_i} \tag{5.4}$$

Each face group has one representative normal with respect to the area:

$$\bar{\mathbf{n}}_{\mathbf{group}} = \frac{\sum_i \mathbf{n_i} \cdot A_i}{||\sum_i \mathbf{n_i} \cdot A_i||} \tag{5.5}$$

and using it, the corresponding force is obtained, along with its x and y components:

$$q_x = \frac{F_x}{A_{group}}, \quad q_y = \frac{F_y}{A_{group}}. \tag{5.6}$$

The process is similar to the $2D$ aerodynamic loads extraction and the pressure distribution presented in fig. 5.3 is obtained. The comparison displays a good agreement between the initial pressure distribution determined from the CFD simulation and the projection results using multiple face groups. The local trends are maintained and the mapped pressure values reproduce the reference solution. Since the projection case represents an approximation, a similar pressure range is obtained. The locations of the maximum and minimum pressure values are preserved, while the overall variation remains consistent on the blade surface.

5.2 Eigenfrequency maximization with a volume constraints

In this section, a first three-dimensional optimization is presented and similar to the first two-dimensional case, the eigenfrequencies maximization with a volume constraint is taken into account.

5.2.1 Problem definition

A density based topology optimization formulation is used, similar to the two-dimensional case. The objective is represented by eigenfrequencies maximization and the 10 % volume constraint is imposed in order to obtain thin supports distributed around the blade. The problem formulation corresponds to equation (4.11).

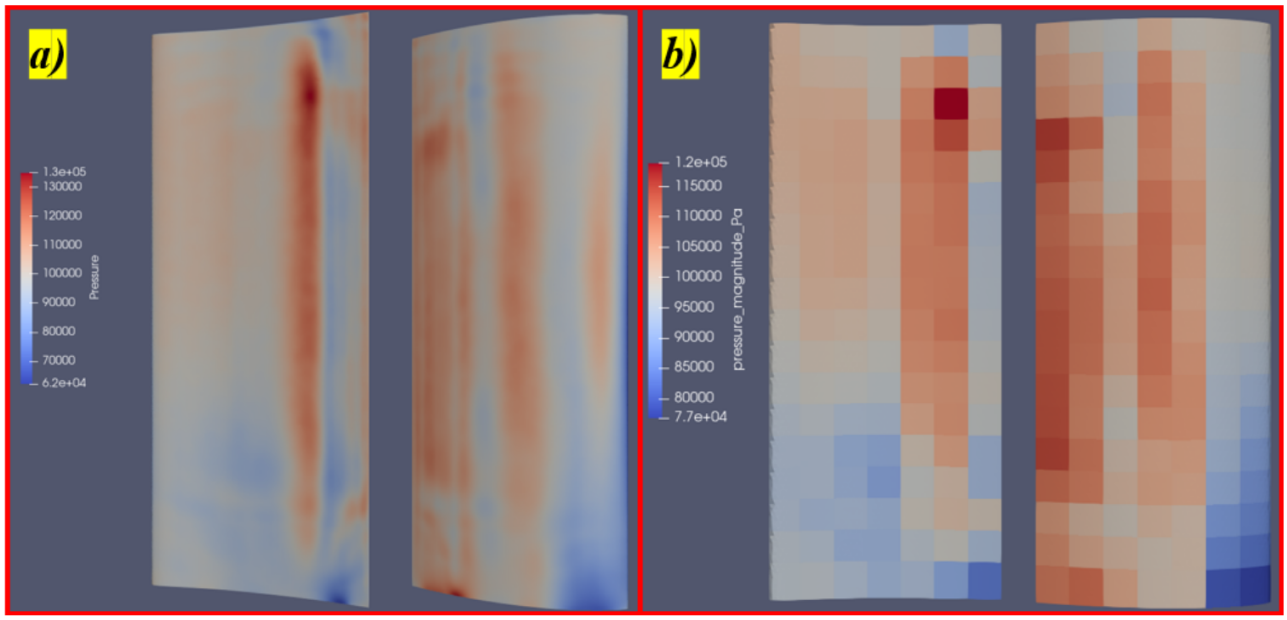


Figure 5.3: Comparison between a) CFD pressure at the interface and b) resulted pressure distribution using the projection

In fig. 5.4, the domains are presented in different colors such that $\Omega = \Omega_d \cup \Omega_{nd}$. The blade domain is written as Ω_{nd}, represented in orange. This volume remains unmodified during the optimization process, representing the non-optimizable domain. Because the aim is to increase the stiffness by creating connection between the clamped walls and the blade surface, the surrounding volume illustrated in blue is denoted as Ω_d, representing the optimizable part with its corresponding clamped surfaces highlighted in purple, Γ_{fix}. Only the bottom surface of the blade along with the bottom and lateral faces of the surrounding domain are fully clamped, while the inlet and outlet boundaries are free.

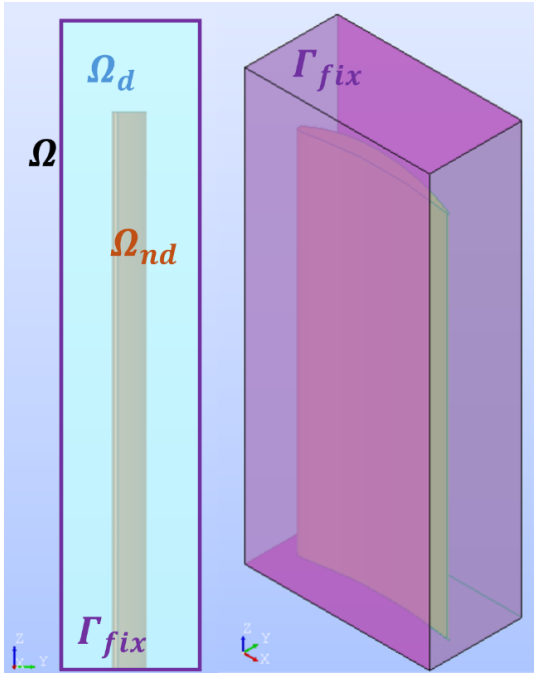


Figure 5.4: Design domain and boundary conditions for the $3D$ topology optimization problem - case 1

The SIMP interpolation with the same parameters as before is maintained, while the radius of the density filter is modified since the local lengths are modified. The local edges length is approximately $0.3 - 0.5$ and a filter radius equal to 1.5 is imposed. For the scaling settings, the default parameters were used, as it was described in the corresponding $2D$ case.

5.2.2 Results and discussion

The final result presented in fig. 5.5 is obtained after 100 iterations. To highlight the results more clearly, the geometry was visualized in Gmsh, retaining only the densities between [0.5, 1]. For the final $3D$ topology optimization result, all views are displayed in order to show the regions that have a significant contribution to the structural response, while regions where $\rho < 0.5$ correspond to low-density or void regions. By setting the objective to maximize the first three eigenfrequencies, the optimizer is redistributing material in order to increase the stiffness-to-mass ratio. As fig. 3.3 shows, the first mode corresponds to a global bending, while the second one represents a torsional mode. The third mode displays a more complex deformation, mainly governed by a bending motion. Due to these characteristics, several supports were created in order to obtain a structure that exhibits smaller local deformations.

The members connecting the blade to the clamped walls are located around it, in regions that exhibit large modal deformations. Therefore, the blade is clamped in the top region on both sides, suppressing the large bending motion observed in the mode shapes representations. In the middle part, several supports are created. Since this region is highly deformed in all three mode shapes, the optimizer attached the blade in critical points. The second mode displayed a torsional mode and therefore, the structure is fixed in four points on the pressure side, illustrated in the second lateral view. The root of the blade is slightly thicker since the optimizer added material in order to reduce the bending moments and to create a gradual load transfer.

In the top view, small disconnected parts are observed, indicating that those regions present a smaller contribution to the global response. They could be related to the density based optimization and the visualization range, suggesting that their connections to the blade can be done with lower densities than 0.5.

Overall, the pressure side displays a larger number of supports, indicating that, under this formulation, creating substructures there provide an efficient increase in terms of global stiffness-to-mass ratio. The supports appear to be thick in this visualization method, since the transition layer between the solid and the void is retained by the 0.5 densities. It can be observed that the supports core are displaying densities closer to $0.8 - 0.9$ which correspond to a solid region.

Similar to the $2D$ case, the objective and constraint evolutions presented in figs. 5.6 and 5.7 are analyzed with respect to iteration number, in order to evaluate the convergence behavior. For the objective evolution, a general decrease tendency is observed. Unlike the $2D$ case where smooth curves were obtained, the presented evolution with respect to iterations displays noticeable oscillations and local peaks, suggesting that the optimizer is continuously redistributing material in order to achieve the objective while satisfying the volume constraint. A possible explanation for this behavior could be represented by the large number of design variables and several load paths. Since each element has its own assigned density, small sensitivity changes can influence larger regions, while the optimizer is relocating the material in order to balance the objective and the constraint.

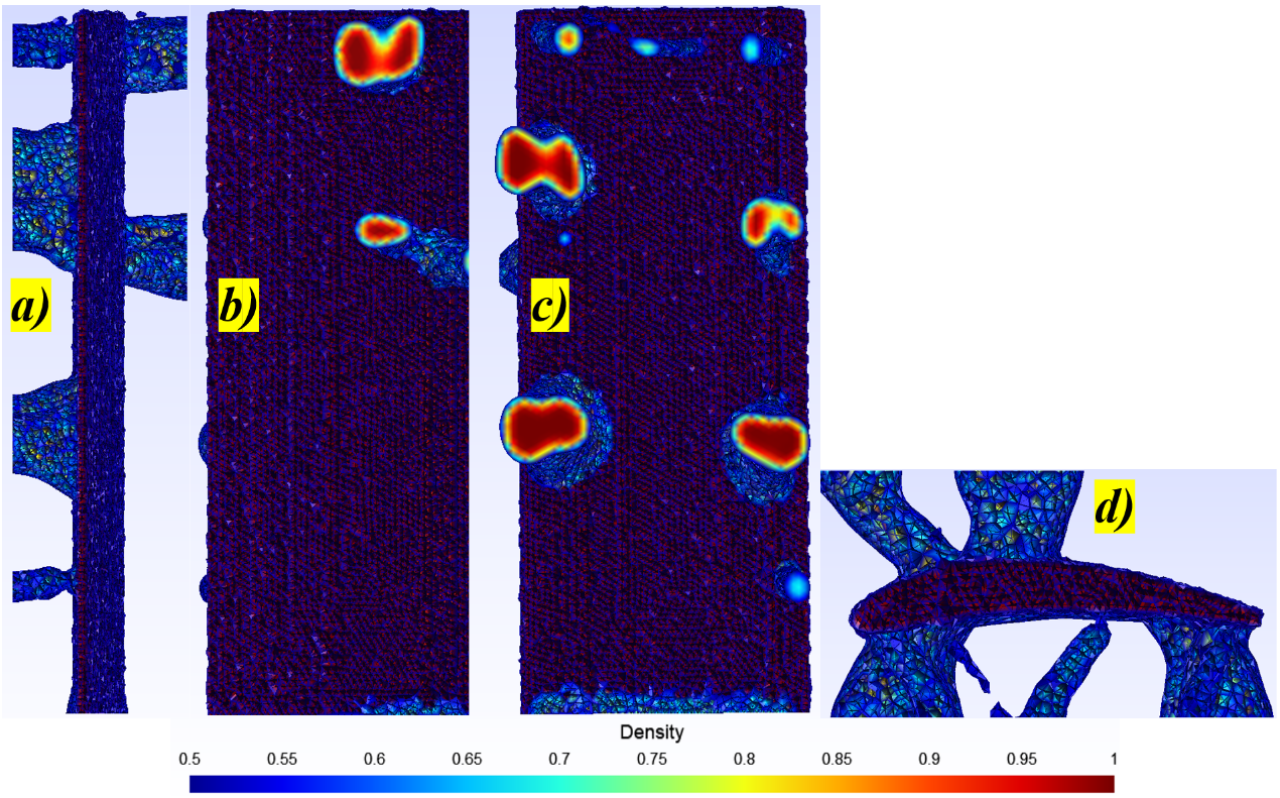


Figure 5.5: $3D$ density based topology optimization result (objective: maximize the first three eigenfrequencies, constraint: retain 10 % of the initial volume) - a) front view, b) lateral view 1, c) lateral view 2, d) top view with [0.5, 1] retained densities.

The volume constraint evolution presented in fig. 5.7 shows a similar behavior to the objective, with oscillations and local peaks. Temporary deviations from the 10% target occur, but in the final iterations, the oscillations are less pronounced, indicating a progressive stabilization. The volume constraint is evaluated at the final iteration such that:

$$\frac{V}{V_0} - \epsilon_{vf} = -0.0012 \quad with \quad \epsilon = 0.1 \Rightarrow \frac{V}{V_0} = 0.098, \tag{5.7}$$

suggesting that the volume constraint is satisfied since the final ratio is lower than the imposed 0.1 fraction.

The eigenfrequencies are extracted every 10 iterations and the evolution is presented in fig. 5.8, along with the corresponding values presented in tab. 5.1. Unlike the smooth increases observed in the $2D$ optimizations, in the presented case, successive increases and decreases are visible due to a continuous material redistribution that modifies the stiffness and mass. Since each change influences the dynamic response, fluctuations appear, while in the final iterations, the values are reaching a plateau. The three natural frequencies reached $2,446\,rad/s$, $2,478\,rad/s$ and $2,494\,rad/s$, respectively.

The final mode shapes of the structure were extracted and presented in fig. 5.9 in order to compare them with the initial ones displayed in fig. 3.3. Therefore, the mode shapes were computed using Morfeo and post-processed using the ParaViS module integrated in Salome Meca, where the densities between 0.5 and 1 were retained. The same scaling factor was used in order to facilitate a better visualization. In the initial configuration with the clamped blade at one end, mode 1 and 3 exhibited a bending motion, while mode 2 was dominated by

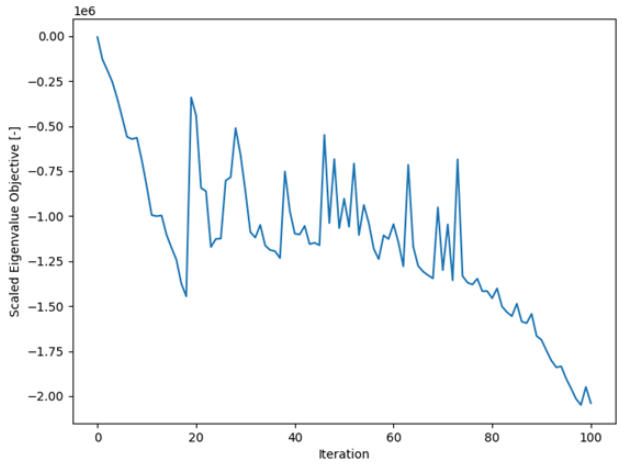


Figure 5.6: $3D$ density based optimization - maximizing eigenfrequencies objective evolution with respect to the iterations - case 1

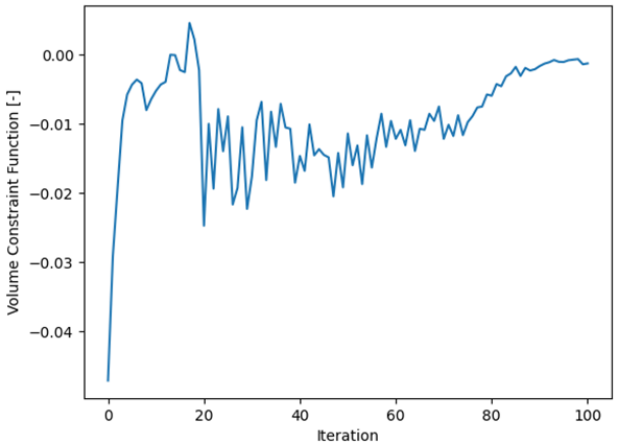


Figure 5.7: $3D$ density based optimization - volume constraint evolution with respect to the iterations - case 1

	$f_1[rad/s]$	$f_2[rad/s]$	$f_3[rad/s]$
Iter. 0	82.9	272.1	379.7
Iter. 100	2,446.5	2,478.3	2,494.7

Table 5.1: Natural frequencies - case 1

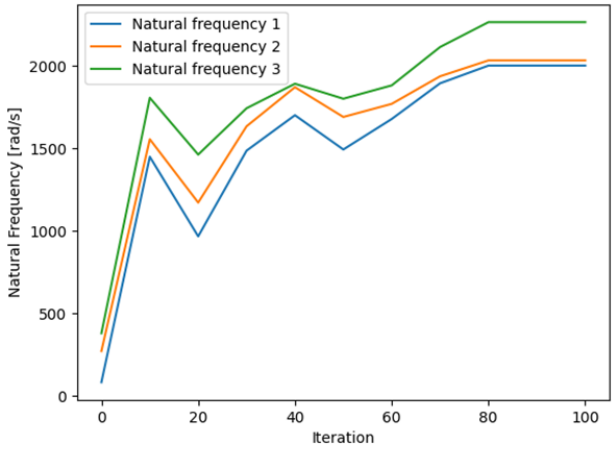


Figure 5.8: $3D$ density based optimization - first three natural frequencies evolution with respect to the iterations - case 1

torsion. At iteration 100, it is observed that the largest displacements are concentrated in the unconstrained regions, where there are no created supports. For mode 1 and 3 at the final iteration, the bending deformation is less pronounced, presenting only localized deformation in zones that are not fixed with the supports. For mode 2, the torsional deformation appears to be reduced and therefore, the optimizer increases the resistance to the torsional deformation by adding several supports to secure the blade. The four supports presented in fig. 5.5 (c) appear to have a considerable influence on this reduction, while small localized deformations are identified.

This comparison emphasizes that the structure's stiffness was increased, reducing the modal deformations by creating attachments between the domain's walls and the blade. The material redistribution reduced the deformation amplitude and only local effects are observed.

Overall, the first $3D$ optimization case offered an expected result, with multiple supports attached around the blade in the critical regions. The objective is reached, while the volume constraint is satisfied, increasing the blade mechanical performances, while still letting the flow to pass around its surface.

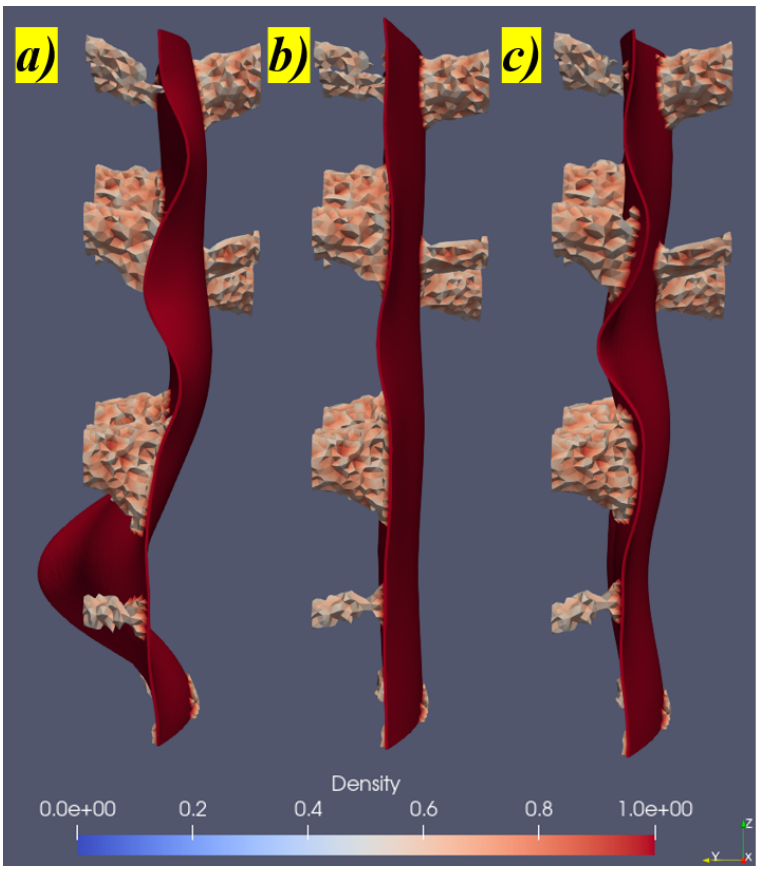


Figure 5.9: First three mode shapes of the obtained geometry with [0.5, 1] retained - case 1

5.3 Eigenfrequency maximization under a distributed load with volume and stress constraints

Previously, only the dynamic response was treated, while in the current $3D$ optimization case, a stress constraint is added by imposing the distributed force on the blade surface.

5.3.1 Problem formulation

The distributed force presented in section 4.1.1.1 is applied on both pressure and suction side of the blade, similar to the second $2D$ case. On x direction, $-1438.37\,Pa$ are imposed, while on y, $-695.78\,Pa$ are applied. Thus, the optimizer is expected to allocate material along the principal load transfer paths, while the main structural members are expected to be placed in the same position since the eigenfrequencies maximization objective is not changed. This would result in a similar geometry with performed local adjustments in order to satisfy the stress constraint while still remaining below the 10 % volume limit.

The current formulation is similar to the one presented in the corresponding $2D$, written in equation (4.13). Therefore, the objective is represented by the maximization of the first three eigenfrequencies, while a 10 % volume constraint is imposed, along with an additional constraint that ensures that the stresses are below $32.5\,MPa$ in the final iteration.

For the scaling parameters, the default values presented in tab. 4.8 are used, while in the corresponding $2D$ case, 1 was used for the objective, $1e3$ for the volume and $1e1$ for the stress constraint. The differences appear because of the larger design space and therefore, difference

numerical scales are observed in the current case. A poor scaling in $3D$ would offer results that follow an unbalanced search direction, resulting in unfeasible geometries with multiple intermediate densities, rather than clear shapes with densities around the solid state.

5.3.2 Results and discussion

The result presented in fig. 5.10 was obtained using Morfeo and the densities between [0.5, 1] are retained. The supports distribution is slightly different, while the main ones are kept in the same regions, indicating that those parts are highly contributing to the eigenfrequencies maximization. In this case, the supports are thinner and distributed in critical regions of the blade.

In fig. 5.10 (d), the top view is presented, emphasizing that, on the pressure side, two main regions are defined and the supports are placed at the two extremities of the structure, while on the suction side, only the middle is clamped. This suggests that the middle part supports are highly contributing to stress reduction and stiffness, while the pressure sides supports control local deformations. Unlike the previous case, there is no material added around the root.

Since the eigenfrequencies maximization was set as an objective, the structure becomes more resistant to bending and torsional deformations. The most critical region is the top part and due to this, a thick support is created in the middle in order to clamp the blade and to reduce the bending displacement magnitude. Another critical zone is represented by the mid-span region that is highly affected by the torsion. Therefore, two large supports are created at the blade extremities in order to reduce the torsion effect and to increase the second mode shape. Additional small supports are added around the blade, contributing to local effects and to eigenfrequencies maximization. Because of the imposed volume fraction, the material needs to distributed strategically in order to suppress the main effects along with local deformations, resulting in a geometry that preserves the main structural framework, while still treating the isolated phenomena.

The scaled objective evolution is plotted with respect to the iterations in fig. 5.11, presenting an oscillatory behavior, with a general decrease tendency. In the first 20 iterations, a drastic decrease is observed, suggesting that the optimizer distributes material in an efficient way. In the following iterations, the objective exhibits several oscillations. The oscillations become more limited indicating a slow and progressive stabilization, reflecting a continuous search done in order to place material in critical regions. It should be noted that, in the first 20 iterations, generally, intermediate densities are created, placing higher densities elements around the blade first and then progressively, the supports creation process starts toward the clamped surfaces.

The volume constraint is also presented with respect to the iterations in fig. 5.12. Similar to the first $3D$ case, an oscillatory evolution is identified. In the first 20 iterations, the constraint exhibits a smooth increase, as in the objective plot. Afterwards, many oscillations are noticed, indicating that the optimizer constantly modifies the geometry in order to maximize the eigenfrequencies while taking into account the volume fraction and stresses. The volume constraint is evaluated such that:

$$\frac{V}{V_0} - \epsilon_{vf} = -0.004 \quad with \quad \epsilon = 0.1 \Rightarrow \frac{V}{V_0} = 0.096 \tag{5.8}$$

and since the volume ratio is lower than 0.1, the constraint is satisfied.

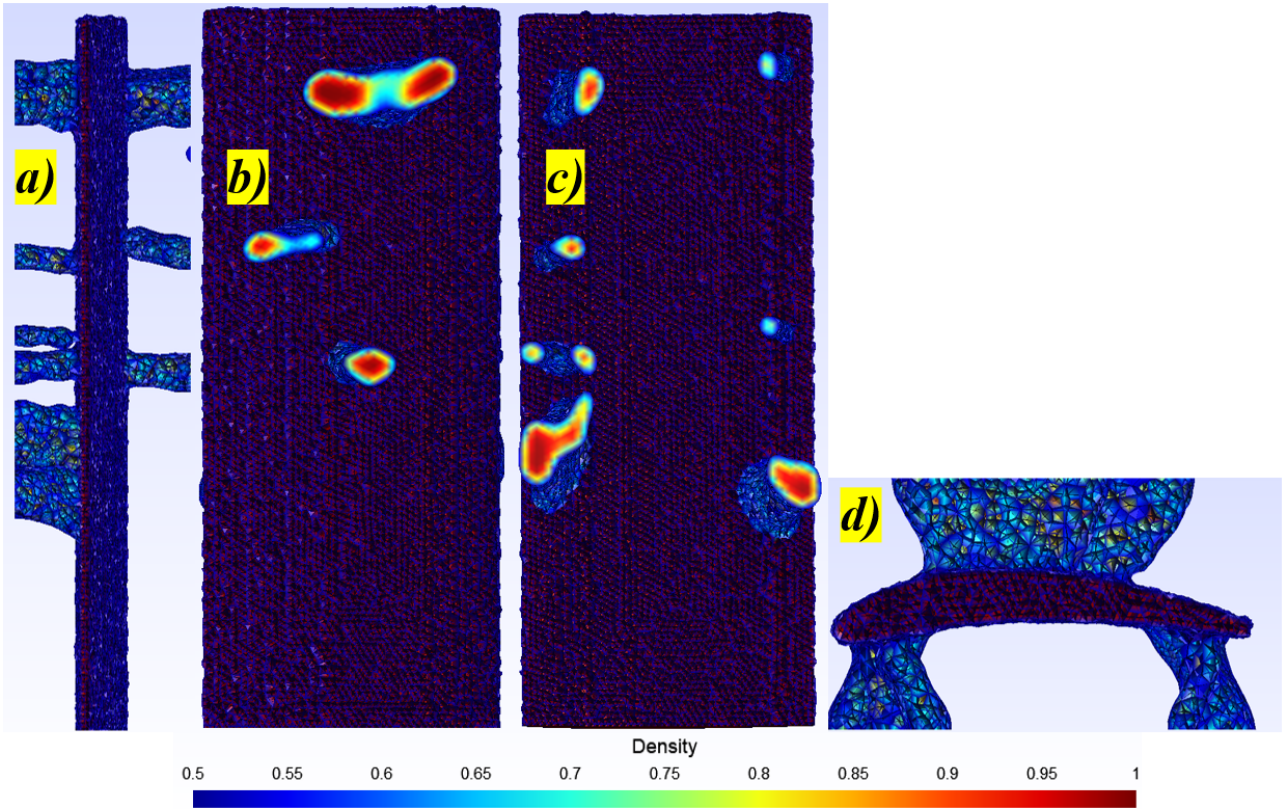


Figure 5.10: $3D$ density based topology optimization result (objective: maximize the first three eigenfrequencies, constraint: retain 10 % of the initial volume, stresses should be below an allowable value $\sigma_{allowable} = 32.5\,MPa$) - a) front view, b) lateral view 1, c) lateral view 2, d) top view with [0.5, 1] retained densities.

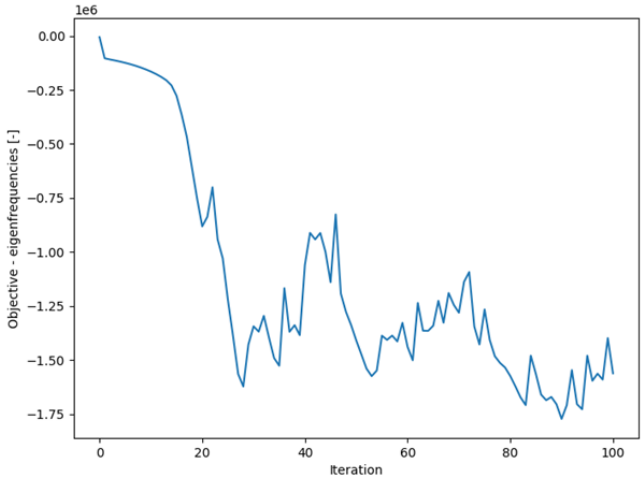


Figure 5.11: $3D$ density based optimization - maximizing eigenfrequencies objective evolution with respect to the iterations - case 2.1

Furthermore, the objective and volume evolution graphs present a smoother behavior than in the first $3D$ optimization. This can be justified by the fact that, in the eigenfrequencies maximization with volume constraint, many possible layouts with similar objective values could be identified. By imposing the distributed force around the blade, the number of possibilities was reduced. Therefore, in order to keep the stresses below the $32.5\,MPa$ imposed value, fewer feasible solutions were available and in this way, the evolution was highly affected, resulting in a more controlled progression.

Comparable to the second case presented in the $2D$ section, the stress constraint presented in fig. 5.12 is active only for the first iteration and then it remains zero for the rest of the process. More precisely, the material redistribution that was performed during the iterations maintained a feasible design while maximizing the first three eigenfrequencies. Because one of the objectives is to show that the stress constraint can be reduced, the next optimization drastically lowers the stress limit such that a larger contribution of the constraint is forced during the optimization.

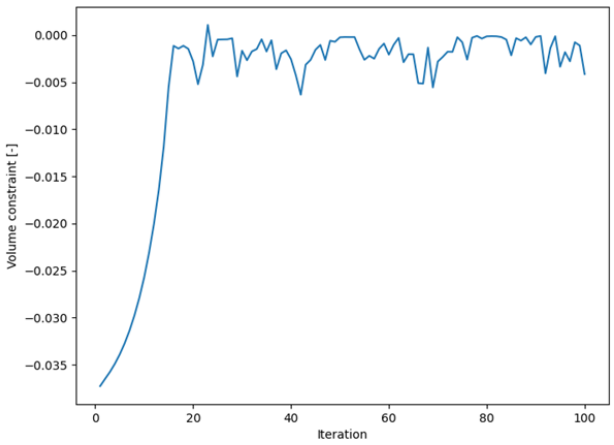


Figure 5.12: $3D$ density based optimization - volume constraint evolution with respect to the iterations - case 2.1

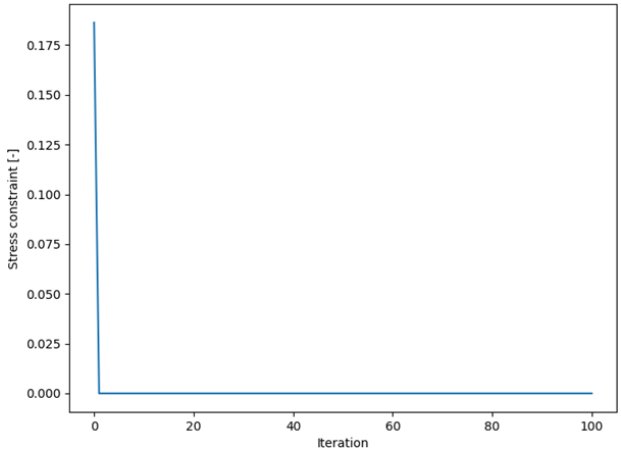


Figure 5.13: $3D$ density based optimization - stress constraint evolution with respect to the iterations - case 2.1

The eigenfrequencies evolution is presented in fig. 5.14, along with the obtained values shown in tab. 5.2. In the first 30 iterations, a smooth increase is observed and when the supports begun to form, oscillations appeared. This emphasizes that the eigenfrequencies remain very sensitive to any local material distribution since small changes in topology modify the stiffness and mass, causing these types of fluctuations. At the final iteration, the three natural frequencies reached $2,034\,rad/s$, $2,225\,rad/s$ and $2,253\,rad/s$, respectively.

	$f_1[rad/s]$	$f_2[rad/s]$	$f_3[rad/s]$
Iter. 0	20.1	45.7	59.9
Iter. 100	2,034.4	2,225.6	2,253.1

Table 5.2: Natural frequencies - case 2.1

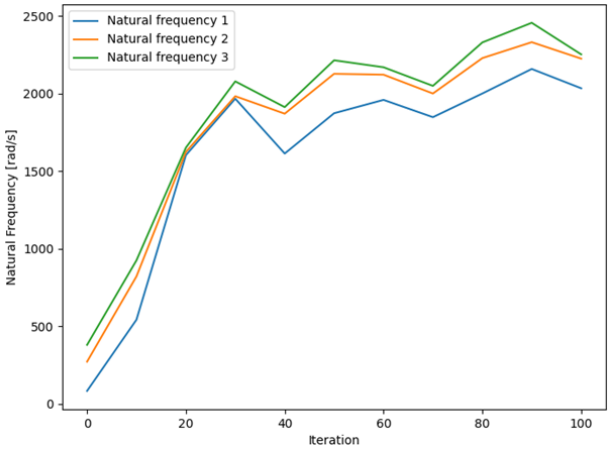


Figure 5.14: $3D$ density based optimization - first three natural frequencies evolution with respect to the iterations - case 2.1

The stress comparison between iteration 0 and 100 is presented in fig. 5.15. Similar to the two-dimensional case, the distributed force was applied on both pressure and suction side and the corresponding stress constraint was active only for one iteration. This indicates that higher stress values were obtained inside the surrounding domain due to the density initialization. Because there is a reduced amount of material available, the stiffness is low and the forces produce higher localized stresses. By associating higher densities in the critical regions, the stress constraint is rapidly satisfied. At iteration 0, the cantilevered blade experiences higher stresses near the root ($\sigma = 1.6\,MPa < \sigma_{allowable} = 32.5\,MPa$), where the maximum bending moment occurs. The imposed load is not producing large deformations on the blade and therefore, the stresses within the structure are reduced. This indicates that the design evolution was mainly driven by the maximization objective with respect to the volume constraint. At iteration 100, the maximum stress value obtained is equal to $\sigma = 0.18\,MPa$ and it is located near the supports. The stresses are reduced and the stress constraint is satisfied.

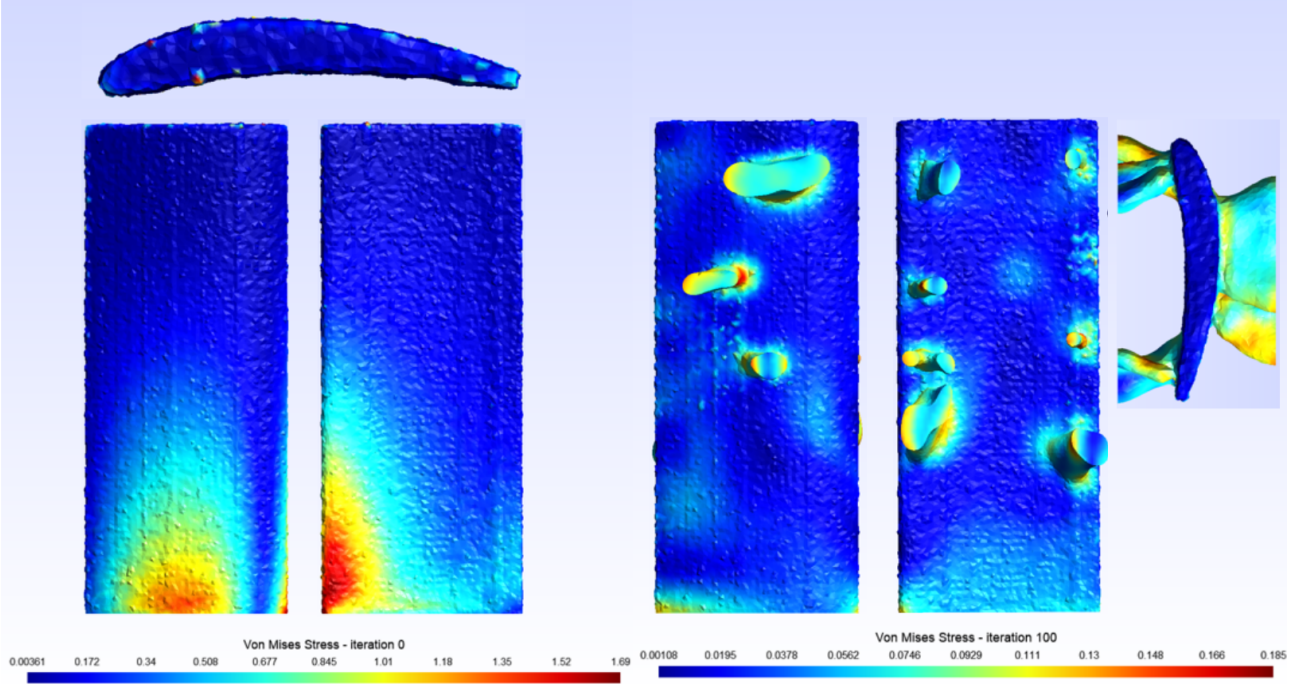


Figure 5.15: $3D$ density based optimization - comparison between stress fields at iteration 0 and 100 - case 2.1

For the current case, the displacement comparison between iteration 0 and 100 presented in fig. 5.16 is extracted when the distributed force is applied. At the initial iteration, the maximum displacement is located at the top free part, while a gradual decrease is observed when approaching the clamped root. During the optimization, the multiple created supports clamped the blade surface to the domain walls, creating stiffer load transfer paths that suppress the motion of the blade. Therefore, at iteration 100, the displacement is reduced and it appears to be negligible in this visualization scheme used in ParaViS, suggesting an increase in stiffness.

Finally, because the objective was set to maximize the first three eigenfrequencies, the mode shapes at iteration 100 were extracted and presented in fig. 5.17, retaining only the densities between [0.5, 1]. The initial mode shapes are presented in fig. 3.3, where the first and third modes were dominated by bending, while the second one was dominated by torsional motion.

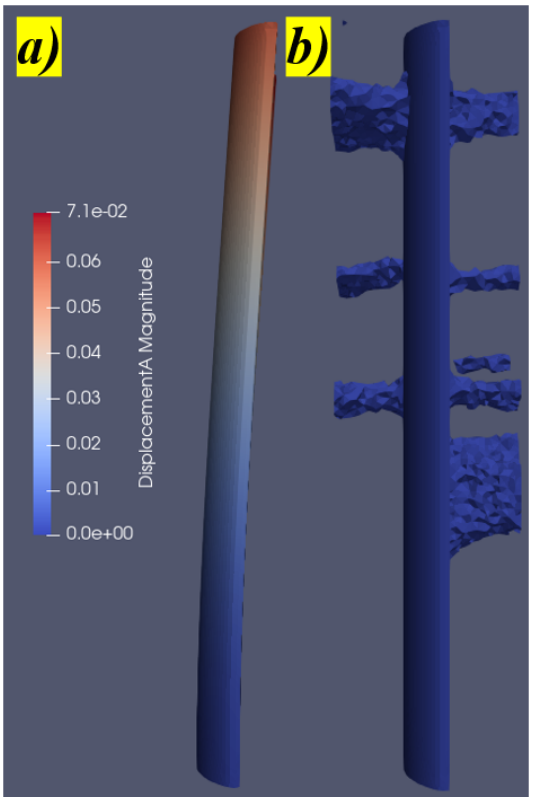


Figure 5.16: $3D$ density based optimization - comparison between displacement at (a) iteration 0 and (b) iteration 100 - case 2.1

At iteration 100, the first mode shape displays local bending effects in the several free regions, where there are no supports. The second one is concentrated in a specific region from the bottom part, illustrating a localized bending mode, while the third one is similar to the mode extracted at iteration 0. Therefore, the lower region of the blade that is not clamped by the created supports displays a strong bending deformation, while the upper part that is fixed presents a lower displacement magnitude.

5.3.3 Reduced allowable stress

In order to show that the stresses can be reduced, a value equal to $0.3\,MPa$ is imposed. The aim of this drastic reduction is to observe the geometrical changes when the stress constraint is active for more iterations. The problem formulation is described by the equation (4.14) used as well to describe the $2D$ corresponding case.

In the previous optimization, when the allowable maximum value was set to $32.5\,MPa$, the stress constraint was active for one iteration, indicating a small influence on the final design. Additionally, in the same optimization, the maximum stress value obtained at iteration 100 was equal to $0.52\,MPa$, while in the current case, the maximum limit is set to an even lower value, $\sigma_{allowable} = 0.3\,MPa$. This forces the optimizer to create a geometry that is capable to maintain lower maximum values, being more restricted and evaluating if the optimizer is capable to reduce the stress level even more. Using this formulation, critical load paths can be identified and the placement of the supports may be influenced in order to maintain this low limit.

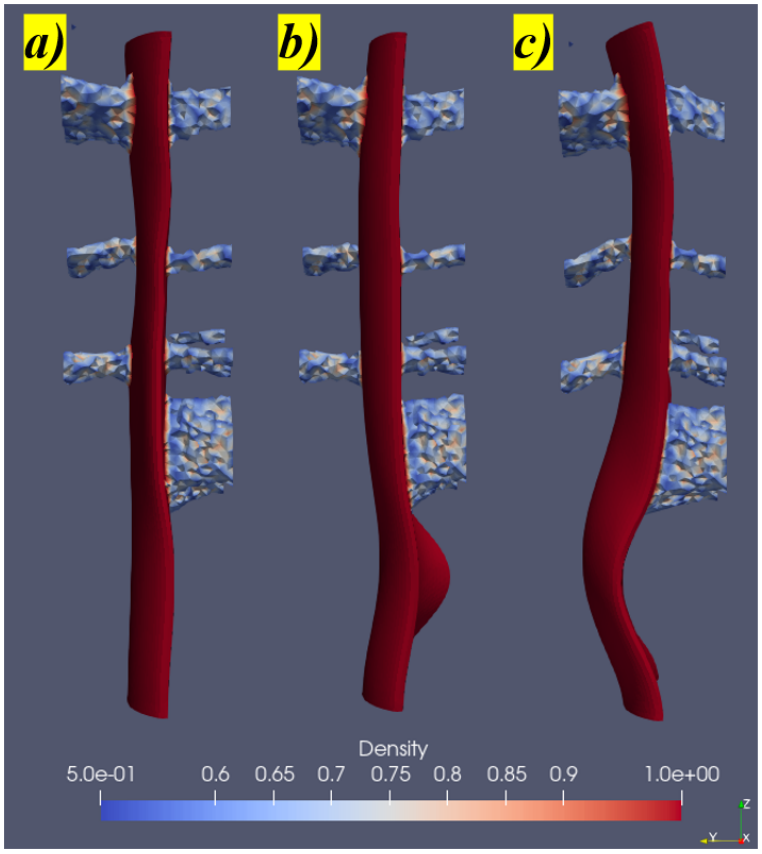


Figure 5.17: First three mode shapes of the obtained geometry with [0.5, 1] retained - case 2.1

Since the allowable maximum stress is reduced, the optimizer is expected to add more material in highly stress regions and even to create thicker supports or redistribute them in order to ensure a better performance.

The obtained results were are shown in fig. 5.18 and for visualization, the densities between [0.5, 1] are retained. On the suction side presented in (b), three created supports are identified. The main one displays a more robust shape, along with two slender supports, one placed mid-span and one at the top leading edge part. On the pressure side illustrated in c), several supports are created and compared to the previous cases, the placement is similar. Four robust supports were added to sustain the blade on the leading and trailing edge, while additional thinner supports are placed in order to reduce the local effects.

Therefore, the current geometry presents a more balanced distribution of supports on both sides. The material is mainly placed in the top and middle region, where the higher stress concentrations appear, while additional load paths are created at the extremities, where the modal deformation could be more pronounced. Since the objective was to maximize the first three eigenfrequencies, the bending and torsion deformation should be reduced. The top part is highly affected by the bending and the created supports are responsible for reducing the deformations, while the middle is enforced by several robust supports that are able to suppress torsional effects.

The corresponding evolutions are presented in figs. 5.19, 5.20 and 5.21. Compared to the previous cases where the optimization was performed for 100 iterations, in the current case, the process was conducted for 130 iterations due to the drastic stress limit. Therefore, a more

refined material redistribution was needed in order to achieve the objective while satisfying both volume and stress constraint.

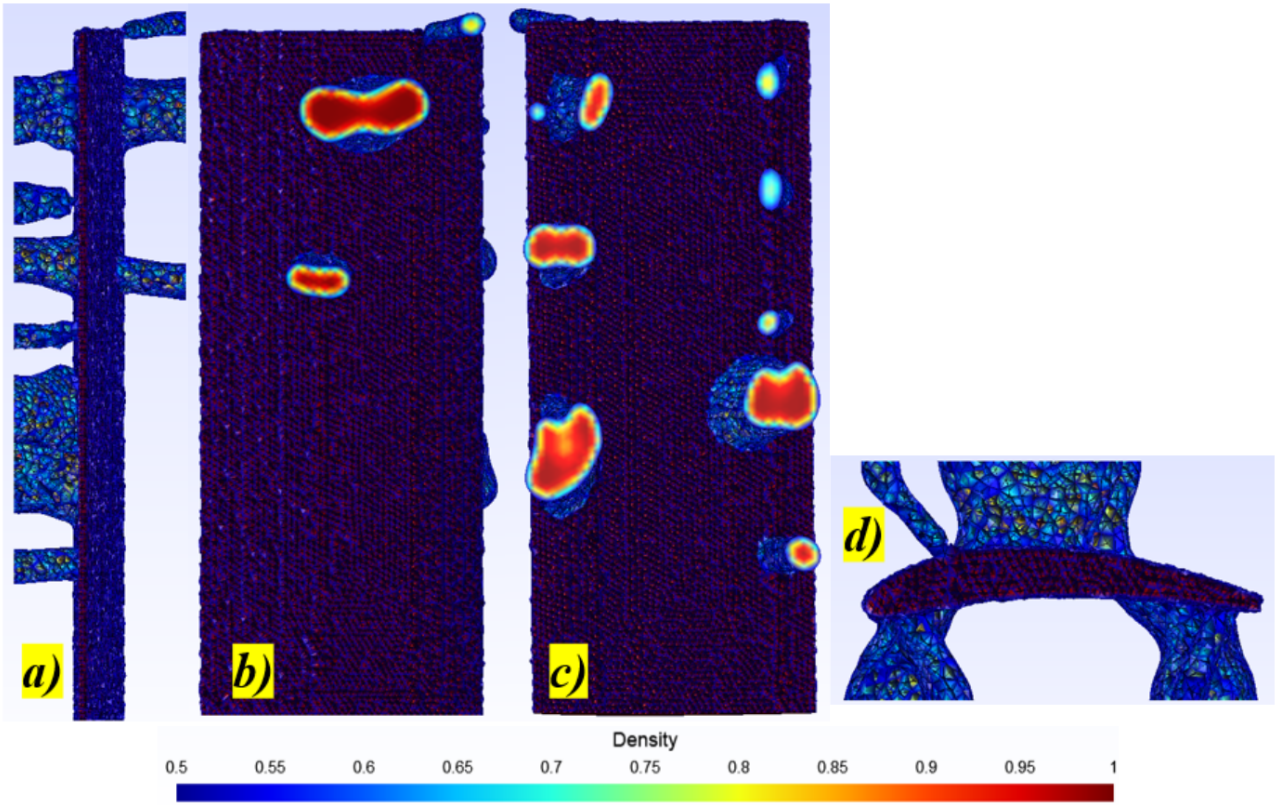


Figure 5.18: $3D$ density based topology optimization result (objective: maximize the first three eigenfrequencies, constraint: retain 10 % of the initial volume, stresses should be below an allowable value $\sigma_{allowable} = 0.3\,MPa$) - a) front view, b) lateral view 1, c) lateral view 2, d) top view with [0.5, 1] retained densities.

The objective evolution is displayed in fig. 5.19. A more oscillatory behavior is observed, compared to the previous case where the $\sigma_{allowable}$ was set to $32.5\,MPa$. The lower maximum value restricts the material redistribution, increasing the conflict between the objective and the constraints and indicating repeated trade-offs performed in order to find a solution for the problem.

For the volume constraint presented in fig. 5.20, a similar trend is observed. Several bounded oscillation appear, indicating that the optimizer is constantly modifying the material distribution. The local effects become more pronounced and therefore, more isolated features appear, highly influencing the evolution of the function. The constraint is evaluated such that:

$$\frac{V}{V_0} - \epsilon_{vf} = -0.002 \quad with \quad \epsilon = 0.1 \Rightarrow \frac{V}{V_0} = 0.098 \tag{5.9}$$

and since the $V/V_0 < 0.1$, the constraint is considered satisfied.

The stress constraint is also presented in fig. 5.21. Similar to the $2D$ case, the objective of this optimization was to study the effects of reducing the allowable stress limit. With the current setup, the stress constraint is active through the optimization, while in the two-dimensional case, it was active for 50 iterations. This emphasizes the fact that the stress state

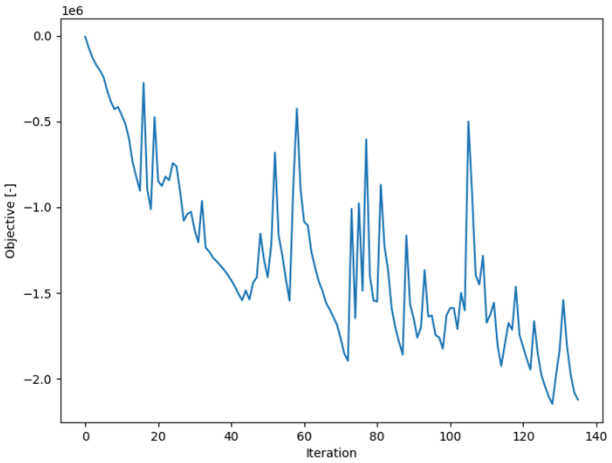


Figure 5.19: $3D$ density based optimization - maximizing eigenfrequencies objective evolution with respect to the iterations - case 2.2

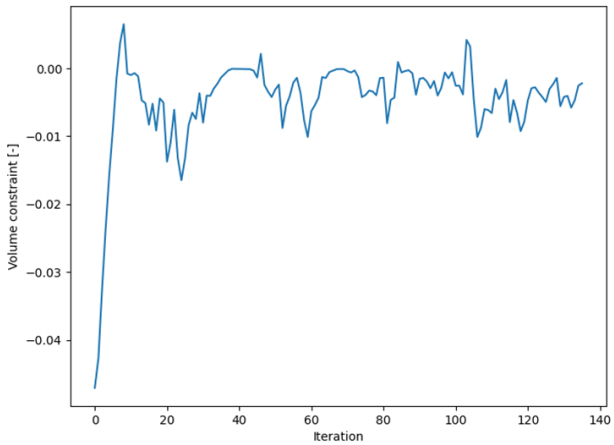


Figure 5.20: $3D$ density based optimization - volume constraint evolution with respect to the iterations - case 2.2

is more complex and since a larger design space offers several feasible solutions to explore, an increased the number of iterations is required. The stress is a local quantity and once the global configuration is mostly determined, the following iterations could focus on local stress concentrations determined in specific locations.

The corresponding diagram displays a rapid improvement in the first iterations. The values are drastically reduced to 0.1 and between iteration 20 and 100, a gradual decrease with small bounded oscillations is observed. Afterwards, the value decreases to 0.03 until it reaches a plateau.

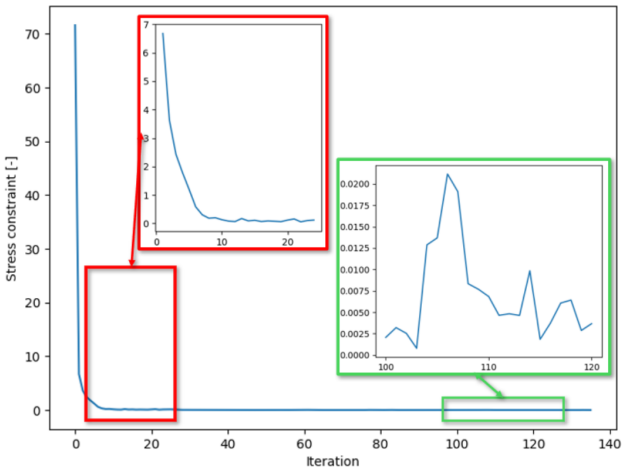


Figure 5.21: $3D$ density based optimization - stress constraint evolution with respect to the iterations - case 2.2

The natural frequencies evolution displayed in fig. 5.22, along with the corresponding values in tab. 5.3 that presents lower values at the last iteration, illustrating the fact that the optimization was more restricted than in the previous cases. Since it must redistribute the material strategically in order to reduce stress concentrations, part of the material is allocated to increase local stiffness rather than providing a larger maximization for the eigenfrequencies.

In the initial stages, rapid improvements are observed, while in the middle part of the process, more oscillations are identified. This suggests that the design was not fully satisfying the imposed constraints and therefore, more adjustments were needed. Additionally, a constant trade-off between dynamic performances and stress attenuation is revealed.

	$f_1[rad/s]$	$f_2[rad/s]$	$f_3[rad/s]$
Iter. 0	20.1	45.7	59.9
Iter. 100	1,956.5	2,256.1	2,287.5

Table 5.3: Natural frequencies - case 2.2

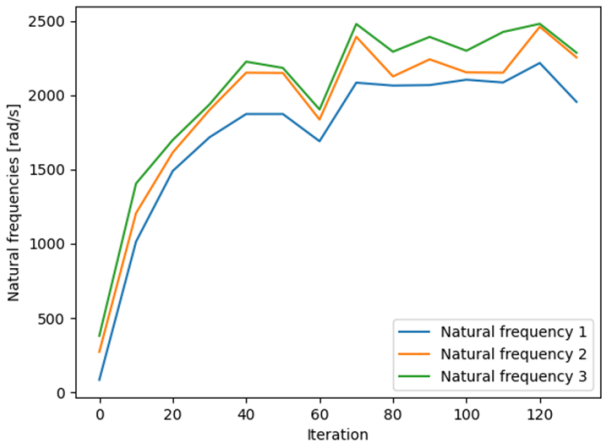


Figure 5.22: $3D$ density based optimization - first three natural frequencies evolution with respect to the iterations - case 2.2

The comparison between iteration 0 and 130 illustrated in fig. 5.23 presents a similar stress reduction to the one discussed in the previous case. At iteration 0, a maximum stress $\sigma = 1.6\,MPa$ is obtained near the root, which is higher than the allowable imposed, $\sigma_{allowable} = 0.3\,MPa$. Therefore, the optimizer adds supports in the critical regions in order to create a stiffer structure that exhibits lower stresses and a maximum of $0.14\,MPa$ is obtained in the final configuration. The stress constraint was active for the whole process, indicating a higher influence on the final geometry, where more robust supports were created and distributed in critical regions.

The displacement comparison is presented in fig. 5.24. Compared to the iteration 0 where the clamped blade experienced larger displacements at the free top region, in iteration 130, the blade is clamped using the created supports, suppressing the structural deformation and indicating an increase in stiffness. The suction side is connected to the clamped walls in the top region, whereas the pressure side presents several supports distributed in order to improve the rigidity of the structure. The discontinuity of the top support in the ParaViS visualization is considered an artifact, while in the Gmsh software, the member appears to be connect to the structure. In both cases, the [0.5, 1] densities were retained.

Lastly, fig. 5.25 illustrates the mode shapes at the final iteration. As a comparison, the initial mode shapes are presented in fig. 3.3, where mode 1 and 3 are dominated by the bending motion, while mode 2 is represented by torsion. This comparison reveals that the structure became dynamically stiffer. The initial deformation patterns are suppressed and local effects are identified. Therefore, for all three modes at iteration 130, a bending tendency is observed in the lower part where only one support was added. In the previous optimization case, where the lower part was fully free, a similar bending deformation was observed, whereas in the current case, it is more localized due to the formed support, suggesting that the current structure has a higher localized stiffness.

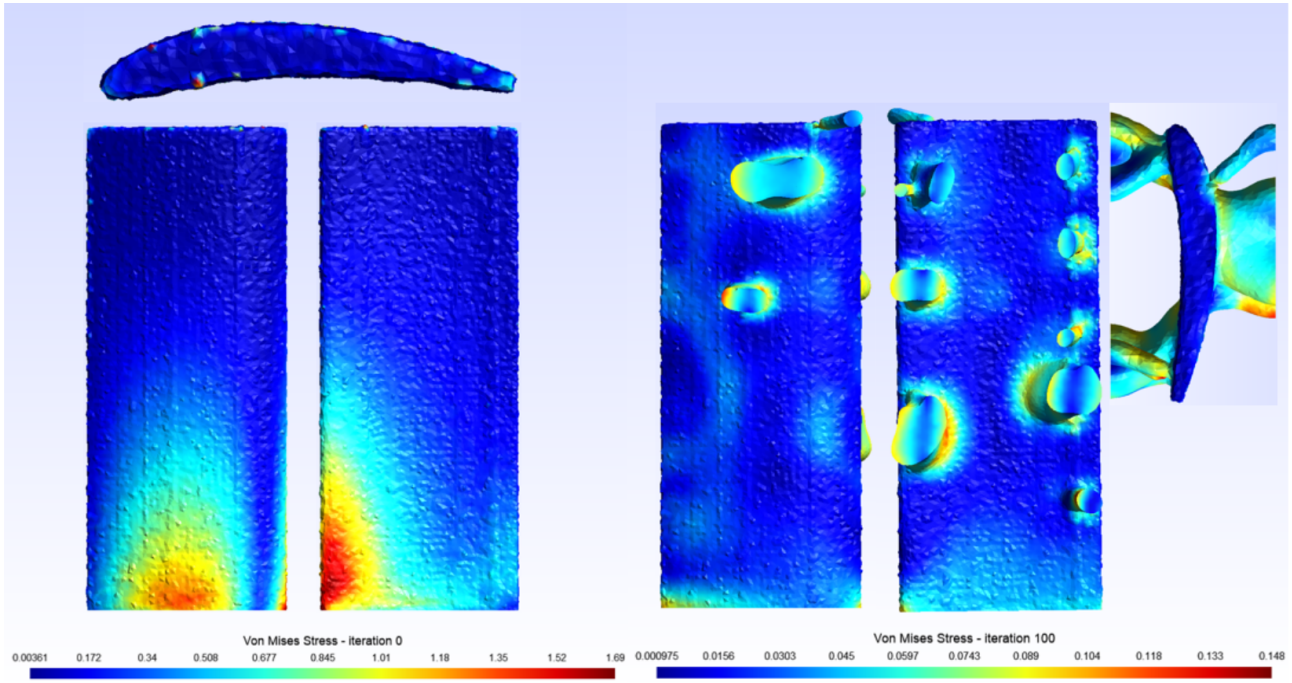


Figure 5.23: $3D$ density based optimization - comparison between stress fields at iteration 0 and 130 - case 2.2

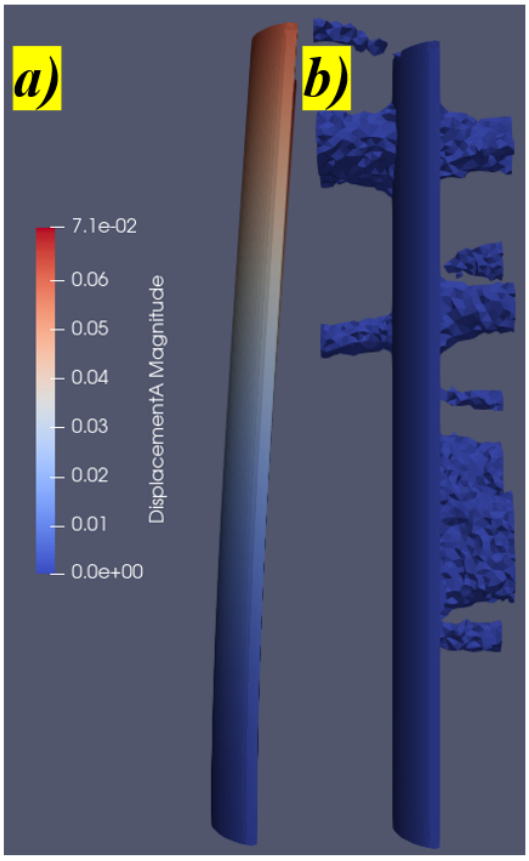


Figure 5.24: $3D$ density based optimization - comparison between displacement at (a) iteration 0 and (b) iteration 100 - case 2.2

Overall, by reducing the allowable stress, a more robust geometry is obtained, with well-defined supports in critical regions. More iterations were needed in order to satisfy the stress constraint which was active during the full process, suggesting that its influence is more con-

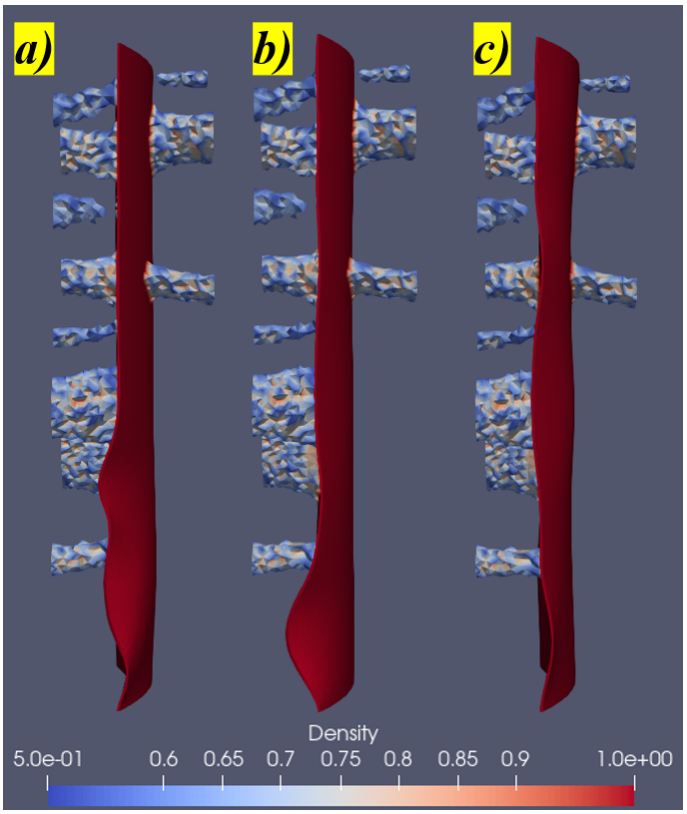


Figure 5.25: First three mode shapes of the obtained geometry with [0.5, 1] retained - case 2.2

siderable compared to the previous case.

5.4 Eigenfrequency maximization under multiple loads with volume and stress constraints

Previously, a distributed load was applied on both sides of the blade and the resulted geometries were analyzed, while in the current case, the loading conditions described in section 5.1.1 are applied in order to represent a realistic framework and to capture local effects, similar to the fourth $2D$ case.

5.4.1 Problem formulation

Using the aerodynamic pressure obtained at the blade interface, a realistic representation of the load was extracted and projected on the structural mesh used in the $3D$ optimization. This multiple-loads case is able to capture local three-dimensional effects, considering the actual spatial variation of the CFD pressure and predicting realistic displacements caused by bending. The obtained result is analyzed and compared to the previous cases that used distributed forces, in order to verify if the applied load was capable of reproducing realistic effects.

The problem formulation is described by equation (4.15), where the objective is represented by the first three eigenfrequencies maximization, while a 10 % volume fraction is applied, along with an additional constraint that ensures that the stresses remain below the prescribed value $\sigma_{allowable} = 32.5\,MPa$. The optimization procedure and the parameters are retained. For the current case, the scaling parameters are using the default values, presented in tab. 4.8.

5.4.2 Results and discussion

The result presented in fig. 5.26 displays the final configuration. A similar locations of the supports is observed, but their thicknesses vary. On the pressure side, higher loads are identified along with multiple local effects, while on the suction side, a uniform load distribution is observed, with lower values towards the trailing edge, as it was shown in fig. 5.3. On both sides, lower forces are identified near the clamped face of the blade.

It is observed that the overall tendency in all presented cases is to create two main supports on the suction side, along with thinner supports on the pressure side, distributed along the extremities of the blade. Therefore, on the suction side presented in fig. 5.26 (b), two thick supporting members are created, along with a slender one in the lower part of the blade. Since a more uniform load covers most of the surface, an efficient load transfer is created using fewer robust members. On the pressure side presented in fig. 5.26 (c), eight slender supports are equally distributed along the extremities. On that side, the blade experiences the highest local load, along with multiple variations and due to these effects, the reinforcement was done through multiple supports placed in the critical regions.

With the objective set to maximize the first three eigenfrequencies, the global stiffness is increased by providing additional support to the regions that are contributing to the chosen modes. Additionally, these modifications are performed while the stress field is constantly evaluated, ensuring that the obtained values are below $32.5\,MPa$ limit. Consequently, the created connections suppress part of the local modal deformation, while ensuring that the structure can withstand the prescribed loads. For visualization, the range [0.5, 1] is selected for the density and it can be observed that pressure side supports are mostly formed out of lower densities, while the opposite supports display densities in the $0.8-0.9$ range. One disconnected support is present and since it has negligible contribution to the structural response, it is interpreted as a numerical artifact.

The objective evolution with respect to the iterations is presented in fig. 5.27. In the first 30 iterations, a relatively smooth decrease is observed, suggesting a stable material distribution. Once the main load paths are created, local refinements are needed in order to fully satisfy the constraints, creating oscillations is the objective evolution.

The volume constraint evolution is presented in fig. 5.28. Similar to the objective function behavior, in the first 20 iterations, a gradual increase is observed. Afterwards, local refinements are needed to be performed on the defined geometry in order to satisfy the volume constraint. Because of the restrictive amount of material, every modification on the distribution may cause oscillations since it directly affects the structural stiffness. The volume constraint is evaluated such as:

$$\frac{V}{V_0} - \epsilon_{vf} = -0.0002 \quad with \quad \epsilon = 0.1 \Rightarrow \frac{V}{V_0} = 0.099 \tag{5.10}$$

and since the $V/V_0 < 0.1$, the constraint is considered satisfied.

The stress constraint is presented in fig. 5.29 and it is active only for 2 iterations. This emphasizes that at the beginning of the process, there is not enough material in the regions where the loads are carried, while in the next few iterations, higher densities are attributed to these regions, improving the local stiffness. Therefore, the stress constraint is immediately

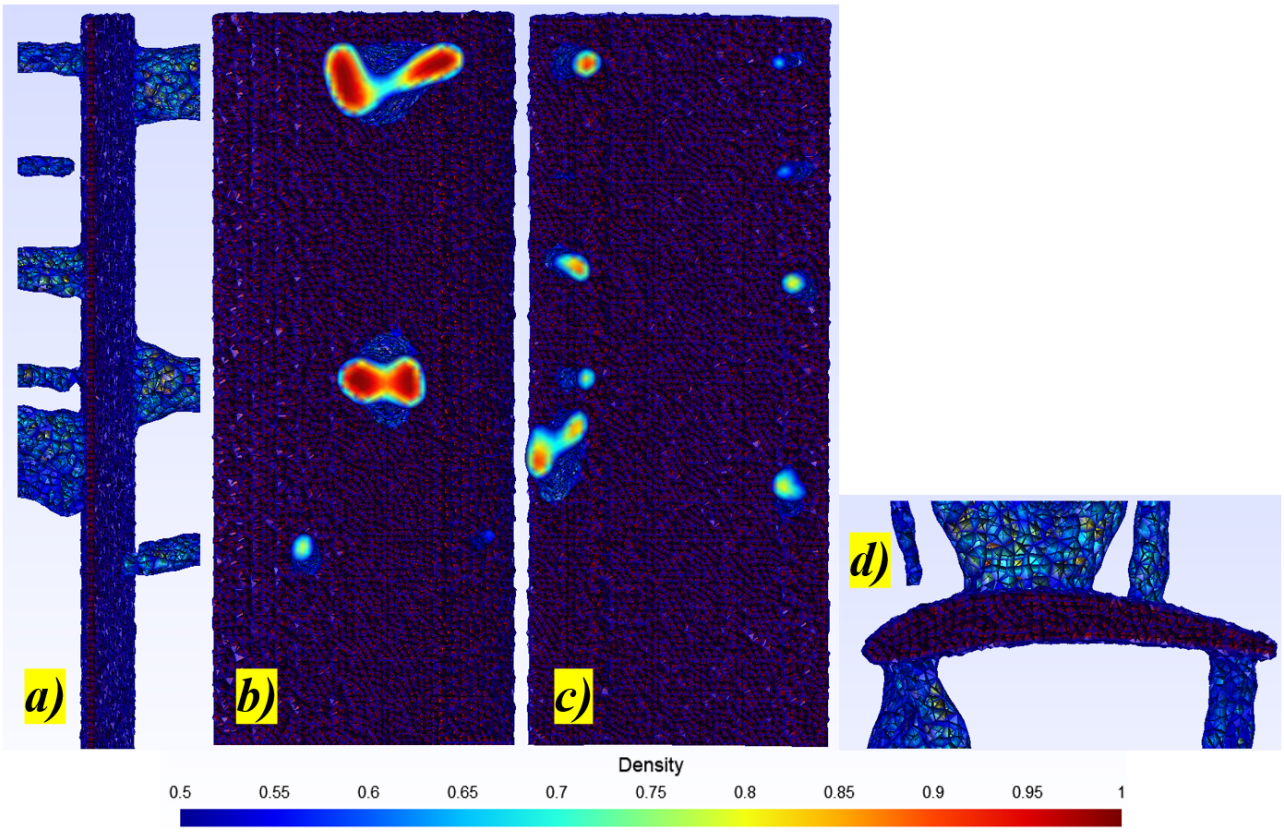


Figure 5.26: $3D$ density based topology optimization result with multiple load applied (objective: maximize the first three eigenfrequencies, constraint: retain 10 % of the initial volume, stresses should be below an allowable value $\sigma_{allowable} = 32.5\,MPa$) - a) front view, b) lateral view 1, c) lateral view 2, d) top view with [0.5, 1] retained densities.

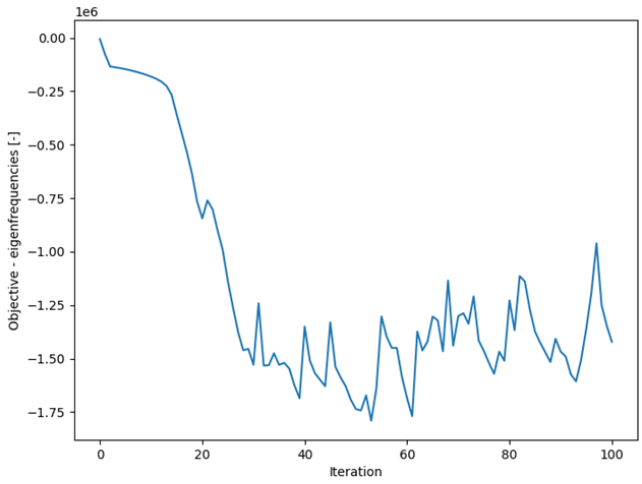


Figure 5.27: $3D$ density based optimization - maximizing eigenfrequencies objective evolution with respect to the iterations - case 4

satisfied and the optimizer is mainly driven by the eigenfrequencies maximization with respect to the volume constraint.

The evolution of the natural frequencies is presented in fig. 5.30, along with the corresponding values at iteration 0 and 100 shown in tab. 5.4. Until iteration 30, a gradual increase is observed, similar to the volume and objective trends. Afterwards, the local redistribution affects the

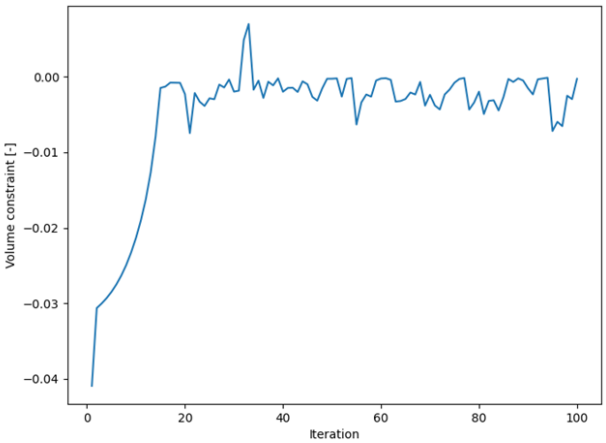


Figure 5.28: $3D$ density based optimization - volume constraint evolution with respect to the iterations - case 3

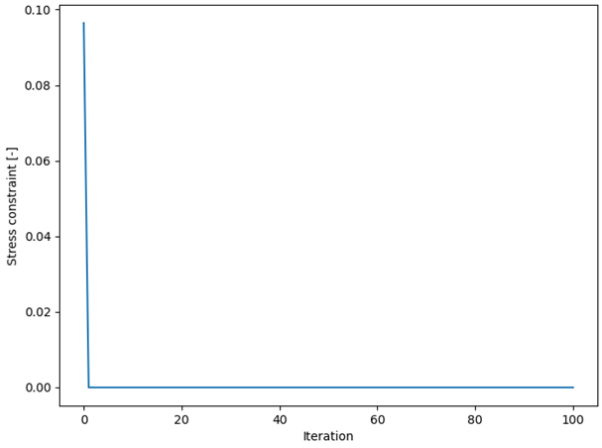


Figure 5.29: $3D$ density based optimization - stress constraint evolution with respect to the iterations - case 3

dynamic response of the structure and consequently, the eigenfrequencies are impacted. At iteration 100, the first natural frequency reaches $1,892\,rad/s$, while the second and third ones reaches $2,155\,rad/s$ and $2,187\,rad/s$, respectively.

	$f_1[rad/s]$	$f_2[rad/s]$	$f_3[rad/s]$
Iter. 0	20.1	45.7	59.9
Iter. 100	1,892.3	2,155.9	2,187.8

Table 5.4: Natural frequencies - case 3

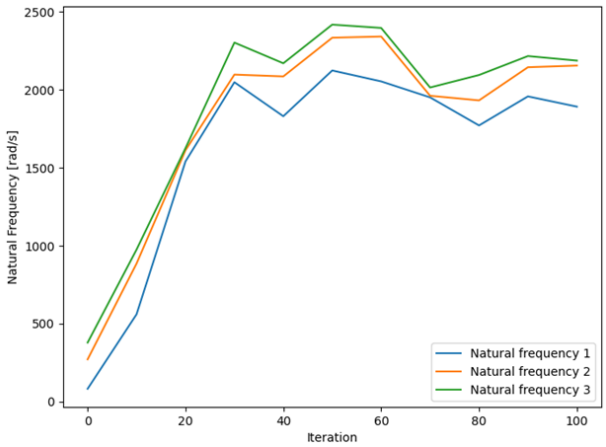


Figure 5.30: $3D$ density based optimization - first three natural frequencies evolution with respect to the iterations - case 3

The observed trends in the convergence indicate that the final geometry is mainly influenced by the balance between the eigenfrequencies maximization and the volume restriction, while the stress constraint is satisfied in the first iterations. The stress fields are extracted and the comparison is presented in fig. 5.31. Higher stresses equal to $\sigma = 2.2\,MPa$ are obtained near the clamping face, while the rest of the blade experiences relatively low values. With the realistic loading case, the imposed allowable limit is set to $32.5\,MPa$ and the stress constraint is active for only one iteration. This empathizes that higher stresses are found in the domain, where the densities are set to almost zero values. At iteration 100, several supports are created and the maximum obtained stress is equal to $0.7\,MPa$.

The deformation comparison between iteration 0 and iteration 100 is presented in fig. 5.32. At iteration 0, a localized deformation pattern is observed in the upper trailing edge region,

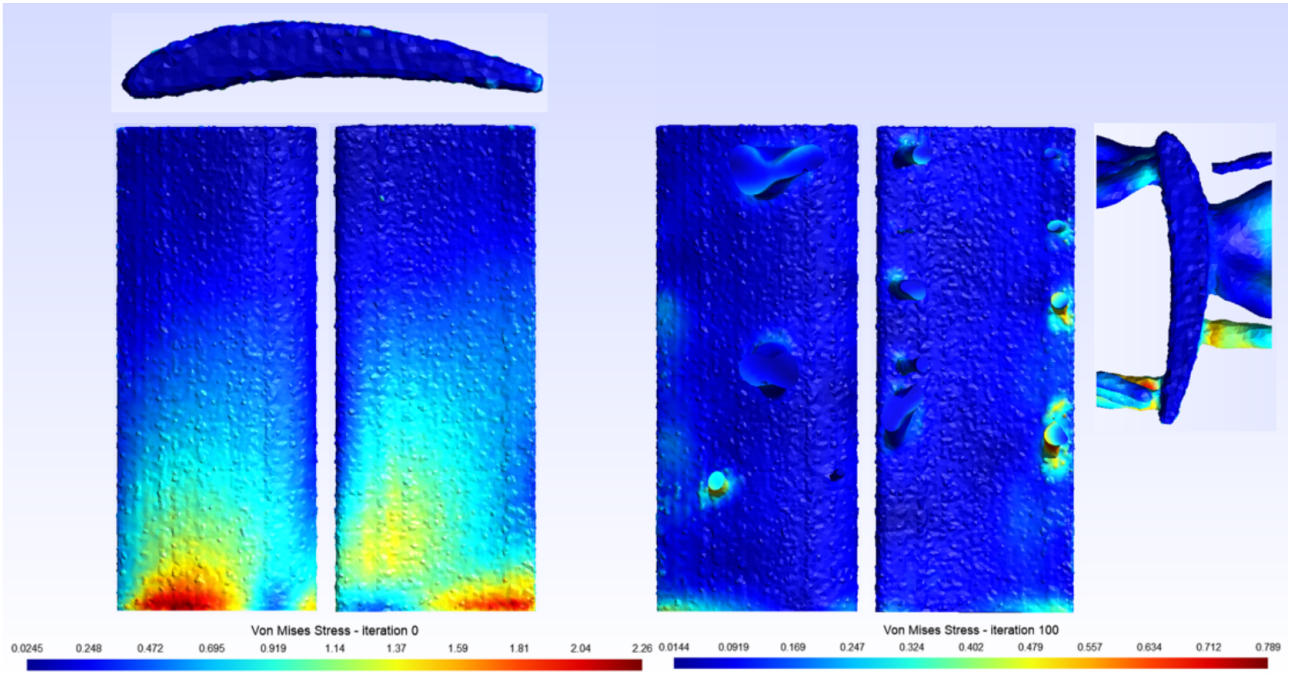


Figure 5.31: 3D density based optimization - comparison between stress fields at (a) iteration 0 and (b) iteration 130 - case 3

while in the previous case presented in fig. 5.24, when the distributed load was applied, the deformation pattern was relatively uniform distributed in the upper part. Since local effects are captured with higher fidelity, this result is consistent with the realistic loading. In contrast, at iteration 100, two localized deformation points are observed, indicating that the displacement is not drastically reduced as in the previous cases.

In the region where higher displacement is observed, multiple thin supports are created and therefore, only a limited reduction in deformation is observed. However, the magnitudes are also low and the optimizer does not have to eliminate all deformations. The thin supports may provide a significant increase in local stiffness and the additional material is concentrated in more critical areas that can highly contribute to the eigenfrequencies increase.

The final mode shapes are extracted and presented in fig. 5.33. As noted previously, at iteration 0, mode 1 and 3 are dominated by bending, while the second one is dominated by torsion. In the current case, local free regions are deformed as it can be observed for the first two modes. The initial deformation pattern was suppressed since the blade is attached by robust supports in the upper and middle part on the suction side. For the mode 3, a bending deformation is observed in the lower part of the blade, close to the clamping. Because there is only one support added, the corresponding region undergoes greater deformations, offering less resistance to bending.

Overall, by applying multiple loads on the blade surface, local effects are captured. More robust supports are connecting the suction side to the clamped walls, creating more resistance to the bending and torsion deformation observed in the three mode shapes, while thinner supports are added on the opposite side. In comparison with the distributed force case, the stresses and deformations at iteration 0 are lower in the current case, suggesting that the distributed force is more conservative, predicting a more severe structural response.

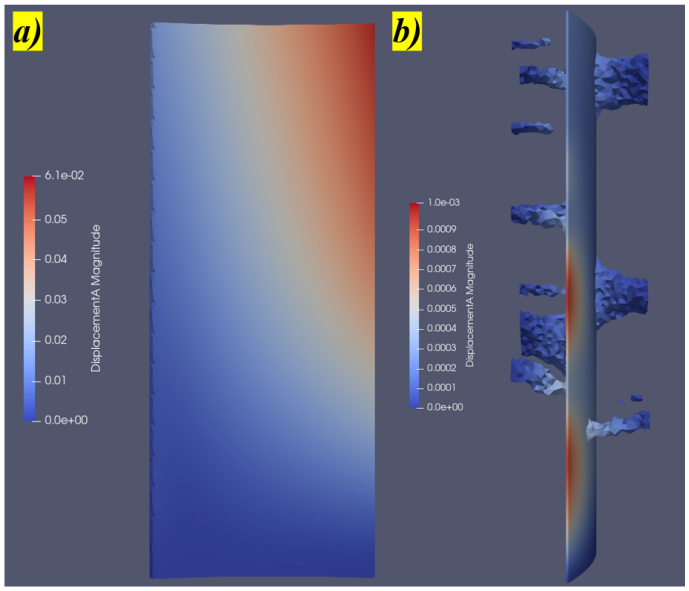


Figure 5.32: $3D$ density based optimization - comparison between displacement at (a) iteration 0 and (b) 100 - case 3

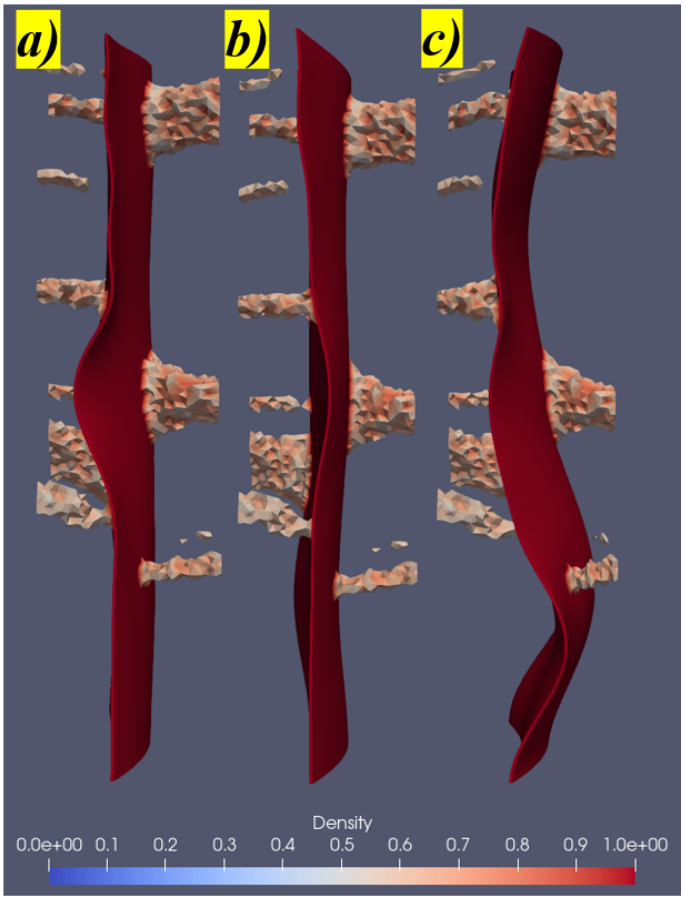


Figure 5.33: First three mode shapes of the obtained geometry with [0.5, 1] retained - case 3

5.5 Comparison of the three-dimensional optimization cases

A geometry comparison between the three-dimensional cases is presented in fig 5.34. Using Gmsh, a density threshold of 0.8 is applied, in order to suppress low density regions and to

reveal main structural members, facilitating a more direct comparison of the results.

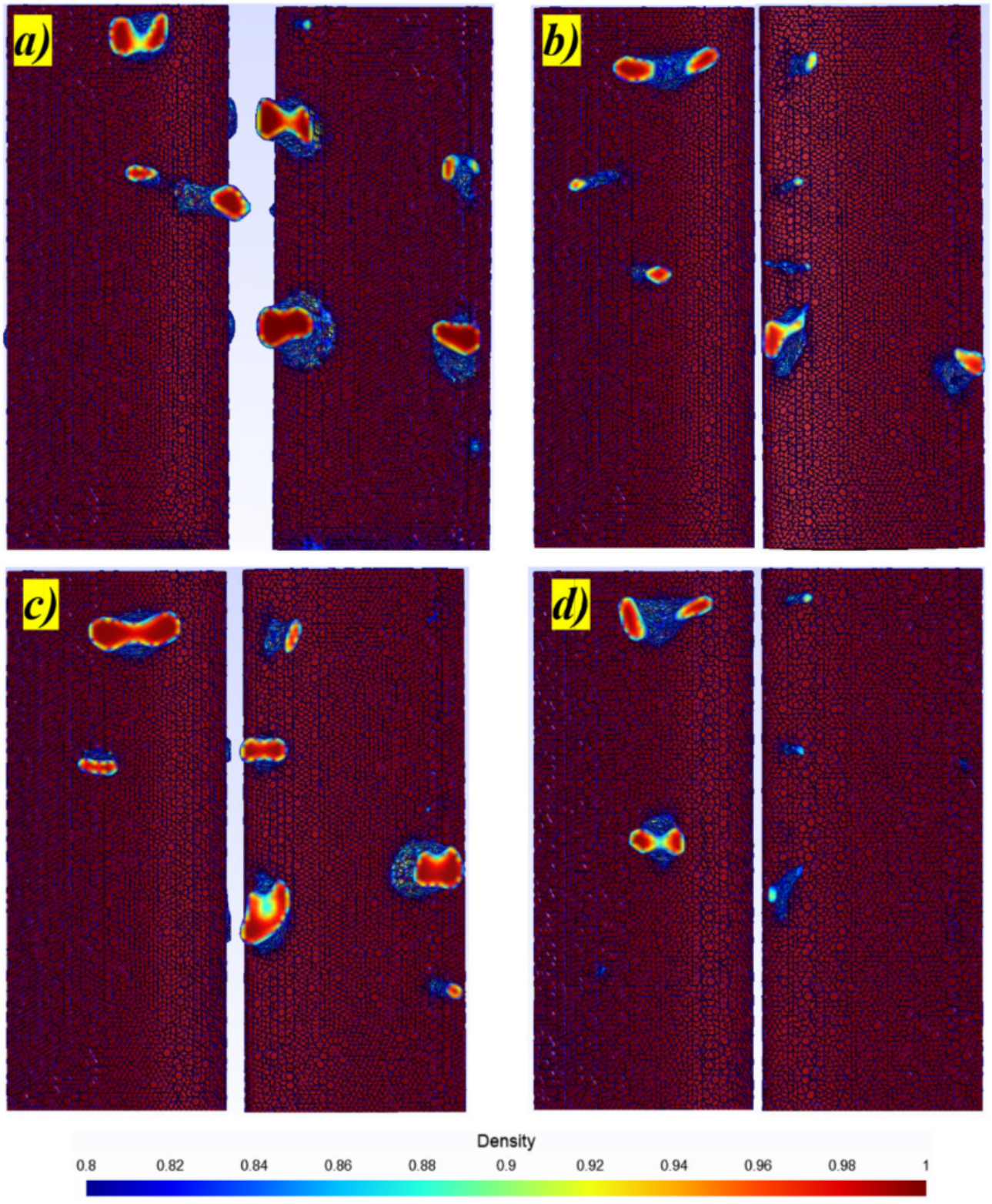


Figure 5.34: $3D$ density based optimizations - comparison between *a)* (eigenfrequency maximization and volume constraint), *b)* (addition of the stress constraint - $\sigma_{allowable} = 32.5\,MPa$), *c)* (reduced allowable stress - $\sigma_{allowable} = 0.3\,MPa$) and *d)* (multiple-load - $\sigma_{allowable} = 32.5\,MPa$)

The maximization of the first three eigenfrequencies was set as an objective, while a fraction of 10 % of the surrounding domain volume should have been retained in order to create multiple thin connections that can allow the flow to pass around the blade. Therefore, the optimizer redistributed material in the optimizable domain in order to increase the global stiffness. For the first and third mode, the flexibility associated with bending is reduced, whereas for the second mode, the twisting stiffness is increased. The baseline formulation was applied in case (a), while in the other three cases, a stress constraint is introduced.

Similar load paths are identified in all four cases. The optimizer creates a robust support in the top part of the blade, on the suction side, resisting the global bending and torsion, while on the pressure side, several supports are distributed along the surface and depending on the stress constraint, their thickness varies. In case (b) and (d), the allowable maximum stress was set to $32.5\,MPa$ and the stress constraint was active for the first 2 iterations. The stress fields reveal that higher values are identified around the blade, indicating that the region where the density was initialized to approximately zero has lower stiffness and therefore it is less capable of transferring the loads. During the first iterations, the densities in critical regions are increasing and therefore, the stress constraint is rapidly satisfied. In case (c) where the maximum allowable was reduced to $0.3\,MPa$, the stress constraint is active for the full optimization. This suggests that the final geometry was highly influenced by it, creating thicker and robust supports around the blade. Similarities in topologies are observed between case (a) and (c), indicating that the baseline result was already able to satisfy stricter stress requirements. In both cases, the load paths are well defined and additional refinements are performed in case (c) in order to satisfy the stress constraint.

The deformation pattern for the distributed load presented an uniform and gradual increase from the clamped region towards the top, while in the multiple-load case, the displacement magnitude presented higher values in the upper trailing edge region of the blade. However, thin supports were created on the pressure side when the maximum allowable stress was set to $32.5\,MPa$, allowing a higher stress level in the structure without the need to perform local reinforcement.

The blade experiences low stresses when the forces are applied, suggesting that the aerodynamic loading is not sufficiently high to produce significant deformations. In this topology optimization formulation, the supports are created in order to maximize the chosen eigenfrequencies while being able to carry the prescribed loads. As a result, several connections between the blade surface and the clamped regions are created, increasing the global stiffness of the structure. In all cases, the volume and stress constraints were satisfied. The final mode shape analysis revealed that the local deformations are present in the free regions, while the global bending and torsion patterns are suppressed.

Overall, the analyzed results indicate that the cantilever blade is capable to withstand the aerodynamic load, presenting low stress values near the root. Therefore, the baseline formulation where the first three eigenfrequencies are maximized with respect to the 10 % volume constraint offers an efficient result from a mechanical point of view, suppressing local deformations and creating a more stiffer structure.

Chapter 6

Application on an industrial case

In this chapter, the industrial application is presented, along with its mechanical status. Afterwards, two $3D$ topology optimizations are presented and their corresponding results are analyzed.

6.1 General description of the industrial case

The industrial application represents a turning vanes system that is able to reproduce complex flow patterns of high level total pressure distortion and large flow angles. In the preliminary design stage, the system is designed using a method inspired from the StreamVane method, described by Virginia Tech [21]. As an input, the velocity field at the Aerodynamic Interference Plane (AIP) is required, along with several seeding points that are used to compute the streamlines and the in-plane velocity field. Therefore, with the obtained streamlines, the position of the support vanes is defined. By distributing secondary seeding points on the defined support vane lines, another set of streamlines in orthogonal in-plane velocity field is created in order to determine the guide vanes positions. The stacking points are used afterwards to probe the desired turning angle at several uniformly distributed points and for each stacking point, an airfoil section of the guide vane is defined [21].

In order to evaluate the assembly, a fluid-structure simulation was performed, where the imposed Mach number was set to $M_{AIP} = 0.565$. Because the result presented higher von Mises stresses than the allowable limit, several supports were added in order to increase the mechanical resistance. The imposed velocity field, along with the obtained geometry is presented in fig. 6.1 .

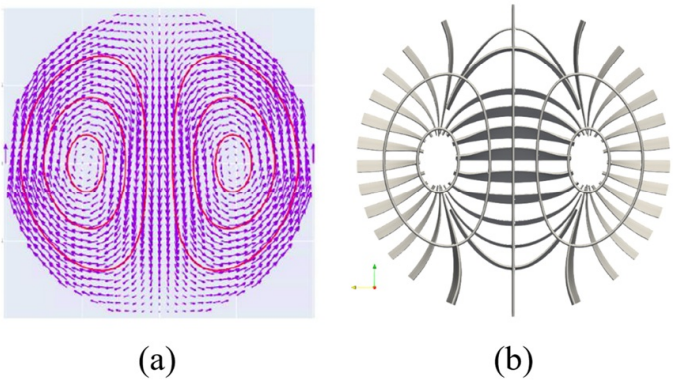


Figure 6.1: Velocity field used for preliminary design (a) and turning vanes system (b). Adapted from Grondin [21]

A RANS-based CFD computation was performed in order to obtain the swirl angle field downstream the turning vanes system and the obtained result were compared with the target angle field, as it is presented in fig. 6.2. The result presents a good agreement between the two fields, with a discrepancy of approximately 2° of the swirl pattern [21].

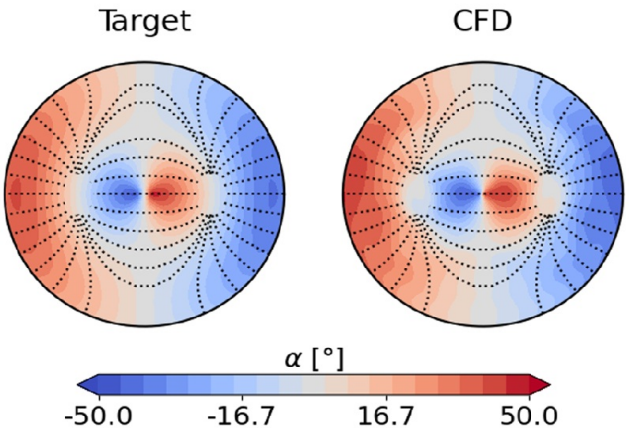


Figure 6.2: Comparison between the target swirl angle α and the obtained result using CFD simulation. Adapted from Grondin [21].

6.2 Industrial case analysis

The CAD model of the swirl device used in the following optimizations was provided by Cenaero.

The geometry of the assembly is presented in fig. 6.3. The geometry is composed of 5 supports and 37 blades and it is symmetric with respect to the $z-$ plane. The blades feature a slender geometry with a slight twist along the span and a varying chord length, providing the aerodynamic function, while the supports are added for additional strength and stability.

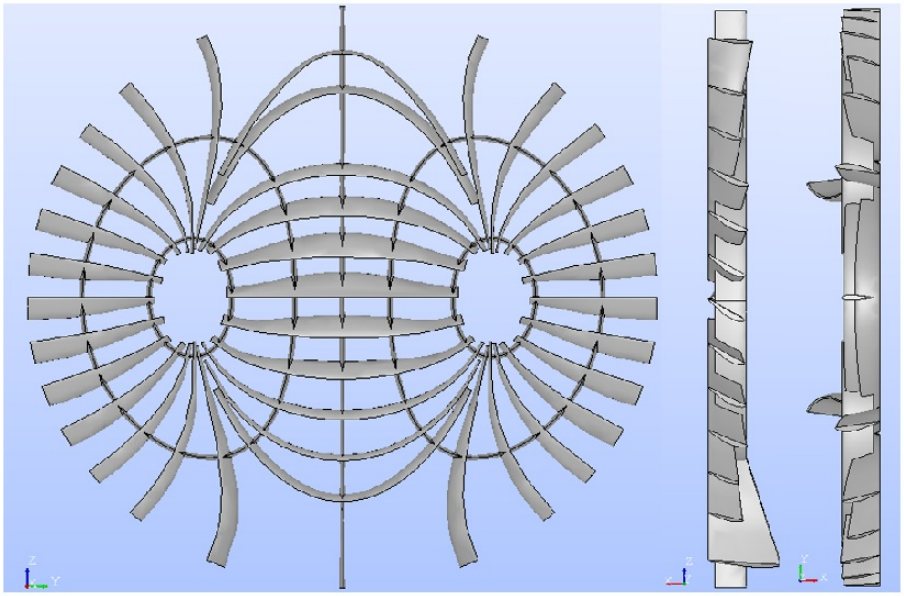


Figure 6.3: Swirl device geometry: a) front view, b) lateral view, c) top view

The optimization strategy presented in chapters 4 and 5 is applied on the industrial case and therefore, a modal analysis is needed in order to extract the first mode shapes and analyze the deformation patterns. Other choices regarding the formulation, parameters used in the CFD computation, material or boundary conditions were based on the observation drawn from the industrial case.

The geometry mesh was generated in Salome Meca software, using the NETGEN 1D-2D-3D algorithm. The domain discretization was created using an unstructured first-order tetrahedral mesh, containing $23,090$ nodes and $59,427$ volume elements. For the boundary conditions, the outer faces of the blades and longitudinal supports are clamped, as it is presented in fig. 6.4.

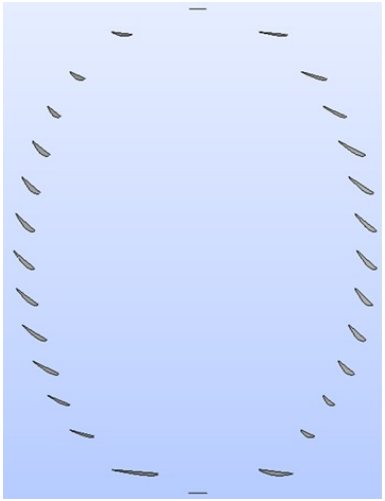


Figure 6.4: Swirl device geometry: clamped surfaces

The modal analysis is performed using Morfeo and the first six natural frequencies are presented in tab. 6.1, while the corresponding mode shapes are visualized using the Salome Meca integrated module, ParaViS and they are presented in figs. 6.5 and 6.6. The first mode shape occurs for $f_1 = 19.42\,Hz$ and it corresponds to the first global bending mode, where the middle region of the system exhibits the largest deformation. The second and third modes occur for $f_2 = 35.25\,Hz$ and $f_3 = 38.47\,Hz$, respectively and they are characterized by a localized deformation of a blade located in the lower section of the system, while the rest of the geometry remains nearly undeformed. Their natural frequencies exhibit close values, indicating a similar dynamic behavior associated with the observed deformation patterns. Subsequently, the global fourth and fifth modes occur at $f_4 = 55.35\,Hz$ and $f_5 = 57.07\,Hz$, respectively. Mode 4 exhibits a bending motion on the $y-$ axis, whereas mode 5 presents a bending motion on the $z-$ direction. Finally, the localized sixth mode occurs for $f_6 = 67.16\,Hz$ and two blades from the lower region of the system exhibit a large deformation pattern.

An identical topology optimization procedure is going to be applied on the industrial case. In the simplified case, the eigenfrequency maximization with respect to a $10\,\%$ volume constraint was applied and compared to the case where an additional stress constraint was introduced. The applied aerodynamic loading was obtained using a CFD simulation and it was shown that the optimization was mainly driven by the eigenfrequencies maximization objective since the stress field presented relatively low values and therefore, a relatively low influence. In the final geometry, the blade was connected by several supports to the clamping regions and a stiffer geometry that automatically satisfies the stress constraint was obtained. Similarly, the

Table 6.1: First six natural frequencies - industry application

Mode	Frequency [Hz]
f_1	19.42
f_2	35.25
f_3	38.47
f_4	55.35
f_5	57.07
f_6	67.16

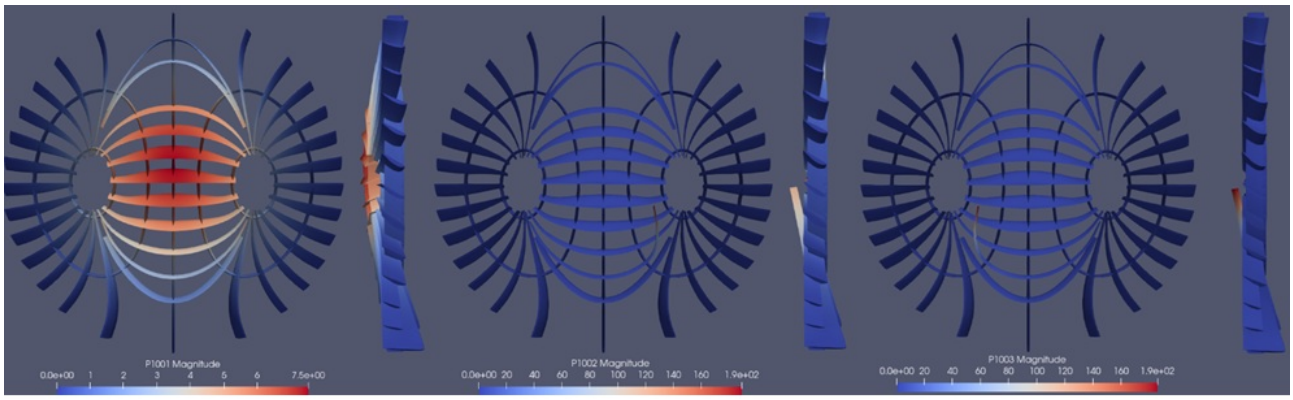


Figure 6.5: Mode shapes 1, 2, 3 for the industry application

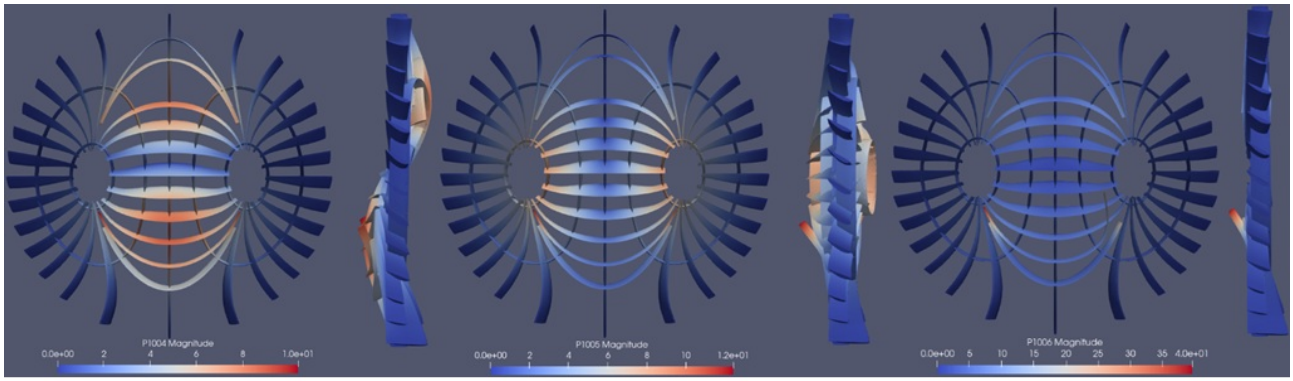


Figure 6.6: Mode shapes 4, 5, 6 for the industry application

industrial case is subjected to the same type of loading and since the simplified configuration demonstrated that a stiffer structure with low stresses was obtained, the optimization where the first three eigenfrequencies are maximized, along with a volume constraint is imposed. This current application is able to evaluate whether the presented methodology can be applied to a realistic and more complex geometry.

Therefore, four optimization cases are presented. The topology optimization formulation remains identical with respect to the baseline described in $2D$ and $3D$ cases, where the eigenfrequencies were maximized and a 10 % volume constraint was imposed. This optimization framework ensures that the new connections between the blades and supports are created in order to increase the stiffness and therefore, to reduce the modal deformations. The 10 % volume fraction facilitates the creation of thin reinforcements without compromising the aerodynamic performances of the distortion grid. In the first three case, the domain definition is based on the simplified case, where the blade geometry was fully embedded inside an optimiz-

able domain, allowing the optimizer to form connections while providing complete freedom. For the first optimization, the first three eigenfrequencies are considered, while in the next two cases, the focus is placed on the first eigenfrequency and on the second and third eigenfrequencies, respectively. In the fourth case, four restricted domains are added in order to show that the optimizer can be guided to form supports in specific regions. By defining zones in which the influence on the aerodynamic flow is reduced, a better preservation on the aerodynamic performances is maintained, while imposing only mechanical constraints.

6.3 Baseline design domain

In the current section, the baseline optimization formulation is applied on the industrial case and the obtained results are presented and analyzed.

6.3.1 Problem formulation

The geometry used in the current optimization case is presented in fig. 6.7, along with the corresponding domains. A cylinder is created around the distortion grid system and an unstructured tetrahedral mesh is generated using Salome Meca software with NETGEN 1D-2D-3D algorithm, resulting in a discretization with 829,793 elements and 139,017 nodes.

The full domain is written as Ω and contains two sub-domains such that $\Omega = \Omega_d \cup \Omega_{nd}$. The optimizable region is denoted as Ω_d (displayed in gray), representing the region where the optimizer is expected to create connections and supports, while the non-optimizable domain is written as Ω_{nd} (displayed in red), corresponding to the region that remains unchanged during the optimization. The boundary conditions are given by Γ_{fix} (displayed in green), defining the 28 surfaces that are fully clamped, as it was shown in fig. 6.3 such as:

$$\mathbf{u} = \mathbf{0} \quad \text{on} \quad \Gamma_{fix}. \tag{6.1}$$

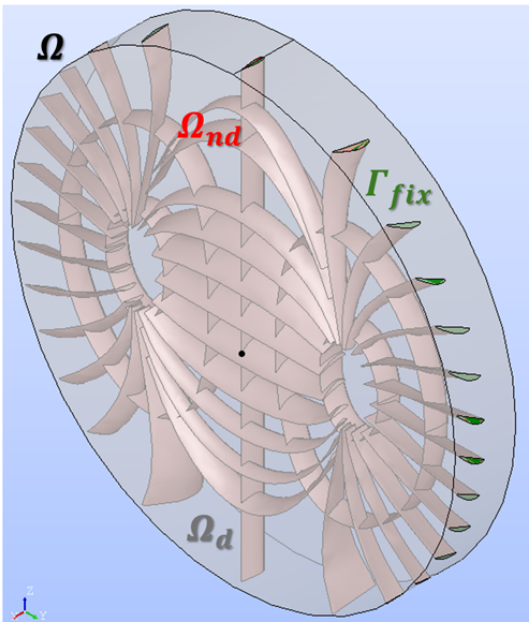


Figure 6.7: Geometry used in the topology optimization process - baseline case

The baseline formulation is kept unchanged and the optimization problem can be described by the equation (4.11) and an identical optimization setup is transferred to the current case. Therefore, the first three eigenfrequencies maximization was set as an objective, while a 10 % volume constraint was imposed. A density filter is used and the radius is chosen to be equal to $7\,mm$, since the local element size is approximately $2\,mm$. For the scaling parameters, the chosen values are presented in tab. 6.2. Since the objective and constraint functions differed by a few orders of magnitude because of different mathematical formulations, the parameters were adjusted such that comparable magnitudes were obtained, improving the numerical conditioning of the problem.

Table 6.2: Scaling parameters - 4

Objective: Eigenfrequencies	**Constraint:** Volume
$1e4$	1

6.3.2 Results and discussion

The final geometry is visualized in ParaViS and the obtained results are presented in fig. 6.8. The initial mode shapes of the structure are presented in fig. 6.5 where the first mode represents a global bending, while the other two modes are characterized by a local deformation concentrated on the free parts of a blade.

In the final design, several connections are created between the blades that exhibit large modal deformations and the system's supports. In the upper and lower part of the distortion grid system, the blades are connected through the longitudinal support in order to increase the local stiffness. The optimizer forms additional connections between the blades, improving the structural connectivity and load transfer. More robust members are formed around the two inner circular supports that are highly contributing in the first bending mode, forming a direct link between slender blades located in the upper and lower area. For the second and third mode, the blade that exhibits a larger deformation is connected to the inner circular supports through the formed paths and therefore, the local stiffness is highly improved. Additionally, the intersection between the initial distortion grids supports and the blades was reinforced by placing additional elements with intermediate densities and creating smoother connections.

The final result reveals that the optimizer preserves the same design principles as in the simplified test case optimization. Several connections are added in order to increase the stiffness in areas with high flexibility, while the main load paths are reinforced. Therefore, for the industrial case, additional connections appear between the slender blades rather than between the structure and the clamping regions. This can be justified by the fact that the distance between the blades was small and a significant increase in stiffness can be obtained by adding a reduced amount of material in the available area.

The objective and constraint evolution with respect to iterations is presented in figs. 6.9 and 6.10. The objective function presents a smooth evolution through the optimization process. After 100 iteration, a restart was performed and a change in the slope is observed. This can be justified by the fact that the design state is recovered, but not necessarily the complete numerical history such as search directions and moving asymptotes. However, a high improvement is noticed in the first half of the process, suggesting that the optimizer rapidly identifies

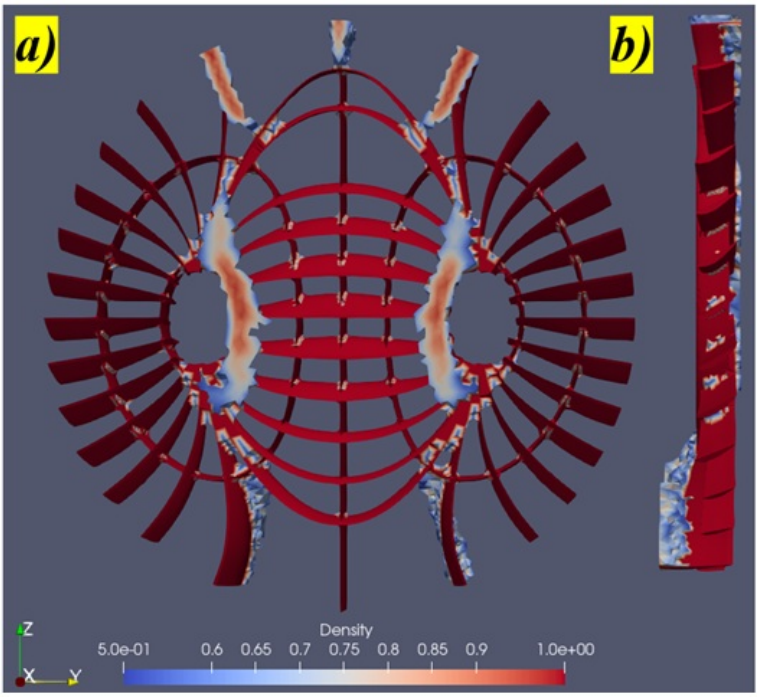


Figure 6.8: $3D$ density based optimization result (objective: maximize the first three eigenfrequencies, constraint: retain 10 % of the initial volume) - a) front view, b) lateral view with [0.5, 1] retained densities, baseline case

optimal material distribution paths and afterwards, local refinements are performed in order to maximize the eigenfrequencies while satisfying the constraint. A similar behavior is identified for the volume constraint evolution, where a smooth convergence is obtained. Small local oscillations are identified, indicating that isolated adjustments were executed. Therefore, both trends reveal that the dynamic performance was improved by a controlled material distribution through the optimization process.

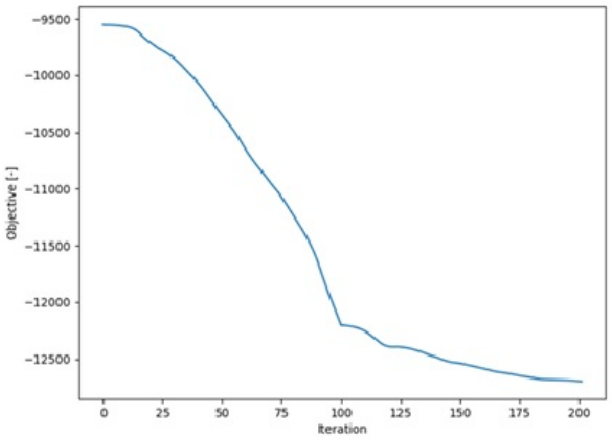


Figure 6.9: $3D$ density based optimization - maximizing eigenfrequencies objective evolution with respect to the iterations - baseline case

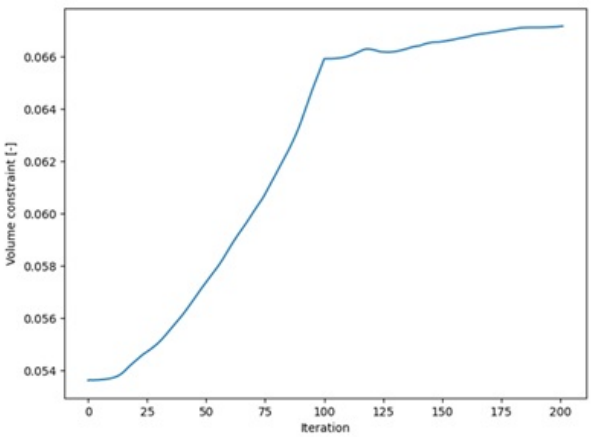


Figure 6.10: $3D$ density based optimization - volume constraint evolution with respect to the iterations - baseline case

The natural frequencies evolution with respect to the iterations is presented in fig. 6.11, along with the obtained values presented in tab. 6.3. The graph displays a smooth increases

for all the targeted modes, illustrating that the maximization was achieved through a balanced material distribution. The first natural frequency presents a small increase, indicating that the global bending was not drastically suppresses, while for second and third values, a greater improvement is observed.

	$f_1[rad/s]$	$f_2[rad/s]$	$f_3[rad/s]$
Iter. 0	122.1	221.4	241.6
Iter. 100	141.4	262.4	264.9

Table 6.3: Natural frequencies - baseline case

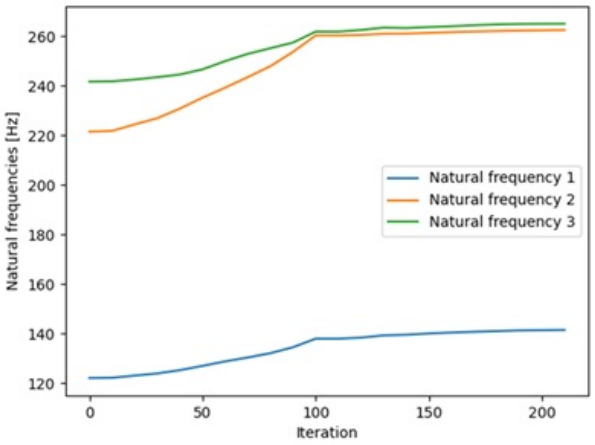


Figure 6.11: $3D$ density based optimization - first three natural frequencies evolution with respect to the iterations - baseline case

The obtained mode shapes of the final geometry are presented in fig. 6.12, while the initial deformation patterns are illustrated in fig. 6.5. The comparison reveals that the first bending mode is not fully suppresses and therefore, small improvements are obtained for the corresponding natural frequency. Since this mode involves the deformation of the entire structure, a significant increase in natural frequency may be obtained by a large increase in structure's global stiffness. With a restrictive volume fraction, the material is placed in localized flexible regions, where small enforcements are determining a high increase in local stiffness. As a result, the deformation of the flexible blade from the second and third mode is suppressed, while the first mode shape deformation pattern is slightly improved. Because all the blades extremities are clamped, global bending remains the dominant deformation pattern and therefore, the mode shape characteristics may be reduced by a drastic increase in global stiffness.

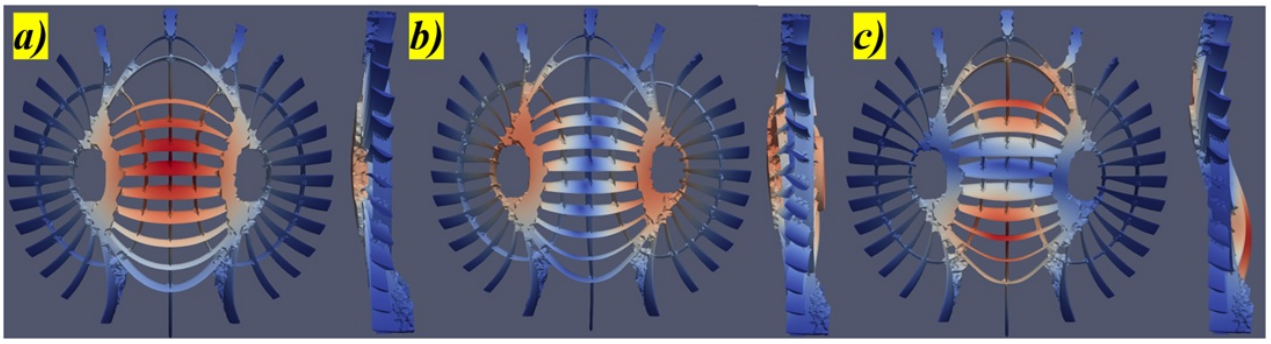


Figure 6.12: First three mode shapes of the obtained geometry with [0.5, 1] retained densities - baseline case

To ensure thin connections inside the distortion grid system, a reduced fraction of the initial volume can be retained such that the flow is not highly influenced. Therefore, the optimizer has less available material that can be placed in critical regions and the improvements in global

modes are more limited. The optimizer is placing the material in local flexible regions, gaining a significant increase in local stiffness, reducing the isolated bending behavior. This indicates a trade-off between the aerodynamic and structural objectives since larger supports may offer an increase in mechanical resistance, but the flow field may be highly disturbed.

6.3.3 Influence of eigenfrequency maximization formulation

Because it was shown that the first mode shape of the distortion grid system represents a global bending mode, while the second and third mode illustrate a localized deformation on a single blade, two optimization scenarios are considered.

For the second optimization investigated here, the objective is treating only the first eigenfrequency and the optimization problem can be written as:

$$\begin{aligned} \max_{\boldsymbol{\rho}} \quad & \left(\frac{1}{\lambda_0(\boldsymbol{\rho})}\right)^{-1} \\ \text{s.t.} \quad & \frac{V(\boldsymbol{\rho})}{V_0} \leq 0.10, \\ & 0 \leq \rho \leq 1 \end{aligned} \tag{6.2}$$

and the corresponding result with densities between [0.8, 1] is presented in fig. 6.13. Since the maximization of the first eigenfrequency is imposed, the whole structure participates in the deformation. In order to reduce the bending, the global stiffness of the structure needs to be increased and therefore, the optimizer distributes material in several regions, creating continuous connections between several blades. The slender blades located in the top and bottom regions are reinforced and connected to the circular supports, while isolated zones around the fixed faces present considerable material addition.

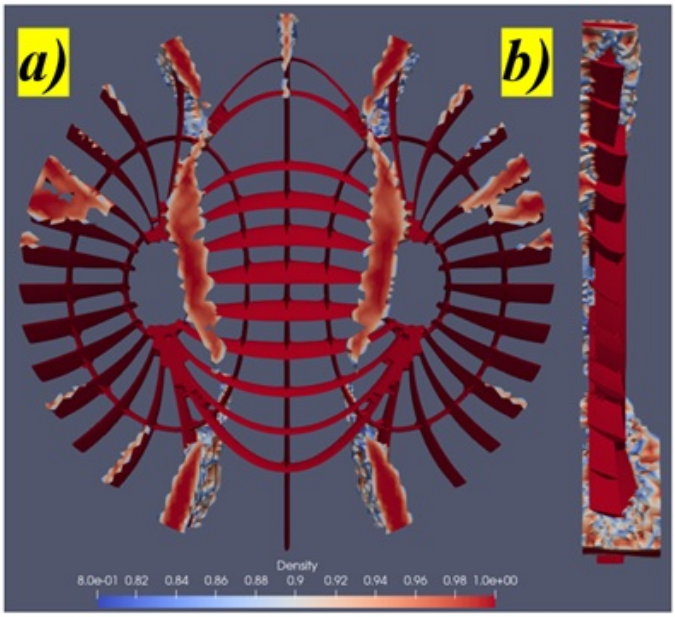


Figure 6.13: Topology optimization result - maximization of the first eigenfrequency, retained densities [0.8, 1]

The first three mode shapes are presented in fig. 6.14 and an identical scaling factor is used. The global bending is reduced and the corresponding natural frequency obtained at iteration 100 is equal to $f_1 = 193.6\,rad/s$, while in the baseline case, f_1 reached $141.4\,rad/s$, indicating a significant increase in global stiffness. For mode 2 and 3, a global bending motion is observed as well, suggesting that the localized blade motion from the initial mode shapes is also suppressed.

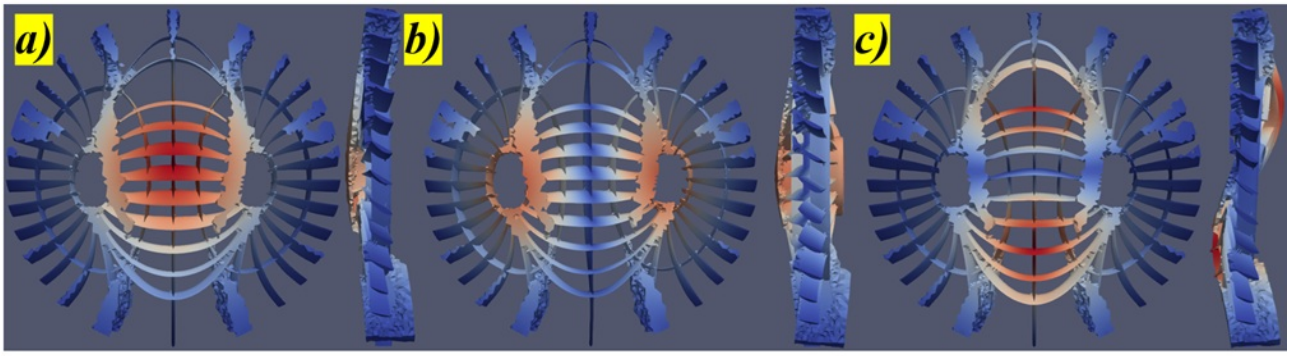


Figure 6.14: First three mode shapes of the obtained geometry with [0.8, 1] retained densities - first eigenfrequency maximization

Regarding the third case, the objective is considering only the second and the third eigenfrequencies and the optimization problem is written as:

$$\begin{aligned} \max_{\boldsymbol{\rho}} \quad & \left(\sum_{i=1}^{n=2} \frac{1}{\lambda_i(\boldsymbol{\rho})} \right)^{-1} \\ \text{s.t.} \quad & \frac{V(\boldsymbol{\rho})}{V_0} \leq 0.10, \\ & 0 \leq \rho \leq 1, \end{aligned} \tag{6.3}$$

and the obtained result with densities between [0.8, 1] is presented in fig. 6.15. The modes 2 and 3 of the distortion grid system shown in fig. 6.5 displayed a localized deformation on a specific blade, while the rest of the structure was nearly undeformed. Because the objective was to reduce this deformation, the critical blade was connected to the inner circular supports by placing material in the free spaces between the blades. Additional connections were created in the top region where the slender blades were not fully connected to the system's supports.

The mode shapes are extracted at iteration 100 and the obtained results are presented in fig. 6.16. An identical scaling factor was used for a better visualization and it can be observed that the localized deformation is suppresses. For mode 2 and 3, the obtained natural frequencies are equal to $f_2 = 226.5\,rad/s$ and $f_3 = 246.5\,rad/s$, indicating similar values to the ones obtained in the baseline formulation. This result is expected since in the baseline case, the blade deformation was fully suppressed. Mode 1 is not highly influenced by the changes and therefore, the global bending is not reduced.

This comparison reveals that the case where the first eigenfrequency is included is more conservative since the local deformations are suppressed as well. When a global bending mode is optimized, several thick connections are generated, increasing the global stiffness. While this is a desirable result in terms of mechanical resistance, from an aerodynamic perspective, the flow may be highly disturbed because of the large material additions. In contrast, the case that considers the second and third eigenfrequencies presents a low added volume. Even though

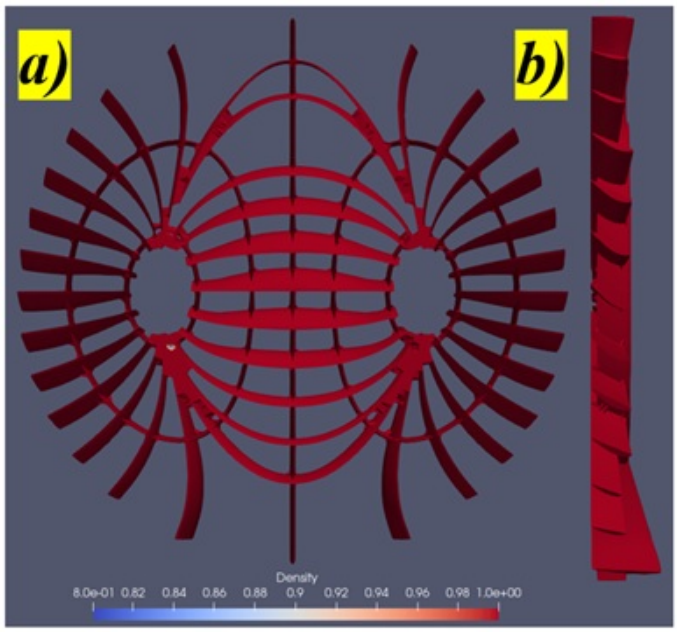


Figure 6.15: Topology optimization result - maximization of the second and third eigenfrequencies, retained densities [0.8, 1]

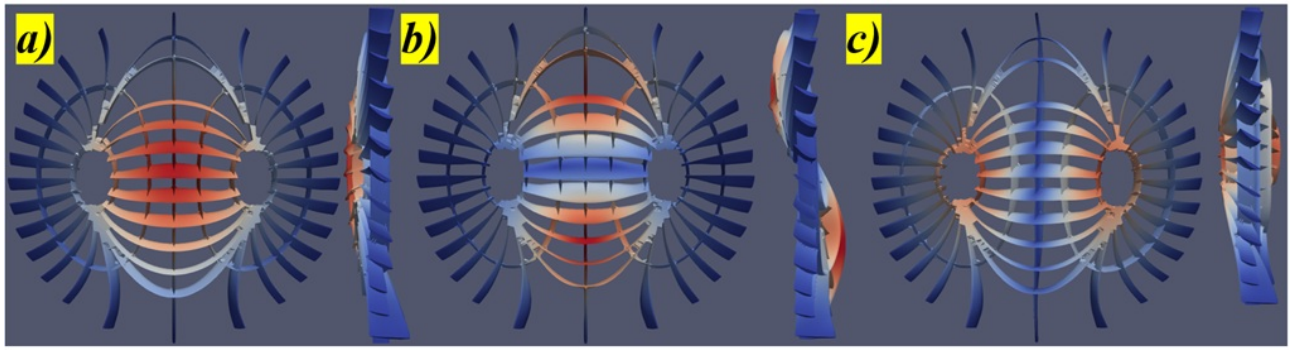


Figure 6.16: First three mode shapes of the obtained geometry with [0.8, 1] retained densities - second and third eigenfrequencies maximization

the global bending is not reduced, the local deformations are suppresses and the added volume occupies a reduced amount of space.

6.4 Guided design domain

The analysis is now focused on a case where a restrictive domain is used. In the previous optimization, the distortion grid system was surrounded by one continuous design domain, while in the current setup, four domains are defined in regions of interest.

6.4.1 Problem formulation

The modified geometry used in the current optimization case is presented in fig. 6.17, along with the corresponding domains. Four reduced domains are added in regions where the modal deformation was large, in order to guide the optimizer to increase the local stiffness only in the selected zones. Two cylinders are added around the inner circular supports and around them, two other hollow cylinders are created in order to ensure that the critical regions are included.

Therefore, the blade that exhibits a larger deformation in the second and third mode shapes illustrated in fig. 6.5 is now enclosed on the optimizable regions, facilitating new connections that may be able to suppress the associated deformation. The unstructured tetrahedral mesh was generated in Salome Meca, using the NETGEN 1D-2D-3D algorithm and the final result presents $1,258,340$ elements and $260,476$ nodes.

The full domain is denoted by Ω and it contains two sub-domains such as $\Omega = \Omega_d \cup \Omega_{nd}$. The optimizable domain (displayed in purple) is represented by the Ω_d region and it includes the four restricted domains, while the non-optimizable domain Ω_d (displayed in blue) includes the blades and supports and represents the region that remains unchanged during the optimization. The exterior faces of the blades are clamped, as it was shown in fig. 6.3, written as Γ_{fix}.

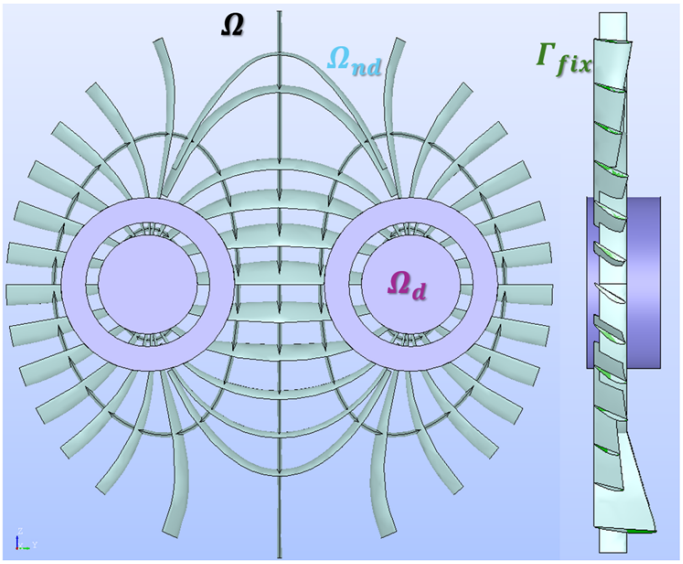


Figure 6.17: Geometry used in topology optimization process - guided design case

The optimization problem can be described by equation (4.11), while the setup remains unchanged. Therefore, the objective was defined by the first three eigenfrequencies maximization, while a $10\,\%$ volume constraint was applied in the optimizable domain. A new filter radius equal to $7\,mm$ is chosen and the new scaling parameters are presented in tab. 6.4.

Table 6.4: Scaling parameters - 5

Objective: Eigenfrequencies	**Constraint:** Volume
$1e8$	1

6.4.2 Results and discussion

The obtained geometry after 100 iterations is visualized in ParaViS, extracting the densities between [0.5, 1] and the final result is presented in fig. 6.18. For the reference, the initial mode shapes are given in fig. 6.5.

It can be clearly observed that the inner circles are removed almost entirely and additional material was placed on the circular supports, towards the center of the system. Within the

optimizable region, the maximum modal deformation corresponding to mode 1 is concentrated in the circular supports, closer to the longitudinal structural member. Therefore, the material addition contributes to the first eigenfrequency maximization, adding volume in the critical regions in order to increase the stiffness. For the second and third modes, the deforming part is connected to the surrounding blades by adding material in the narrow spaces between the blades, improving the local stiffness and offering additional support to the critical component. A larger support is created from the given hollow cylinder, connecting the blades in the lateral regions of the distortion grid system and adding a large contribution in global stiffness. Instead of placing material in the center region that is experiencing large bending deformations, the optimizer adds reinforcement in the farthest points of the optimizable domain, creating a more efficient geometry from a mechanical perspective.

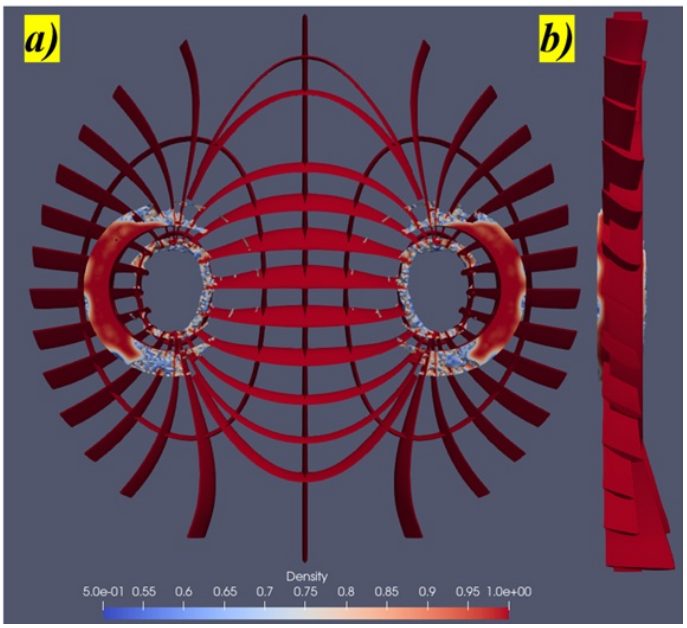


Figure 6.18: $3D$ density based optimization result (objective: maximize the first three eigenfrequencies, constraint: retain 10 % of the initial volume) - a) front view, b) lateral view with [0.5, 1] retained densities - guided design domain case

The objective and constraint evolution with respect to the iteration is presented in figs. 6.19 and 6.20. For the objective, several oscillations are observed in the first 20 iterations, suggesting that the optimizer was continuously searching for efficient paths that can increase the mode shapes while taking into account the volume constraints. After the main load paths were defined, the oscillations were reduced and a smooth decrease is observed in the second half of the process.

The volume constraint displays a similar behavior to the one presented by the objective function. Therefore, at the beginning of the process, large density field adjustments are made in order to identify the main load paths. Since the eigenfrequencies maximization is strongly coupled with the material redistribution, small refinements in volume can highly affect the eigenfrequencies, resulting in oscillations in both evolutions. Afterwards, the function is experiencing a smooth increase and small corrections are performed in order to satisfy the constraint.

The natural frequencies evolution, along with the corresponding values is presented in fig. 6.21. After the main paths were defined by the optimizer in the first 20 iterations, a smooth

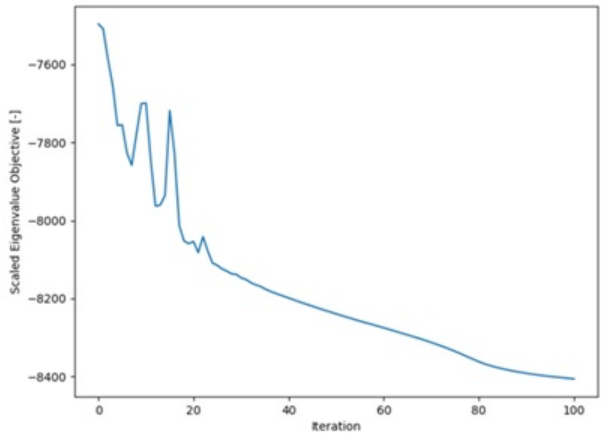


Figure 6.19: $3D$ density based optimization - maximizing eigenfrequencies objective evolution with respect to the iterations - guided design case

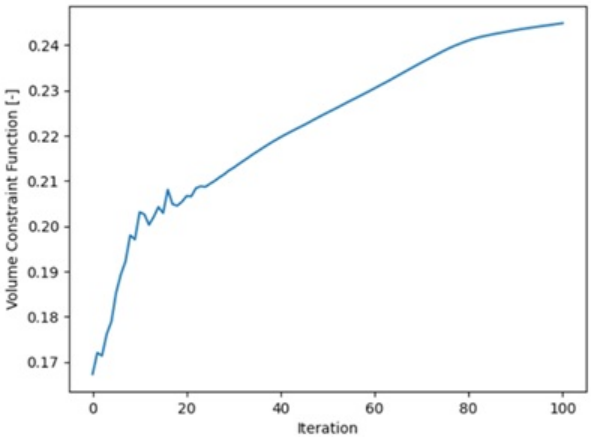


Figure 6.20: $3D$ density based optimization - volume constraint evolution with respect to the iterations - guided design case

growth is observed. The increase is slight, indicating that the deformation pattern illustrated by the mode shapes were not fully suppresses. The first two mode shapes present an increase of $10\,rad/s$, while the third one display a growth of $20\,rad/s$. This behavior is similar to the one observed in the baseline case, where the global bending exhibited in mode 1 was slightly reduced. In the current case where the optimizable domain was restrictive, this result is expected since the added volumes target especially mode 2 and 3, aiming to create additional connections that can offer support to the deforming blade.

	$f_1[rad/s]$	$f_2[rad/s]$	$f_3[rad/s]$
Iter. 0	109.1	190.7	213.4
Iter. 100	114.6	201.5	233.6

Table 6.5: Natural frequencies - guided design case

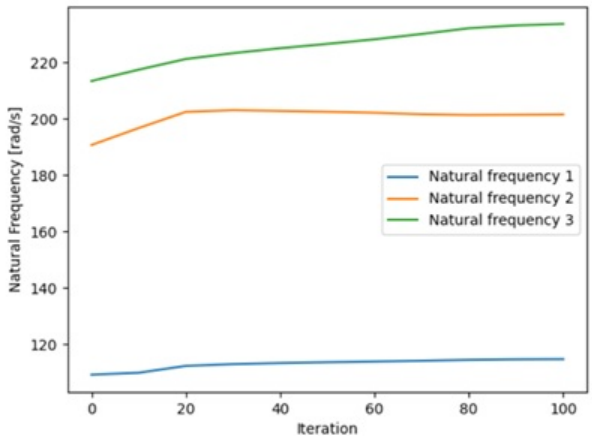


Figure 6.21: $3D$ density based optimization - first three natural frequencies evolution with respect to the iterations - guided design case

The mode shapes at iteration 100 are presented in fig. 6.22. Similar deformation patterns to the baseline case shown in fig. 6.12 are observed, suggesting that the fundamental structural behavior did not change. The overall geometry and the boundary conditions are not modified and therefore, the dynamic characteristics are preserved even though different connections and supports are added. All three mode shapes display a bending motion and since all the blade extremities are clamped, the result is expected.

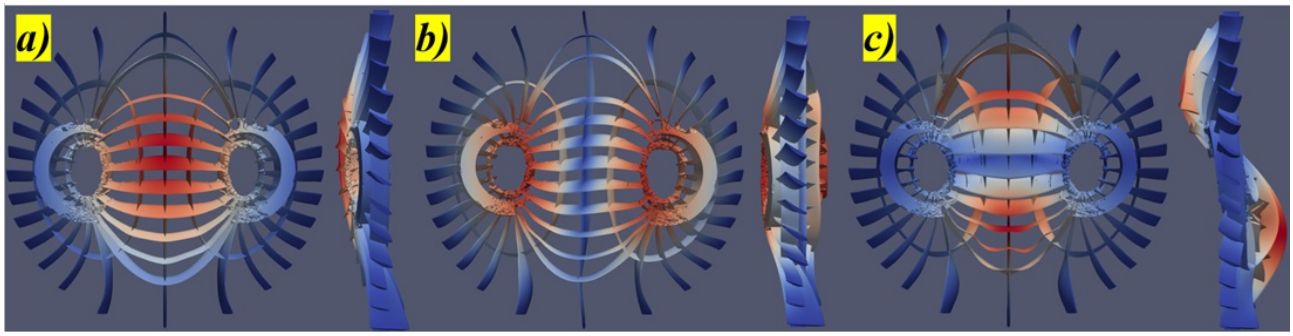


Figure 6.22: First three mode shapes of the obtained geometry with [0.5, 1] retained densities - guided design case

Overall, the restricted volume domains were added by taking into account the deforming blade observed in the initial mode shapes 2 and 3 and therefore, the mechanical performance was targeted. Additionally, more complex volumes could be defined by following the imposed velocity field presented in fig. 6.1. With this approach, the optimizable domains are limited to regions where supports can be added without highly affecting the flow field and a better preservation of the aerodynamic capabilities can be achieved.

6.5 Summary

The optimization procedure developed on the simplified test case has been applied on the industrial application. The aim of the optimization was to create a stiffer final structure and by increasing the first natural frequencies, the flutter stability can be improved as well. In all the cases, the eigenfrequencies maximization was considered and a 10 % volume constraint was imposed in order to obtain relatively thin and slender connections.

By adding a large design domain around the distortion grid system, several connections can be created and the global modes displacements of the structure can be reduced. With a more restricted design domain, localized modes can be targeted and a smaller material addition is needed. Both cases present similar final mode shapes, where the displacements are mainly dominated by bending. For a preliminary design phase, the restricted approach presents a significant benefit since the volumes can be added with respect to the velocity field and therefore, the aerodynamic performance can be preserved.

Overall, a trade-off between mechanical resistance and aerodynamic considerations is observed, since an increased amount of material distribution may lead to larger flow obstructions. In the case where only the localized modes are optimized, a small amount of material is occupied and the local deformations are reduced. In contrast, when a global mode is optimized, material is distributed in several regions and the aerodynamic capabilities may be reduced. This suggests that the proposed methodology does not eliminate the need for CFD simulation, but it can serve as a preliminary structural assessment that can evaluate rapidly the dynamic response, multiple design alternatives and compromises.

Chapter 7

Conclusions and perspectives

This thesis presented a topology optimization methodology developed on a simplified test case in order to increase the mechanical performances of the structure. The framework was then applied to an industrial application and the corresponding results were analyzed.

For the simplified test case, a slender blade was chosen based on an extruded NACA 9410 airfoil in order to replicate the main characteristics of a distortion grid system. A modal analysis was performed using Morfeo in order to understand the dynamic behavior of the structure, along with a CFD simulation that was used to extract the loadings. In the initial stage, several two-dimensional cases were tested starting from an eigenfrequencies optimization objective and a volume constraint. An additional stress constraint was introduced and the maximum allowable limit was lowered in order to demonstrate that the stresses can be reduced with the proposed framework and lastly, a more complex loading scenario was imposed. In all the cases, a similar rib system that connected to the blade to the clamping regions was observed, indicating that the stress constraint was mainly used for local material distribution refinements. Therefore, the formulation where the objective is set to maximize the first three eigenfrequencies while taking into account the volume constraint provide a stiffer structure that can exhibit lower deformations, leading to an overall improvement in the mechanical response.

The two-dimensional cases served as a methodology development platform since they have a low computational cost and facilitate parameters calibration. Once the methodology was validated, identical approaches were applied for the three-dimensional cases in order to analyze the capabilities on a more realistic configuration, resulting in four distinct topology optimization cases. The $3D$ results presented final geometries that were able to suppress the initial mode shapes deformation patterns, while the volume constraint was successfully satisfied. Several thin supports were created in critical regions, especially in the mid-span and top regions, where maximum deformations were observed. The main locations of the supports were preserved in all optimization, while in the case where the maximum allowable stress limit was reduced, the stress constraint presented a higher influence in the supports definition, resulting in a thicker multiple supports distributed around the blade. The result was similar to the other three configurations, indicating that the optimization where the first three eigenfrequencies were maximized with respect to the volume constraint offered a structure with a higher stiffness that was capable to withstand the imposed aerodynamic load. With these informations, the optimization setup for the industry application was reduced to an eigenfrequency maximization and a volume constraint formulation.

In order to increase the stiffness of a distortion grid system, thin and slender supports are needed such that the obtained flow field is not highly disturbed. A case where the whole

structure was embedded into a large cylindrical domain was first treated and several connection appear in order to suppress the first global bending mode along with the localized deformation of a blade observed in second and third vibrational mode. Two other cases were analyzed in order to show the influence of the included eigenfrequencies. In a first case, the first eigenfrequency was included and therefore, more thicker connections were needed in order to increase the global stiffness of the structure. This result is not desirable since the drastic material addition may block the flow and may create larger errors between the targeted and obtained flow field. Another case was treated, where only the second and third modes was considered. The localized blade deformation was suppressed with a reduced amount of material, creating connections only between the localized free parts of the blades.

Lastly, a final configuration was tested for the industrial application where restrictive volumes were strategically placed such that the vibrating blade could be attached, resulting in an efficient design that was able to suppress the targeted motion. This method also represents an alternative where the restricted domains can be defined based on the intended flow field, serving as a preliminary design approach that considers only mechanical constraints.

Overall, the industrial case demonstrated that the topology optimization methodology can be transferred from a simplified configuration to a more complex geometry. The baseline along with the restricted domains optimizations produced a material redistribution in the regions that are contributing effectively to structural stiffness, while satisfying the imposed volume constraint. The results emphasize the importance of selecting the targeted modes according to the desired structural behavior since the global modes would require a large material addition, while targeting the localized modes can offer thin connections that suppress the local modal deformation. Additionally, by defining reduced domains, the optimizer is guided toward specific regions, creating connections between existing structural members and providing a platform to introduce aerodynamic considerations indirectly, defining the domains in regions where the new connection may not highly disturb the flow.

Several limitations of this proposed workflow are identified. Only steady-aerodynamic loading conditions were considered in the simplified test case analysis and a two-way fluid-structure interaction (FSI) coupling is needed in order to obtain a final distortion grid system that is capable to withstand the loadings. Another limitation is represented by the aeroelastic phenomena and more precisely, the flutter analysis should be done in detail in order to address the stability and to identify the critical points. Additionally, manufacturing constraints may be imposed to provide efficient material distributions.

Bibliography

[1] E. Boufidi et al., "Coupled Design of Multi-Component Distortion-Generating Devices for Aircraft Engine Ground Tests – Part II: Experimental Characterization in a Closed-Loop, High Speed Test Rig," en, in *Volume 1: Aircraft Engine*, London, United Kingdom: American Society of Mechanical Engineers, Jun. 2024, V001T01A056, ISBN: 978-0-7918-8792-9. DOI: 10.1115/GT2024-128870

[2] B. König et al., "DLR TAU-Code uRANS Turbofan Modeling for Aircraft Aerodynamics Investigations," *Aerospace*, vol. 6, no. 11, p. 121, 2019. DOI: 10.3390/aerospace6110121

[3] D. Delling. "5 things to know about the cfm rise program," GE Aerospace. [Online]. Available: https://www.geaerospace.com/news/articles/5-things-know-about-cfm-rise-program

[4] J. Kurzke and I. Halliwell, *Propulsion and Power*, en. Cham: Springer International Publishing, 2018, ISBN: 978-3-319-75977-7 978-3-319-75979-1. DOI: 10.1007/978-3-319-75979-1

[5] K. M. Hoopes, "A New Method for Generating Swirl Inlet Distortion for Jet Engine Research," en,

[6] H. Li, C. Wang, X. Zhang, J. Li, J. Shen, and S. Zhou, "A Mini Review on Fluid Topology Optimization," en, *Materials*, vol. 16, no. 18, p. 6073, Sep. 2023, ISSN: 1996-1944. DOI: 10.3390/ma16186073

[7] T. Guimarães, K. T. Lowe, and W. O'Brien, "An overview of recent results using the StreamVaneTM method for generating tailored swirl distortion in jet engine research," en,

[8] I. Ordaz, S. K. Rallabhandi, E. J. Nielsen, and B. Diskin, "Mitigation of engine inlet distortion through adjoint-based design," in *54th AIAA Aerospace Sciences Meeting*, San Diego, California: American Institute of Aeronautics and Astronautics (AIAA), 2016. DOI: 10.2514/6.2016-1563

[9] J. Pecinka, G. T. Bugajski, P. Kmoch, and A. Jílek, "Jet engine inlet distortion screen and descriptor evaluation," *Acta Polytechnica*, vol. 57, no. 1, pp. 22–31, 2017. DOI: 10.14311/AP.2017.57.0022

[10] T. G. Bucalo, "Fluid Dynamics of Inlet Swirl Distortions for Turbofan Engine Research," en,

[11] J. Meng, L. Liao, D. Li, Y. Cao, L. Yang, and Y. Chen, "Topology Optimization Method Research on Hollow Wide-chord Fan Blade of a High-bypass Turbofan Engine," en, *Procedia Engineering*, vol. 99, pp. 1228–1233, 2015, ISSN: 18777058. DOI: 10.1016/j.proeng.2014.12.652

[12] C. Lundgaard, J. Alexandersen, M. Zhou, C. S. Andreasen, and O. Sigmund, "Revisiting density-based topology optimization for fluid-structure-interaction problems," en, *Structural and Multidisciplinary Optimization*, vol. 58, no. 3, pp. 969–995, Sep. 2018, ISSN: 1615-147X, 1615-1488. DOI: 10.1007/s00158-018-1940-4

[13] M. Abdelhamid and A. Czekanski, "Topology optimization of fluid-structure interaction problems with total stress equilibrium," en, *International Journal for Numerical Methods in Engineering*, vol. 125, no. 2, e7368, Jan. 2024, ISSN: 0029-5981, 1097-0207. DOI: 10.1002/nme.7368

[14] E. Jonsson, C. Riso, C. A. Lupp, C. E. Cesnik, J. R. Martins, and B. I. Epureanu, "Flutter and post-flutter constraints in aircraft design optimization," en, *Progress in Aerospace Sciences*, vol. 109, p. 100 537, Aug. 2019, ISSN: 03760421. DOI: 10.1016/j.paerosci.2019.04.001

[15] K. E. Jacobson and B. K. Stanford, "Flutter-Constrained Optimization with the Linearized Frequency-Domain Approach," en,

[16] A. Crovato, "PyPk - Collection of p-k methods," en,

[17] M. Schuff, "Coupled Mode Flutter of Turbomachinery Blades," de, Ph.D. dissertation, Deutsches Zentrum für Luft- und Raumfahrt (DLR), 2023. DOI: 10.57676/K1D4-MK17

[18] Airfoil Tools. "Naca 4 digit airfoil generator (naca 9410 airfoil). "[Online]. Available: http://airfoiltools.com/airfoil/naca4digit?MNaca4DigitForm%5Bcamber%5D=9&MNaca4DigitForm%5Bposition%5D=40&MNaca%204DigitForm%5Bthick%5D=10&MNaca4DigitForm%5BnumPoints%5D=81&MNaca4DigitForm%5BcosSpace%5D=0&MNaca4DigitForm%5BcosSpace%5D=1&MNaca4DigitForm%5BcloseTe%5D=0&yt0=Plot

[19] M. Géradin and D. J. Rixen, *Mechanical Vibrations: Theory and Application to Structural Dynamics*, 3rd ed. John Wiley & Sons, 2015, ISBN: 978-1-118-90020-8.

[20] A. Verbart, "Topology optimization with stress constraints," Ph.D. dissertation, Delft University of Technology, Delft, The Netherlands, 2015, ISBN: 978-94-6259-739-6.

[21] J. Grondin et al., "Coupled Design of Multi-Component Distortion-Generating Devices for Aircraft Engine Ground Tests – Part I: Design Methodology and Numerical Validation," en, in *Volume 1: Aircraft Engine*, London, United Kingdom: American Society of Mechanical Engineers, Jun. 2024, V001T01A055, ISBN: 978-0-7918-8792-9. DOI: 10.1115/GT2024-128869